ABSTRACT

| | |
|---|---|
| Title of Document: | IN SITU MANIPULATION OF MAGNETIZATION VIA DIRECT MECHANICAL INTERACTION IN MAGNETOSTRICTIVE THIN FILMS |
| | Paris Noelle Alexander Nero, Doctor of Philosophy, 2014 |
| Directed By: | Associate Professor and Keystone Professor, John P. Cumings, Materials Science and Engineering |

The pursuit of a universal memory– possessing fast write/read times, nonvolatile and unlimited data endurance, low operating power, low manufacture costs, high bit density, as well as being easily integrable with on-trend complementary metal-oxide semiconductor (CMOS) devices– has reenergized research in the field of multiferroic and magnetoelectric materials. Such materials simultaneously exhibit ferroelectricity and ferromagnetism, and allow for the coupling of the two order parameters, known as magnetoelectric coupling. This coupling is enhanced in magnetostrictive/piezoelectric bilayer systems where applied electrical bias can modify magnetic order via strain-mediation, a mechanism that can reduce the power demands in emerging magnetic random access memory (MRAM) technologies. We have previously investigated this relationship in an $Fe_{0.7}Ga_{0.3}/BaTiO_3$ bilayer structure using magnetic contrast imaging techniques with

in situ applied electric fields. The goal of this thesis was to explore methods to better control magnetoelectric effects in order to enhance local magnetic response to external stimuli.

Specifically, we investigated magnetoelastic response of freestanding, magnetostrictive $Fe_{0.7}Ga_{0.3}$ thin films via direct mechanical interaction with an external probe, as the well known strain-mediated mechanism in magnetoelectric devices depends on the lesser known magnetoelastic nature of strain transfer between the distinct material phases. Magnetoelastic effects are directly associated with both external magnetic field and stress via Lorentz-force transmission electron microscopy (LTEM) contrast techniques, and the hysteresis of magnetic order was charted with respect to both stimuli. For relevant application to MRAM devices, we have initiated studying these effects in patterned media as well, where individual, nanoscale magnetic geometries represent bistable bits for memory.

We demonstrate static pure stress effects on the magnetoelastic response in continuous thin films, as well as real-time mechanical "writing" of stable domain states. The external probe is directed into the film, inducing a non-uniform, radially symmetric local strain.

Micromagnetic simulation reveals that the strength of observed magnetoelastic effects is offset by small, undulating variations in magnetization characteristic of polycrystalline thin films, known as magnetization ripple. Imposing a threshold function on the effective anisotropy of the film describes the spontaneous onset of these effects and the differences in magnetic order for films with hysteresis solely due to stress, or with both field and stress. Thus, a method to achieve bistable

logic for MRAM applications using direct uniform stress, in lieu of external fields, is

proposed.

IN SITU MANIPULATION OF MAGNETIZATION VIA DIRECT MECHANICAL
INTERACTION IN MAGNETOSTRICTIVE THIN FILMS


By


Paris Noelle Alexander Nero


Dissertation submitted to the Faculty of the Graduate School of the
University of Maryland, College Park, in partial fulfillment
of the requirements for the degree of
Doctor of Philosophy
2014


Advisory Committee:
Professor John P. Cumings, Chair
Alison Flatau
Lourdes Salamanca-Riba
Ichiro Takeuchi
Manfred Wuttig

# Dedication

This work is dedicated to my family– Renard, Francine, and Milan Alexander– who have loved, supported, and sacrificed for me so that I may realize my dreams. There is a saying that "if you don't believe in yourself, then nobody else will." I am very grateful to have been surrounded by people that have unyieldingly believed in me, even when I could not believe in myself. You all have served as my role models: my father for his humor and hard work ethic, my mother for her creativity and pensiveness, and my sister for her persistence and strength. Thank you for being my foundation and my best cheerleaders!

In my time at the University of Maryland I have forged my closest friendships, and the ultimate example of this is my now husband, Brandon Nero. We first met as undergraduates, and have supported each other through the trials and tribulations of graduate degrees. Brandon, you have been a constant source of encouragement, and a beaming example of hope, optimism, and faith– through you I see the ways that God works in my life. Because of you I have gone places that I would have never gone on my own will; you have taught me that experiencing the world is a worthwhile self-investment. You have helped me through the most trying times of my life, and you have always reminded me that I am a person that seeks self-improvement. Thank you for holding my hand. I look forward to our next adventure!

My friends and fellow colleagues in the Department of Materials Science & Engineering have enriched my life and have maintained my sanity through constant equipment failure, failed experiments, and moments of uncertainty. I will miss our lunches at the picnic table, exploring the new DC, and pursuing physical feats

together. Thanks for making me laugh, and in turn, laughing at my corny jokes, and

teaching me new tricks. You all are brilliant!

# Acknowledgements

# Table of Contents

# List of Tables

# List of Figures

xiv

# Chapter 1: Introduction

## *1.1 Motivation*

The quest for a universal memory solution– having the attributes of fast reading and writing speeds, nonvolatility, unlimited endurance, high data density, low voltage requirements, low cost and facile manufacturing, and integratability with industry prominent CMOS architectures– has reenergized the field of multiferroics. Multiferroic materials display coexistence of at least two ferroic orders (ferroelectricity, anti/ferromagnetism, and ferroelasticity), creating an avenue to realize the coupling of ferroelectric and ferromagnetic order parameters, known as magnetoelectric coupling. This coupling mechanism could allow better control of magnetization through manipulation with electric fields. Herein lies a significant gain towards the search for an universal memory, where the high speed, low cost and facile manufacturing of semiconductor based memories can be intrinsically bridged with the nonvolatility, high endurance, and high bit densities of magnetic memory technologies.

However, intrinsic multiferroic materials are conflicted by an existential paradox where the requirements for ferroelectricity generally contradict those for ferromagnetism. To date, the search continues for a multiferroic material that exhibits strong magnetoelectric coupling at non-cryogenic temperatures. Advances in computation and fabrication of high-quality structures with nanoscale control continue to push research efforts in this direction [1]–[4].

Strong magnetoelectric coupling has been demonstrated in composite multiferroic structures. The constituent phases do not intrinsically exhibit the coupling, but magnetoelectric coupling is achieved via cross-interaction of the individual phases. Here, the order parameters that exist within each phase can be individually tuned and enhanced to generate a strong magnetoelectric response.

While various connectivity schemes are possible in order to realize the effect, bilayer heterostructures are the most common avenue for achieving magnetoelectric coupling. Such structures are easily fabricated using modern physical vapor deposition techniques, and epitaxial growth can be maintained for intimate contact at the interface. Magnetoelectric coupling occurs through either charge-mediated, exchange-bias mediated, or strain-mediated mechanism, or sometimes a cross-linking of two of these mechanisms.

The inherent complexity of the charge-spin interaction in these systems has created challenges with both identifying and quantifying mechanisms for interaction, especially within the regime of reduced dimensionality [1]–[4]. In order for these systems to realize device applications and continue the progress of energy-efficient MRAMs, it is imperative to improve the understanding of how these two order parameters interact. The way toward achieving strong magnetoelectric coupling is not only a matter of careful selection of materials and properties, but also careful selection of characterizing techniques to analyze the interaction. Moreover, it is common to characterize these structures based on the direct association of effects on magnetization by varying the ferroelectric order. These methods have included the use of VSM, SQUID, MFM, and MOKE to characterize the magnetic response to applied electric fields.

## *1.2 Overview*

In section 2.3.1 we explore an example of a bilayer magnetostrictive/piezoelectric (FeGa/BTO) structure that exhibits strain-mediated magnetoelectric coupling. Here, direct LTEM observation of controlled and reversible switching of magnetic domains using electric fields is reported. This in situ observation technique allows the direct association of observed magnetization dynamics with a range of applied electric fields. It is observed that during application of ~7-11 MV/m electric fields to the BTO film, local magnetic domains rearranged in the FeGa due to transfer of strain. Simulations and calculations reveal the magnetic anisotropy varied from zero up to 25 kPa with the electric field range.

Thus, a mechanism for a MRAM magnetoelectric memory is proposed. Nanometer-scale magnetoelectric memory nodes are simulated to either reduce or negate their coercivity for magnetic polarization through altering their respective magnetic anisotropy with electric field. This effectively addresses the scaling conundrum in the requirements of magnetic media for use in MRAM devices. High anisotropy media is desired for bit stability but require large currents, and therefore power for writing. On the other hand, low anisotropy media are desired for reduced coercivity, but become thermally unstable with reduced bit dimensions. Magnetoelectric coupling can therefore provide a means for achieving the desirable attributes of both low and high anisotropy magnetic media. Here, the potential of magnetoelectric coupling in composite structures is demonstrated, addressing both of the needs for reduced power and scalability towards a universal memory.

Nevertheless in order for magnetoelectric memories to realize device implementation, an understanding of the mechanism needs to be gained to impact localized control of magnetic order. The essence of the magnetoelectric effect in some composite structures lies at the interface of the two material phases, where, in the case for strain-mediation, deformations in the crystal structure of the piezoelectric create magnetization events in magnetostrictive film. Therefore, understanding the nature of the strain transfer and how it impacts magnetic order is needed for the progression of these devices.

Section 3.3 details the work completed towards this goal, where direct application of strain via mechanical interactions to magnetostrictive films may help identify improved means for controlling the magnetic domains. Thin films of magnetostrictive FeGa– supported by flexible, free-standing silicon nitride membranes– are directly deflected with an external scanning-probe, inducing local strains in the magnetic film. Resulting magnetization dynamics are observed in situ with Lorentz-force transmission electron microscopy.

The magnetic hysteresis of the film is documented with attention to both applied magnetic field and applied strain, which both impact the local remanence. We directly observe the competition between the anisotropies generated with external strain, and that inherent in the magnetic film (through uniaxial anisotropy and magnetostatic interactions between the grains that compose the film).

We initiate the theoretical investigation of the hysteretic behavior in section 4.3 with an object-oriented micromagnetic model with an applied strain that varies inversely

with space. Further development of the spatial variance of the applied strain show that the strain varies only slightly over the film; modeling of the system suggests a more complex interaction of the various anisotropies. Introducing a threshold for the onset of the effects of the applied strain provide a model that most closely resembles the data, and implies that applied strains must either be strong enough to dominate the effective anisotropy, or one must reduce the threshold, for example, with applied magnetic fields. The imposed threshold model demonstrates how small variations in magnetization, inherent in polycrystalline thin films, impacts the onset of magnetoelastic effects, and methods to enhance the effect are explored.

Ultimately, the goal is to envision how strain-mediation of magnetic order can improve the energy-efficiency of MRAM devices and also enhance their scalability. Thus, it is important to consider these interactions on a scale for memory implementation. Patterned magnetic media– either through lithographic or directly fabricated nanostructures (such as magnetic nanoparticles)– is an area of increasing interest for realizing methods to increase scalability of magnetic media. Therefore it is appropriate to explore the strain mediation in patterned media, where shape anisotropy can dominate the overall magnetic character. The initial stages of investigating direct mechanical interaction on patterned media are also accounted in section 3.3.3.

# Chapter 2: Background

## *2.1 Introduction to Memory Technology*

### *2.1.1 Current Market Status*

Increasingly, our everyday lives depend on electronic technology for the creation, availability, and accessibility of digital data.  Innovations in today's electronics market are driven by the ubiquity of mobile computing and connectivity via platforms such as smartphones, tablets, and many other portable sensors [1]. For the first time in the history of the semiconductor industry, technological innovations are driven by mobile systems in lieu of computers, as seen in **Figure 2-1** [1]. The convenience and reliability of current mobile devices presents new challenges in order to advance to the next generation electronic devices. Because most of these devices rely on battery power, energy efficiency is essential along with their scalability. Lower power consumption, high computing performance, and affordable product cost are needed in order to advance the mobile computing systems market.
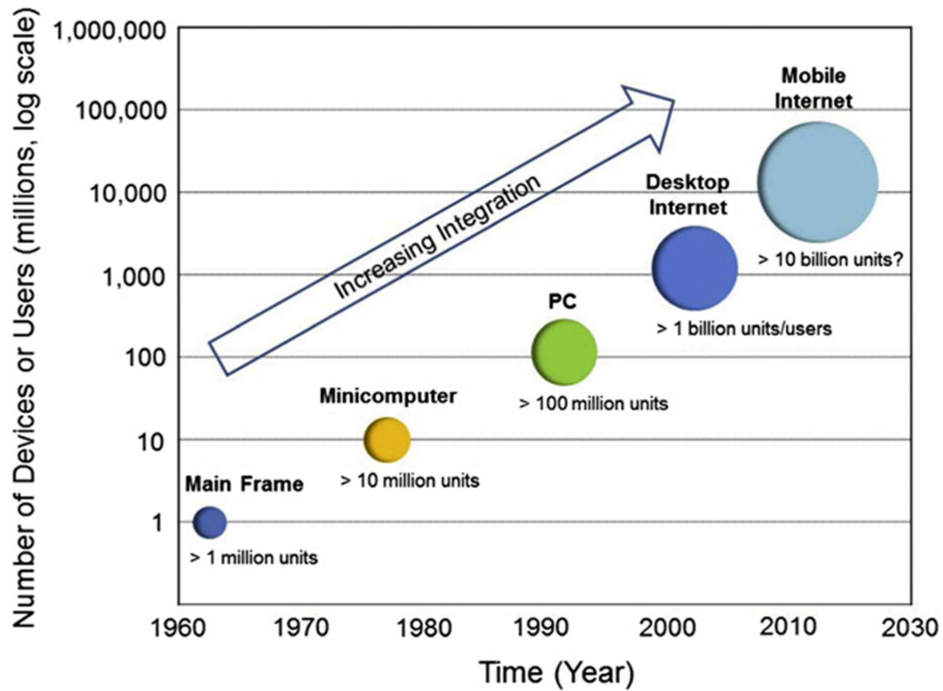
**Figure 2-1. Growth drivers for computing and connectivity over time. The current trend is classified as the era of mobile internet computing. Taken from** [5]**.**

The modern computing systems industry is founded on the back of silicon-based semiconductor devices. Arranged as *integrated circuits* (ICs), these devices enhanced electronic computing, allowing for the manufacture of very complex, high-speed, and reliable computers. The most important device for advanced ICs, reported in the early 1960's by Kahng and Atalla, is the metal-oxide-semiconductor field effect transistor (MOSFET) [6], [7]. The MOSFET consists of a MOS structure that serves as a gate, and two p-n junctions as the current source and drain. The first demonstration of the device had a gate length of *20 μm* and a gate oxide thickness of *100 nm*, and for several decades silicon-based transistors have steadily evolved towards smaller and denser features. This gradual shrinking of devices, has been influenced since 1965, is known as Moore's Law. Present day MOSFETs have been successfully scaled to the submicron regime. However,

as the industry explores IC designs beyond *20 nm*, we begin to encounter limits to this conventional device scaling. Major fundamental device challenges arise, including high leakage current, performance saturation, increased device variability and process complexity [1], [8]–[13]. These issues translate to problems in power dissipation, performance, and cost for a wide range of IC products. While Moore's Law scaling is not yet fully realized, as we approach the nanoscale, growing technological and economic concerns compromise its merit.

In electronics, the term *memory* is known as the ability to store digital information. In computer systems, memory is generally divided into two categories – primary storage and secondary storage [7]. Secondary storage, or external memory, is used for the long-term storage of information –such as programs, files of data– or files of latent information. This class of memory generally employs memory technologies consisting of magnetic media for nonvolatility of recorded data.

On the other hand, primary storage, or internal memory, is used in processing for temporary storage of data, program, and information. During the execution of a data process, information and data are exchanged between the external and internal memory components as system inputs and outputs; the internal memory serves as a temporary holding place for data during the program execution. Ultimately, the data results of the processing are returned to external memory for permanent storage. Internal memory units of a computer system are generally semiconductor memories based on electric charge storage [7], [10]. Semiconductor memories are noted over their magnetism-based competitors for: smaller and denser ICs, higher operating speed, low power consumption, and lower production costs. These merits give semiconductor memories a competitive

edge over magnetic memories in the market. It is for these reasons that electronic

memories, such as random-access memory (RAM) and solid state flash memory, are the

dominant memory types in modern microelectronic devices. However, neither electronic

nor magnetic storage can universally satisfy all of the requirements of computing

systems, and are often used in conjunction with one another in larger computing systems;

small computing devices generally utilize solely electronic memories.

These design requirements for computing systems have dire implications for their

energy efficiency. It is recognized that an IC, even when idle, will waste a substantial

amount of energy. Because the main IC components are MOSFET logic devices, energy

is lost due to leaky logic devices and volatile memory [1]. **Figure 2-2** depicts current and

future power consumption trends for a mobile system-on-chip (SOC) [14]. As the

microelectronics market drives toward small, compact mobile devices, it is clear that the

energy demands of the memory component present a serious challenge in the

downscaling of device size; these energy demands also compromise the functionality of

larger computing systems, and for connectivity systems designed to always be on and

connected.
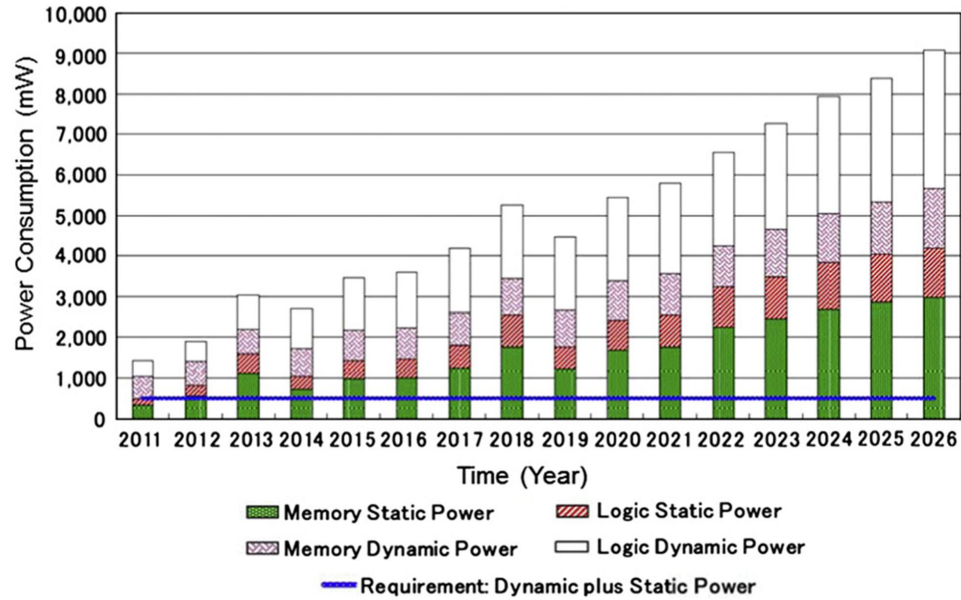
**Figure 2-2 Mobile SOC power consumption trends. Taken from** [14]**.**

The solution to this problem lies in the realization of a non-volatile SOC. However such a system remains elusive, as these fundamentals are not inherent in conventional MOSFET or memory technology. Industry-wide research and development efforts are in pursuit of an innovative, nonvolatile memory in lieu of conventional memories that are facing tradeoffs in performance and power, and also nearing the fundamental scaling limits. One of the most compelling candidates is emerging from the field of spintronics– a particular device consisting of a dense array of nanoscale magnetic tunnel junctions (MTJs) integrated with complimentary metal oxide semiconductor (CMOS) circuits [1], [8]–[17]. The following sections examine past, current, and next-in-line market trends in both semiconductor and magnetic memory classes.

### 2.1.2 Semiconductor-based Memory Technologies

Semiconductor type memory devices dominate the memory market. In this type of memory, data is stored in electric circuits as voltage or current levels. In the electronics industry, random-access read/write memory devices are referred to as RAMs. Storage locations in RAM can be accessed in random order; however, data stored in RAM is not permanent, that is, they can be altered and are volatile. RAMs are able to both write new data in a location for storage, and read data back out for use in processing [7]. Due to this versatility in read and write features, RAM is the most widely used electronic memory in applications where data frequently changes. However, RAM is a volatile memory; therefore, in removing the power supply from the IC, the data is lost. These RAM features allow the technology to appear in devices in conjunction with other non-volatile memories, or operate as the sole memory feature in devices where data recovery is not desired.

The combinatorial logic functions of a RAM design include address input bus, data input and output buses, and control input bus. The binary word input over the address bus lines select the storage location within the RAM module to which data is to be written or from which data is to be read. When data is to be written or read, it follows the data input or output bus lines. The control bus moderates addressing (data entry), chip selecting (data output), and read/write control (signals read or write operations) [7].

There are two basic categories of RAM: static RAM (SRAM) and dynamic RAM (DRAM). Both of these memories are classified as volatile as the logic is stored as two distinct charge states. A SRAM memory cell consists of four to six MOSFETS, making it the larger of the two RAM classes. Historically, four-transistor, two-resistor (4T2R)

11

SRAM cells have been used, and are suitable for medium to high performance

applications. However, four-transistor cell designs exhibit relatively high leakage

currents, and thus require higher standby currents for data preservation. Consequently, a

six-transistor (6T) SRAM memory cell has become more prevalent as it is more stable,

and has lower leakage and standby currents [18]. Thus 6T SRAMs are favored for

portable electronic device applications.
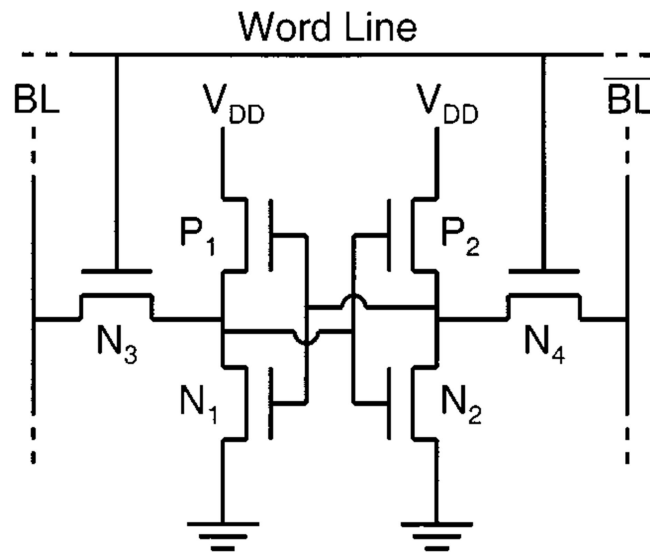


**Figure 2-3 6T SRAM cell circuit schematic. This represents one memory cell. Taken from** [19]**.**

**Figure 2-3** illustrates a 6T design [19]. Each bit is stored on four transistors ($P_1$,

$P_2$, $N_1$, $N_2$) that form two cross-coupled inverters, also known as a *flip-flop* circuit. Here

the N-channel MOSFETs, $N_1$ and $N_2$, are the active switching elements while the P-

channel MOSFETs, $P_1$ and $P_2$, act as load resistors for $N_1$ and $N_2$. This storage cell has

two stable states, which are used to denote 0 and 1 as binary logic. The two additional

MOSFETS, $N_3$ and $N_4$, act as gates to control the access to a storage cell during read and write operations. These two gates are turned ON and OFF by the word line [7], [18]–[20].

To write data into the cell, the gate leads of MOSFETS $N_3$ and $N_4$ must be held positive. This is accomplished by selecting the cell by its word and column line. In this manner, the drain lead of MOSFET $N_1$ connects to bit line $BL$ and the drain of $N_2$ to bit line $\overline{BL}$. Through forcing $BL$ to logic 1 and $\overline{BL}$ to logic 0, $N_2$ is turned ON and $N_1$ OFF. When the transmission gates are turned back OFF, the flip-flop remains in this state. Thus the cell holds new data. The read cell operation is performed in a similar manner. The access gate transistors are turned ON, but instead of applying data to the bit lines, the sense amplifier is enabled to read the status of $BL$ and $\overline{BL}$. A logic state representing the data held within the cell is produced at the output of the sense amplifier [7], [18]–[20]. While a cell is not addressed for either read or write cycles, it remains in a standby state. If the word line is not activated, the gate transistors $N_3$ and $N_4$ isolate the cell from the bit lines. The two flip-flop inverters will continue to reinforce each other as long as they are connected to the power supply.

SRAM memory cells are commonly employed as cache memories on microprocessors, a tribute to their relatively fast access and programming times. With cells consisting of up to 6 transistors, SRAM is the largest among the prevalent electronic memories (DRAM and Flash memory). Condensing the cell size presents issues with current leakage, which impacts the balance between the two cross-connected inverters, and thus can lead to bit failure.

Dynamic random access memories (DRAMs) use charge storage on a capacitor to represent stored binary data values of logic 0 or logic 1. In opposition to "static" RAMs,

13

DRAMs are termed "dynamic" because the stored charge leaks away even with
continuous power application. Because of this, the cells must be periodically read and
refreshed. Intel™ introduced the first commercial DRAM chip in 1970, using a three-
transistor (3T) cell [18]. However, the switch from three-transistor to one- transistor
design marks a milestone in DRAM evolution. In general, as the number of transistors
per cell decreases, so does the areal size of the cell. Small cell size is essential for high-
density ICs; therefore, the less area occupied by a cell, the better. As a result, an
advantage to 1T1C DRAMs is their large storage capacities (1 Mb and higher) [18].
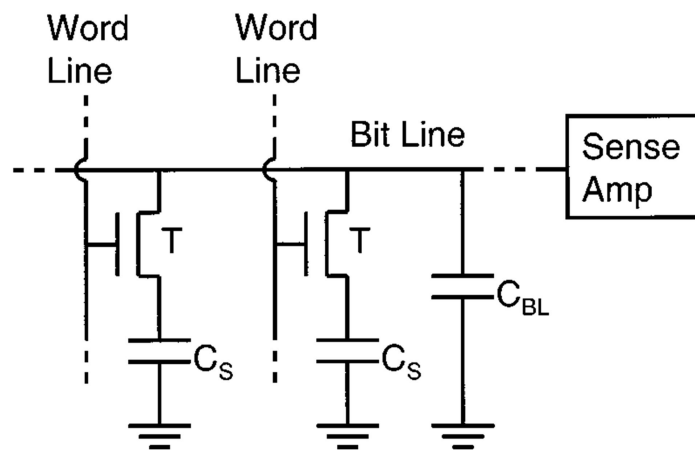


**Figure 2-4 DRAM circuit schematic. Two 1T1C cells are depicted. Taken from** [19]**.**

**Figure 2-4** represents a two-cell 1T1C circuit design [19]. Here data are stored on
capacitor $C_S$. Each capacitor is accessed through a transistor T connected to an array of
bit lines and word lines. To read data from the cell, the word line is set to select the cell,
turning ON the access transistor. The logic level represented by the charge stored on $C_S$
is dumped to the bit line. The charge induces current on the bit line, which is detected as

14

logic 0 to 1 by a sense amplifier. The data must be restored to the cell after the reading

process. Writing is performed by driving bit line to the logic level of the data and

selecting the cell with word line. This causes $C_S$ to be either recharged or changed to the

new logic state. As the word line is deselected, transistor T turns OFF and thus, traps the

charge on $C_S$.

Refreshing of cell data is accomplished by applying a refresh voltage, which

represents the stored logic level, to the Bit Line. By turning ON the access transistor, the

capacitor is recharged [7], [18], [19]. Generally, extra circuitry is required to perform the

refresh operation, which adds complexity to the operating mode of this memory. Despite

this drawback, DRAMs have the advantage of their cost per bit and high densities,

making them the most widely used semiconductor memories in commercial

microelectronics [10], [18].

However, DRAM and other memories based on charge storage are gradually

approaching the physical limits of scalability. Although a new cell structure for DRAM

has been developed to overcome scaling challenges at 30 nm, future size reduction below

*20 nm* features is facing both technological and economic limitations [10]. Therefore, the

future of DRAM lies in the ability to reduce the amount of fundamental components that

make up the cell– a memory cell based on a transistor alone. This 1T0C device concept is

known as zero-capacitance RAM (ZRAM).

The functionality of the first-generation ZRAM is realized through a possibility to

store major charge carriers in the floating body of the transistor, hence negating the need

of an external charge storage component. This is achieved via impact ionization of

minority carriers close to the drain, generating the majority carriers. Consequently, the

threshold voltage is modified due to charge accumulation in the body of the transistor, thus creating the two states of a MOSFET channel (open and close) for a gate voltage between the two thresholds. The second generation of ZRAM exploits the properties of bipolar transistors. Here, current flows through the body of the structure, generating majority carriers through impact ionization for storage [10]. While ZRAMs boast longer data retention times, and thus enlarged programming windows, one disadvantage is the relatively high operating voltage needed to generate carriers through impact ionization. In order to improve the applicability of this memory to low-power devices, it is critical to reduce the operating voltage.

While RAMs are generally favored for their fast and versatile read/write mechanisms, moderate cell size and operating voltages, low manufacturing costs, and unlimited memory endurance, the data stored with these memories are volatile. Once the device is removed from a continuous power supply all data are lost. It is required for a universal memory solution to be non-volatile in order to host applications where data retention is desired.

Nonvolatile memories are characterized by their ability to retain stored data, even when power is temporarily interrupted, or when the device is left without power for extended periods of time. An ideal nonvolatile memory is one that offers high bit density, fast random access, low power consumption, and the lowest cost per bit. Flash memory is among the ranks of SRAM and DRAM in terms of its wide use in current market products. However, unlike its competitors, Flash memory is a non-volatile semiconductor-based memory technology.
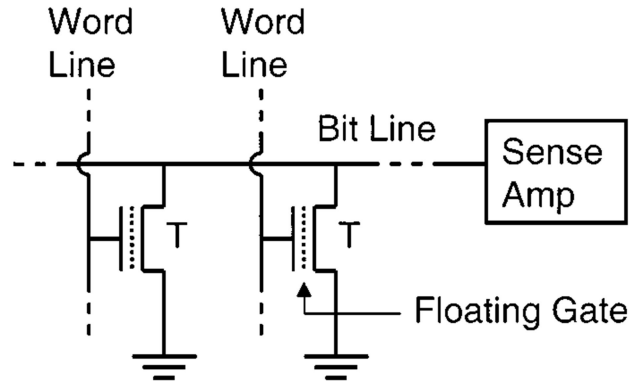
**Figure 2-5 Flash memory circuit schematic. Two memory cells are depicted. Taken from** [19]**.**

Flash memory cells operate through charge storage on a floating gate between the normal gate electrode and channel region of a MOSFET, as depicted in **Figure 2-5** [19]. Flash memory arrays are divided into two different chip architectures: NOR and NAND, which principally differ in their charge storage mechanisms. NOR cells use channel-hot-electron injection to program the floating gate. NAND cells use Fowler-Nordheim tunneling to program the floating gate. In each case, an applied electrical field adds or removes electron charge from the transistor's floating gate, effectively changing the threshold voltage that can be detected by sensing the current through the Bit Line while accessing the cell. Both technologies use Fowler-Nordheim tunneling to erase a cell [18], [19]. This tunneling mechanism directly adds or removes charge, enabling high-efficiency and low-power operation. In addition, NAND type memories are relatively dense because multiple bits are combined in a series string of cells, requiring a single bit line contact for the group. NOR requires a contact for each cell in the memory array.

However, both hot electron injection and tunneling processes are slow, yielding typical program times of *1 μs* and *10 ms*, respectively [19]. It is required that the

tunneling oxide be thin enough for reasonable write/erase times, but not so thin as to cause the charge to eventually leak off. The tunneling oxide must also be robust enough to tolerate $>10^5$ write/erase cycles during the product lifetime. These competing restrictions on the tunneling oxide imply limitations to the future scaling of Flash memory cells. The market is open to other contending nonvolatile memory technologies.

As mentioned earlier, SRAM, DRAM, and Flash memories dominate the market for microelectronic devices. While all three options find usefulness in niche applications as the sole memory mechanism, for many applications they must be supplemented with secondary memories in order to achieve the desirable device features. **Table 2-1** compares the key features of these memories, and highlights their shortcomings [12]. Of these options, Flash memory is the only nonvolatile option, and it suffers slow write speeds, limited endurance, and comparatively high operating voltages. None of these solid-state memories can provide all of the needed attributes in a single memory solution. Potential solutions to this dilemma are emerging from the industry of magnetic random access memory (MRAM) devices. In section 2.2, the fundamental principles and mechanisms of magnetic materials are briefly reviewed. These principles are then demonstrated in major developments in the evolution of MRAM. Select innovative technologies are highlighted in the review.

|            | SRAM      | DRAM      | FLASH       | MRAM          |
|------------|-----------|-----------|-------------|---------------|
| Read       | Fast      | Moderate  | Fast        | Moderate-fast |
| Write      | Fast      | Moderate  | **Slow**    | Moderate-fast |
| Nonvolatile| **No**    | **No**    | Yes         | Yes           |
| Endurance  | Unlimited | Unlimited | **Limited** | Unlimited     |
| Refresh    | No        | **Yes**   | No          | No            |
| Cell Size  | **Large** | Small     | Small       | Small         |
| Low voltage| Yes       | Limited   | **No**      | Yes           |

**Table 2-1 Comparison of MRAM features with other prevalent memory technologies. Bold letters indicate undesirable attributes. Adapted from** [12]**.**

## *2.2 Fundamentals of Magnetism*

Ferromagnetic materials possess a spontaneous magnetization, developing a magnetic moment at temperatures below the characteristic ordering temperature known as the Curie temperature $T_c$. These properties arise as a result of the electrons of an atom, which have magnetic moment by virtue of their angular momentum; both electron orbital and spin angular momentum contribute to the magnetic moment [21]–[26]. The magnetic moment of an atom is the vector sum of all its electrons' moments. In ferromagnetic materials, the cancellation of the electronic moments is only partial. Thus, a ferromagnetic atom is left with a net magnetic moment. This property is exploited in magnetic data storage technologies, and is the hallmark of spin-based electronics, or spintronics.

Magnetic ordering in ferromagnetic materials is a complex phenomenon, involving competing energies over different length scales. On the scale of the interatomic distance, a quantum-mechanical torque is responsible for ferromagnetic alignment of individual spins [21]–[26]. This torque depends on the relative orientation of spins with respect to one another; also known as the exchange torque. This interaction adds an extra term to the overall energy of a two-atom system, the exchange energy $A$ [21], [23], [27]:

$$E_{ex} = -2J_{ex}S_1 \cdot S_2 \quad \textbf{(Equation 2-1)}$$

where $J_{ex}$ is the exchange integral, and $S_1$ and $S_2$ represent the spin angular momentum of the two atoms. If $J_{ex}$ is positive, then $E_{ex}$ is a minimum when the spins are parallel and a maximum when they are antiparallel. If $J_{ex}$ is negative, the lowest energy state results from antiparallel spins. A positive value of the exchange integral is therefore a necessary condition for ferromagnetism.
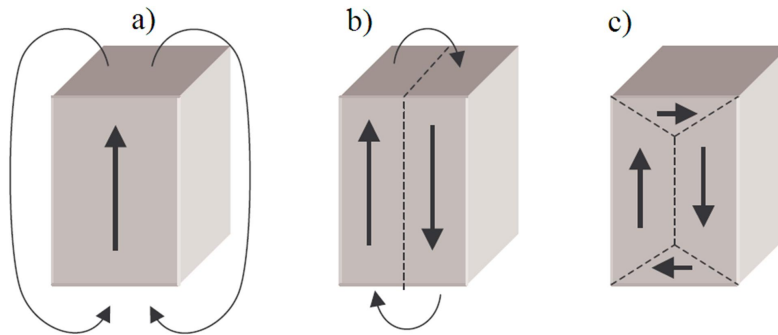
**Figure 2-6. Division of a crystal into domains. Taken from** [27]**.**

On a larger scale (*10-100 nm*), the finite dimensions of a ferromagnet cause the formation of magnetic poles, which increases magnetostatic energy. Subdividing the material into domains with alternating magnetization directions can lower the overall energy of the specimen [21]–[27]. Thus, this dipolar energy and the associated demagnetizing field are minimized by the formation magnetic domain structure, as is illustrated in **Figure 2-6** for a uniaxial crystal [27]. Each domain is spontaneously magnetized, but the directions of magnetization of the various domains are such that the specimen as a whole has no net magnetization. The process of magnetization thus becomes converting the specimen from a multi-domain state into one in which it is a single domain magnetized in the same direction of an applied field.
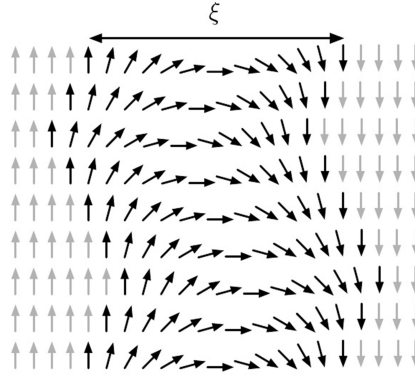
**Figure 2-7 Domains are separated by a transition region with thickness ξ. The direction of the magnetization changes gradually. Taken from [24].**

A domain wall– represented as dashed lines in **Figure 2-6** – in which the magnetization direction changes gradually, separates the domains. The two domains depicted in **Figure 2-7** are spontaneously magnetized in opposite directions, and are separated by a region of gradual spin transition [24]. Magnetocrystalline anisotropy ($K_1$)– a torque that tends to hold the magnetization in a preferred orientation (easy axis) as determined by the crystallographic directions in a crystal– competes with the exchange energy to set the width ($\xi$) of the domain walls, defined as [23], [24], [27]:

$$\xi = \sqrt{\frac{A}{K_1}}$$

**(Equation 2-2)**

The exchange energy tries to minimize the angle between neighboring spins, favoring a wide domain wall. Conversely, the anisotropy energy tries to minimize the number of spins that do not lie parallel to an easy direction, favoring a small domain wall. The ultimate width corresponds to the optimum distance that minimizes the total energy. As a result of this, anisotropic magnets have thinner domain walls (down to interatomic

distances), while magnets lacking anisotropy have domain walls with widths up to a few tens of nanometers.

As stated earlier, the energy of a magnetic material depends on the orientation of the magnetization with respect to the crystal axes, which is known as crystal anisotropy energy. This can be expressed in terms of a series expansion of the direction cosines of magnetization relative to the crystal axes [23], [24], [27]. In a hexagonal crystal, this energy depends on only the angle $\theta$ between the magnetization vector and the c-axis of the crystal, and can be described as:

$$E = K_0 + K_1 \sin^2 \theta + K_2 \sin^4 \theta + ... , \quad \textbf{(Equation 2-3)}$$

where $K_0$, $K_1$, $K_2$,... are constants for a particular material at a particular temperature and are expressed in terms of energy density. Higher powers are generally not needed, and sometimes $K_2$ is negligible. The first term has no angle dependence and is also usually ignored. Therefore this energy can be simply represented as, $E = K_1 \sin^2 \theta$ [23], [27].
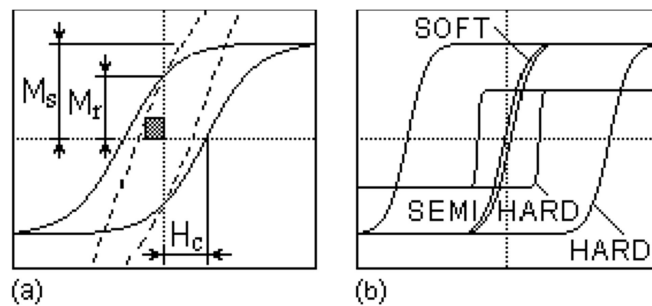


**Figure 2-8 Hysteresis loops. (a) Basic extrinsic properties derived from M-H loops. (b) Hysteresis loops of hard, semihard, and soft magnets. Taken from** [23]**.**

The magnetization of ferromagnets is characterized by a magnetic hysteresis loop,

whose most important parameters are the coercive field $H_c$ and the remanent

magnetization $M_r$. This characterizes the dependence of magnetization as a function of

the external field, illustrated in **Figure 2-8 (a)** [23]. In magnetization reversal, from

saturation in one direction to saturation in another, an applied field rotates the

magnetization $M_s$ of a single domain out of the easy direction, working against the

restoring force of anisotropy. The magnitude of $H_c$ depends on the materials impedance

to magnetization rotations in a particular direction. A hard magnet is described by a

"square-loop," with vertical or almost vertical sides, and magnetic remanence $M_r$ almost

equal to the saturation magnetization $M_s$, as depicted in **Figure 2-8 (b)**. A soft magnet is

described by an "S-shaped loop." The change of magnetization with external field is

almost linear over most of its range. Here, $M_r$ and $H_c$ are small or nearly zero [21]–[27].

In a polycrystalline material, the easy-axis directions vary from grain to grain, and

the magnetization may tend to follow these directions [22]–[24], [27]. If the grains are

oriented randomly in space, then the anisotropy of the individual grains will average out,

and the body on the whole will exhibit no crystal anisotropy. On the other hand, if the

grains have a preferred orientation, or crystallographic texture, then the body will have an

anisotropy dictated by the average of the individual crystals. The texture of a

polycrystalline material depends on its shape and how it was formed. In thin magnetic

films, the easy-axis of each grain tends to align parallel to the film surface; a large

demagnetizing field would act normal to the film surface if $M_S$ were oriented in that

direction [24], [27].
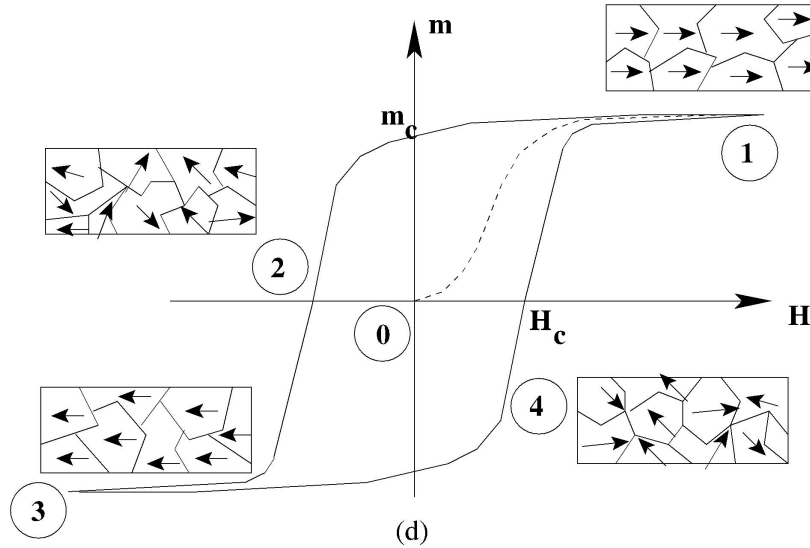
**Figure 2-9. Magnetization reversal and hysteresis for a polycrystalline magnet. Taken from** [25]**.**

The magnetization reversal of a polycrystalline specimen is represented in **Figure 2-9** [25]. The reversal mechanism in a thin ferromagnetic film is affected by its dimensionality [21], [24], [27]. Ordinary domain walls that exist in bulk materials are known as Bloch walls, and are characterized by magnetization rotation through the plane domain wall. While domain walls such as these are a possibly in thin films, the nucleation and propagation of magnetic domains is more likely to involve Néel walls when the thickness decreases; in Néel walls, magnetization transitions occur within the plane of the film. The magnetostatic energy of a Néel wall is less than that of a Bloch wall when the film thickness $t$ becomes less than the wall thickness $\xi$. This is described by the ratio of the magnetostatic energies associated with the two kinds of walls [27]:

$$\frac{\gamma_{ms,Bloch}}{\gamma_{ms,Neel}} = \frac{\xi}{t}$$

**(Equation 2-4)**

25

These various aspects of a particular material's magnetic nature compete to impact the overall magnetic behavior, and thus utility. These principles of magnetism at the nanoscale are the foundation of an increasing number of technological applications, especially within the industry of data storage. Memory technologies based on magnetic materials exploit the remanence, coercivity, domain structure, and atomic spin interactions for use in nonvolatile, high density, low cost, low-power consumption data storage devices. Next we explore a range of such technologies– past and prospective– and the possible gains toward a universal memory solution found in magnetic random access memories (MRAMs).

### 2.2.1 Magnetic-based Memory Technologies

Historically, memories based on magnetic materials have been an essential feature of digital data storage. Although semiconductor based memories have replaced their function in central processing units (CPUs), MRAMs have been the workhorses for secondary storage functions, and with recent increased R&D efforts, are anticipated to fill the gap of scaling-limited semiconductor memories. Key attributes of MRAM technology are non-volatility, and unlimited read and write endurance, thus having a functional edge over flash memory. In addition, it is anticipated that MRAM could operate at high speed and low voltage, with comparable densities. With continued progress in this class of memory, MRAMs could be poised to replace all other memories in various systems as a single, universal memory solution.

Magnetic bubble memory (MBM) technology emerged in the late 1970s, and was one of the most important developments in the memory industry. MBM is a solid-state memory device that stores data by remanent magnetization and serial access; meaning the

26

data access is non-mechanical.  The material and circuit processing techniques used for bubbles are similar to those used in semiconductor memories. Here, single-crystal materials (that are easier to grow than silicon), with higher bit densities, and less complex processing combine to make the bit per memory cost lower than conventional silicon integrated memories, and low enough to compare favorably with other mechanically accessed memory devices such as magnetic tape, magnetic disks, and magnetic drums.

Magnetic bubbles are mobile cylindrical domains that represent the logic states of digital data, instead of electrical voltages, currents, or charges. Bubbles are generated in a thin magnetic layer and are moved within the layer by interaction with patterned paths processed directly onto the layer and magnetized by external fields [7], [28], [29]. The presence of a bubble in a bit position, or bit period, represents logic 1, and the absence of a bubble represents logic 0.



NO EXTERNAL MAGNETIC FIELD    SMALL EXTERNAL MAGNETIC FIELD    LARGER EXTERNAL MAGNETIC FIELD
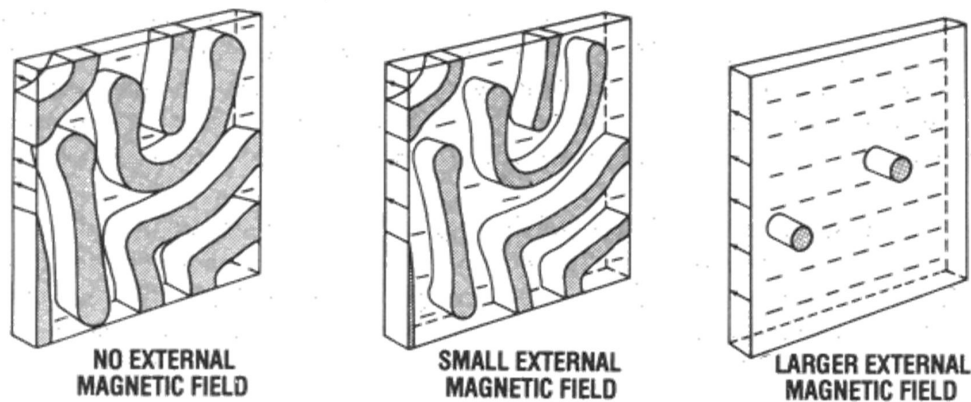
**Figure 2-10 Bubble formation within a MBM chip. Taken from** [28]**.**

The bubble chip is formed on a non-magnetic synthetic garnet substrate. The bit periods that represent the storage cells are formed in a thin film of synthetic garnet that is deposited on the substrate. Magnetic bubbles are cylindrical magnetic domains whose

magnetization is reverse to that in the remainder of the thin magnetic film. These domain configurations will only occur if the magnetic material has a uniaxial anisotropy with the easy axis of magnetization perpendicular to the surface. **Figure 2-10** illustrates the process for bubble formation within a MBM chip [28]. With no external field applied to the chip, the magnetic domains in the film form random, magnetically neutral patterns with equal area; this is known as serpentine pattern. As a small external magnetic field is applied, the domains, with polarity opposite to the field, shrink. Further increases in the magnetic field shrink the stripe domains into cylindrical configurations.
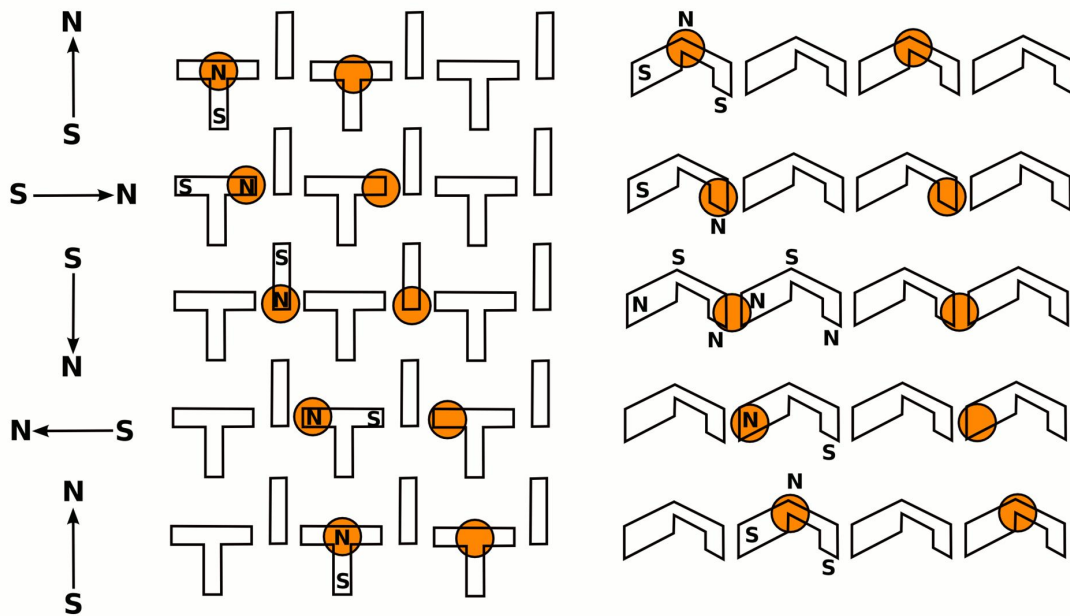


**Figure 2-11 T-bar (left) and chevron (right) propagation circuits. Adapted from** [28]**.**

In MBM, applying a varying magnetic field parallel to the film moves bubbles laterally through the film. To control the direction of movement, magnetic material is deposited on the surface of the film in the shape of a path. By sequentially magnetizing the propagation paths with a rotating magnetic field, provided with drive coils, the

magnetic polarity of the path elements are altered in order to pull bubbles through each element and down the path. This mechanism is depicted in **Figure 2-11** with both T-bar and chevron propagation paths [28].

While MBMs were characterized by their relatively high storage capacity and nonvolatility, their primary disadvantage was slow access times when compared to semiconductor memory, owing to the serial propagation process previously reviewed. The prospects of MBMs as a universal memory were truncated by their inability to be mass-produced in a cost effective semiconductor environment due to scaling and CMOS compatibility issues [30].

The application partially determines the success of a memory technology. As suggested in **Figure 2-1**, there has been a major shift in the use of memories away from desktop systems towards diverse mobile applications. The most successful area of growth in magnetic recording has been in hard disk drives (HDDs), which have saturated the desktop market, and are competing with flash memory in mobile markets [30]. HDDs have traditionally been used in computers since the late 1950s. The first generations of these devices were expensive and large. However, HDDs have successfully evolved over the following decades as gradually developments in their scalability have been overcome.
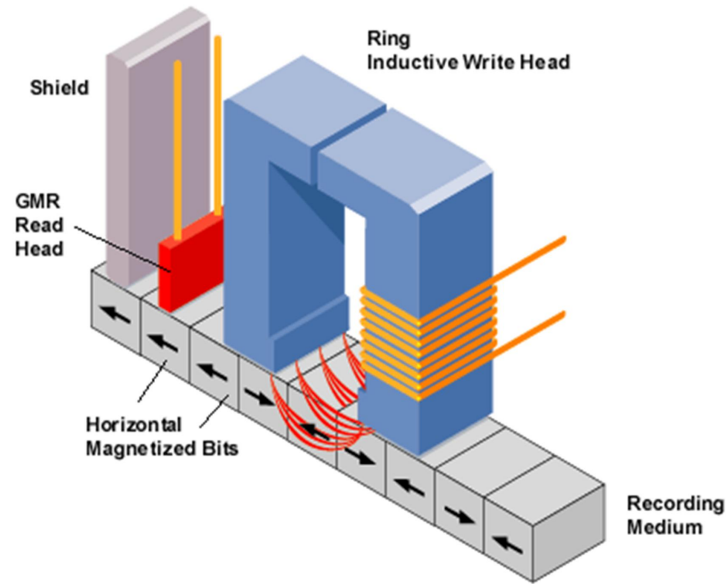
**Figure 2-12 Writing process in longitudinal recording** [31]**.**

HDDs were first engineered with a longitudinal recording mechanism. A magnetic pattern is written in narrow tracks into the recording medium as it moves past a writing head, which produces localized magnetic fields, as illustrated in **Figure 2-12** [31]. In longitudinal recording, the magnetization in the written information lies parallel to the layer surface and parallel to the track direction, where the two distinct orientations represent the binary logic. A read head that converts the sensed magnetic field from the media to electrical signals recovers the information.
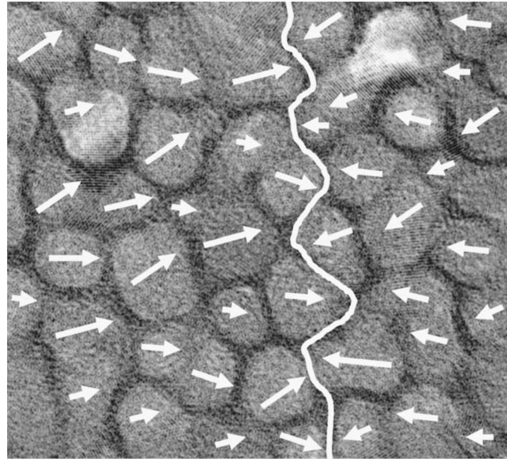
**Figure 2-13. Illustration of grains in polycrystalline magnetic recording media. Both the randomness of the easy-axis orientations, and the bit boundary are depicted. Taken from** [32]**.**

The magnetic recording media consists of deposited thin films, which are polycrystalline by nature of their formation. Therefore, the grains of the recording media have random positions and sizes, as is illustrated in **Figure 2-13** [32]. Consequently, the grains have random easy axis orientations. A group of grains are used to store information, and represent the fundamental logic element. The signal-to-noise ratio is the figure of merit in characterizing the potential bit density, which is a logarithmic function of the number of grains comprising a bit. Therefore, the key to increasing the storage capacity in HDDs has been reducing the grain size, or grain size distribution of the recording medium. This increases the number of grains in the bit area.

The energy that can be stored in one grain is $KV$, where $K$ is the magnetic anisotropy energy density and $V$ is the grain volume. This energy competes with the thermal energy $k_BT$ [33]. Therefore, the grain energy must be large enough to prevent spontaneous magnetization reversals, which lead to thermal decay and

superparamagnetism. The grain energy can be maintained for smaller grain volumes if the anisotropy energy $K$ is increased. High $K$ materials generally require a higher magnetic field to switch magnetization. The material that can be used to fabricate the poles limits the write head fields. To date, the maximum obtainable saturation magnetization is *2.4 T* [33]. This presents a three-fold challenge where efforts to increase SNR, maintain writability, and prevent thermal decay are in direct conflict with one another. This dilemma describes the scaling limitations of HDDs, and advances to further improve magnetic recording involve either a means to break these challenges or postpone them. The shift to perpendicular magnetic recording marked a significant boon in continuing HDDs on the market, and postponing these material issues.

Although conceptualized in the late 1970s, perpendicular recording did not obtain a place in the market for over 30 decades because of the success of longitudinal recording technology remained competitive. However with the threat of onset superparamagnetism with grain scaling for both technologies, attention was turned to the perpendicular writing scheme in efforts to delay the superparamagnetism limit. Eventually, the hard disk industry transitioned from longitudinal to perpendicular recording in the early 2000s, and has remained competitive by offering data storage capacities on the order of terabytes at ever lower cost [1], [33].
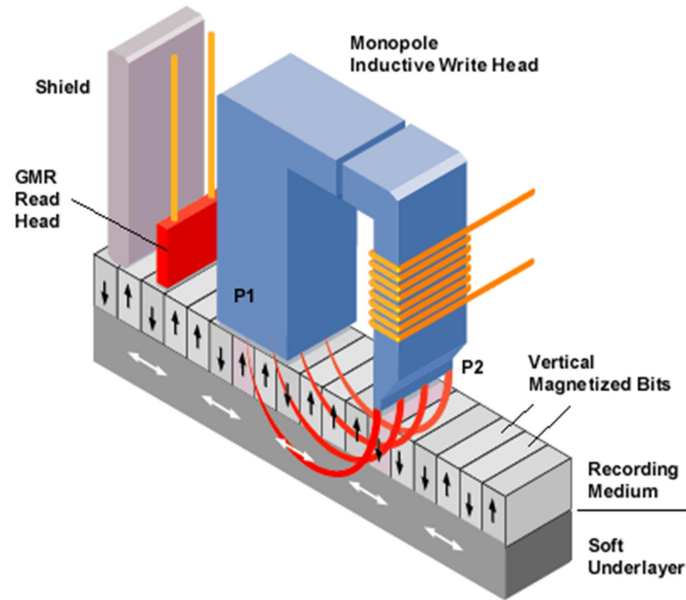
**Figure 2-14. Writing process in perpendicular recording. Taken from** [31]**.**

The fundamental concept of perpendicular recording is identical to that of longitudinal recording. The primary difference is that the magnetic medium is designed such that the easy axis magnetization in the media points perpendicular to the plane of the field in "up" or "down" configurations, as depicted in **Figure 2-14** [31]. The major advantages of perpendicular recording are that higher magnetizing fields can be applied to the recording medium (allowing for the use of higher anisotropy materials), and that the bit length can be reduced (packing more bits per unit length of track). Writing fields are generated with a single-pole head design. This modification requires the addition of a soft magnetic underlayer to the disk. This layer provides a path for the magnetic flux to return to the head. The return flux is diluted over a much larger area than the area of the writing gap. Thus, the field strength is much lower and is insufficient to alter prerecorded bits on the track [27], [32], [34].

Though the shift from longitudinal to perpendicular magnetic recording increased areal densities in HDDs, further progress in the down-scaling of both methods is threatened. As previously described, the superparamagnetic limit imposes a signal-to-noise ratio, thermal stability, and writability tradeoff. A promising approach to enabling large increases in the storage density of HDDs is heat-assisted magnetic recording (HAMR). Here, a write head modified with a laser is used to momentarily heat the media during the recording process. The heating process reduces the media coercivity below the available applied magnetic field from the recording head. The heated region is then rapidly cooled in the presence of the applied head field, where "up" and "down" magnetization orientations represent the binary logic as in perpendicular recording. The recording mechanism is illustrated in **Figure 2-15** [35].
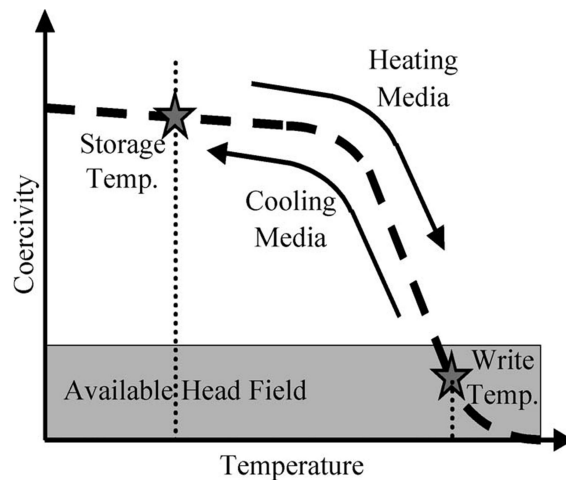


**Figure 2-15 Diagram of the HAMR write process. Taken from** [35]**.**

The heat-assisted method allows for the use of higher media anisotropy than is presently used in conventional perpendicular recording, and therefore thermal stability

*KV* is maintained as grain volume of the media is reduced. Further reductions in grain

volume can also be achieved with heat-assisted recording in patterned media. The effect

is demonstrated in **Figure 2-16**, where recording on high anisotropy media is

demonstrated both without and with heat assist [35]. Another principle attraction of

HAMR is a very high effective writing field gradient, which determines the width and

precision of the written bit, and is considerably higher with HAMR than can be achieved

with a magnetic writing head alone. This high effective head field gradient yields both

better-defined written transitions, and narrower and better defined track widths. For these

reasons, it is anticipated that HAMR will have a significant role in extending the areal

density potential of magnetic recording up to a factor of ten, after conventional

perpendicular recording reaches expected performance limits [35].
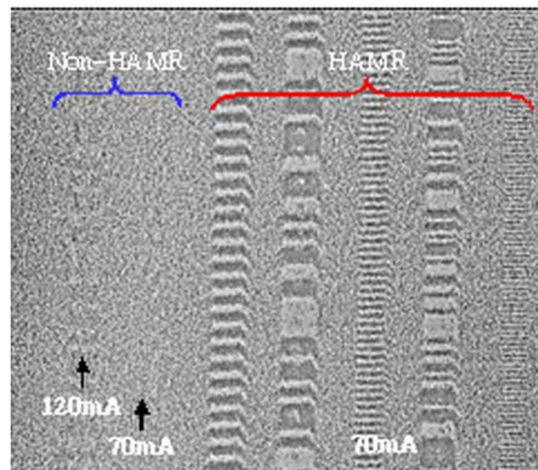


**Figure 2-16. Magnetic force microscopy image of high coercivity media being written without and with heat assist. Taken from** [35]**.**

HDDs, along with the promise of extended scaling of HAMR, have been the most significant application of high density, non-volatile magnetic recording. Perpendicular HDDs offer approximately one terabyte per square-inch storage capacities, and with developments in HAMR up to one hundred terabytes per square-inch can be achieved. However, HDDs require mechanical components (such as a spinning disk, and moving read and write heads), causing drawbacks such as limited access time, large form factor, and susceptibility to mechanical reliability problems [1]. Thus, solid-state memories (such as NAND flash memory) remain as strong market competitors, in particular for consumer products such as cellular phones, tablets, and notebook computers. A memory that works like a DRAM or SRAM, and is also nonvolatile is highly desired as a universal memory for these products.

Given the success of HDDs, MRAM still remains a possible cost-effective solution for long-term data retention. Electron-spin based data storage for on-chip memories has the potential for ultrahigh density, low power consumption, and high endurance. Another technology emerging from the field of spintronics, where the hysteretic behavior of electron spin in ferromagnetic materials is used to represent binary logic, is the magnetic tunnel junction (MTJ) [1], [8], [10]–[12], [15], [16], [36]–[38]. **Figure 2-17** is an illustration of the fundamental MTJ device structure [29]. The device consists of two ferromagnetic layers separated by a thin tunnel dielectric. One layer is "fixed," meaning that its magnetic orientation cannot be changed during operation. The magnetization of the reference layer is fixed by an exchange-bias interaction mechanism with an adjacent anti-ferromagnetic (AFM) layer (not pictured). The second layer is a soft ferromagnetic "free" layer, which can be changed by the application of a sufficiently

36

large magnetic field or spin-polarized current. The long axis of the free layer is oriented

parallel to the uniaxial anisotropy magnetic orientation of the fixed layer, resulting in a

magnetic orientation of the free layer in two stable states– in the same direction as the

fixed layer (parallel), or in the opposite direction (anti-parallel).
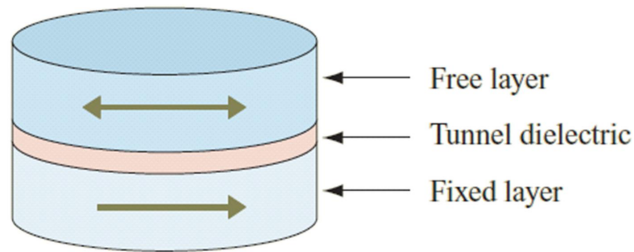


**Figure 2-17. Illustration of fundamental MTJ device structure, with indicated directions of layer magnetization. Taken from** [38]**.**

When a small bias voltage is applied between the fixed and free layers, a

tunneling current flows through the thin dielectric layer. The magnitude of this tunneling

current depends on the magnetic state of the free layer with respect to that of the fixed

layer. The parallel state has higher current, while the antiparallel state has lower current.

The MTJ is essentially a variable resistor, where the high and low current states represent

binary logic. The fractional change in the effective resistance is known as the

*magnetoresistance (MR)*, which is defined by:

$$R_{AP} = R_P(1 + MR) \quad \textbf{(Equation 2-5)}$$

where $R_{AP}$ is the effective resistance of the anti-parallel state and $R_P$ is that of the parallel

state [38]. *MR* values are typically between 30-50%, while novel materials in

development provide *MR* values in excess of 100% [38]. Due to the changes in current

37

density, MTJ resistance becomes minimum for the parallel magnetization state, and maximum for the anti-parallel configuration. This behavior is depicted in **Figure 2-18**, where the resistance is show as a function applied magnetic field to the cell [38].
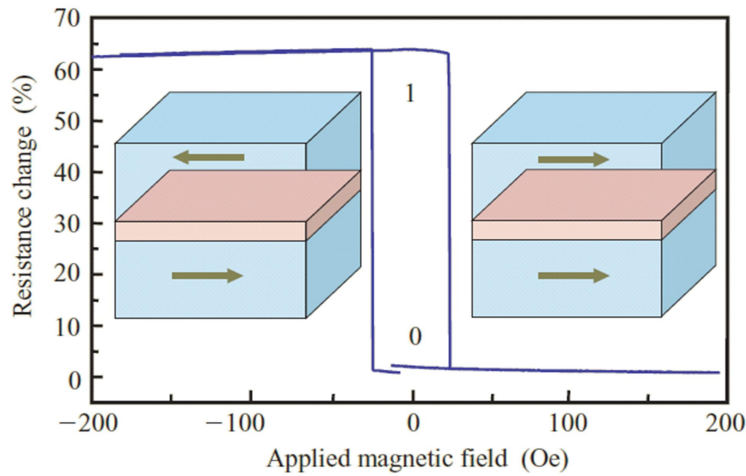


**Figure 2-18. MTJ device switching. Taken from** [38]**.**

The phenomenon giving rise to MTJ magnetoresistance is referred to as tunneling magnetoresistance (TMR), originally proposed by Julliere in 1975. It is a quantum mechanical phenomenon and was the result of spin-dependent tunneling [1]. The conductance of the metal-insulator-metal structure is affected by the electron density of states near the Fermi energy level that are available for conduction electrons. When conduction electrons are emitted from one ferromagnetic metal electrode (e.g. the fixed reference layer), they are spin-polarized to the magnetization direction of that electrode and tunnel through the thin barrier with their spin states conserved. The electron density of states in the opposite electrode (e.g. the soft ferromagnetic free layer) that the tunneling electrons encounter is dependent on the magnetization of the native layer.

Therefore, the conductance of the structure is determined by the relative orientations of the magnetizations. The tunnel magnetoresistance ratio (*TMR*) is thus defined as [1]:

$$TMR = \frac{R_{AP} - R_P}{R_p} \times 100\%$$

(**Equation 2.6**)
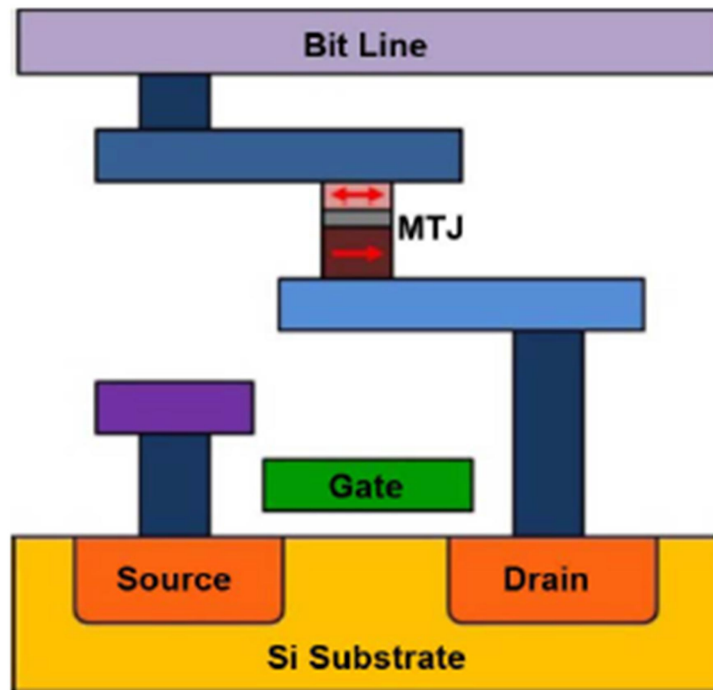


**Figure 2-19. Bit cell structure of STT-MRAM. Taken from** [37]**.**

A spin transfer torque based magnetic memory (STT-MRAM) device consists of an array of MTJs, coupled with transistors as access gates, and integrated with current carrying bit lines. A schematic of a 1T/1MTJ bit cell is depicted in **Figure 2-19** [37]. The word line activates and deactivates the transistor. When the transistor is on, charge current can flow through the MTJ when a voltage on the bit line and source line is different. The programming of a bit is accomplished through STT mechanism when

magnetization reversal occurs, or in other words, when the current density exceeds a threshold value known as the critical density $J_c$. An inherent asymmetry exists in switching an MTJ from parallel to anti-parallel compared to switching from anti-parallel to parallel. This is due to differences in the spin-reflection and scattering in both states, thus requiring different state dependent $J_c$ [1], [12], [15], [37], [38]. This process describes the mechanism of later-generation MTJ devices, where the prior generation of devices relies on current-induced magnetic fields to program the cell.
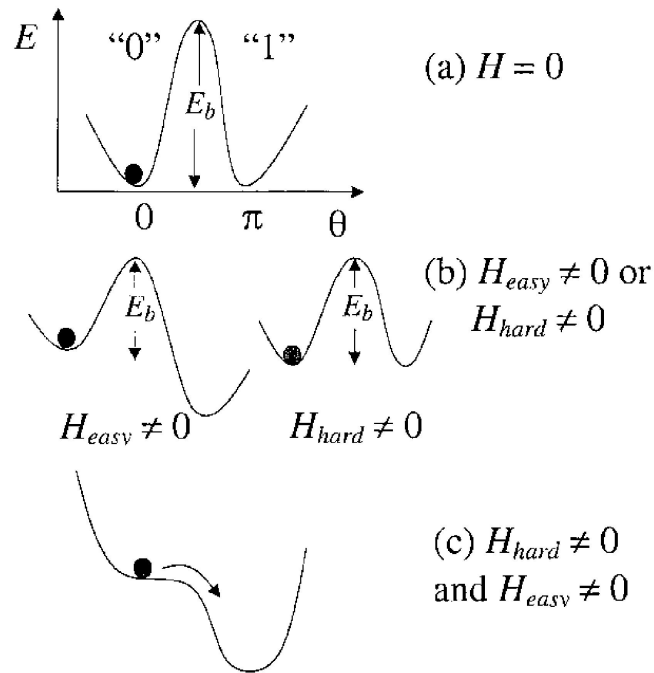


**Figure 2-20. Schematic of energy barrier $E_b$ that separates logic 0 from logic 1 in STT-MRAM cell. (a) In zero magnetic field, $E_b$ is maximum. (b) With applied field $H_{hard}$ or $H_{easy}$, $E_b$ is reduced. (c) With applied field $H_{hard}$ and $H_{easy}$, $E_b$ is reduced to 0 and the cell is programmed** [12]**.**

This mechanism of programming works by using the magnetic field generated by the passing current to reduce the energy barrier to magnetization reversal of the free layer. It is common that the bit of the MTJ cell is patterned with elongated shape, so that magnetic shape anisotropy creates an energy barrier ($E_b$) to magnetization reversal. The energy barrier is critical for the nonvolatility of the cell. The switching mechanism is depicted in **Figure 2-20**, where magnetic field manipulation of $E_b$ is used to program and preserve the bit [12]. The size of $E_b$ can be reduced with the application of a magnetic field along the easy-axis (parallel to the long axis of the cell) and hard-axis directions (transverse to the hard axis of the cell). As depicted, $E_b$ is a maximum with no applied field. With easy-axis ($H_{easy}$) or hard-axis fields ($H_{hard}$) applied separately, $E_b$ is reduced yet still finite. This is the case for those bits that are only exposed to fields from one line, or half-selected bits. With both fields applied, $E_b$ is reduced to zero, facilitating the programming of the bit that resides at that intersection.

MTJ based MRAM technologies possess a unique combination of high density, performance, and write endurance [38]. This technology is the most promising candidate for a future universal memory. However, a memory technology must be scalable to be economically viable. The current challenge in scalability for the STT-MRAM technology is to reduce the switching current density, which must generally increase with decreasing MTJ size to maintain data stability. A number of technology and design related developments are being researched in order to address this issue, including thermal-assisted switching for use with high anisotropy media [39]–[41]. However, additional developments need to be made in order to reduce the power required by this technology.

Developments to enhance the performance and scalability of MRAM technologies are still needed in order to compete not only as a universal memory, but also as a favored technology over popular DRAM, SRAM, and NAND Flash memories. Research efforts are pouring towards novel materials or technologies that can either improve these emerging devices or replace them. Because of this, attention has turned to the field of multiferroics and magnetoelectrics. These unique materials and structures offer the possibly to directly control the magnetic properties of a material through manipulating their electronic properties. Materials and devices that allow greater control over magnetic properties have potential to reduce power consumption in MRAM devices.

## *2.3 Introduction to Multiferroics and Magnetoelectric Coupling*
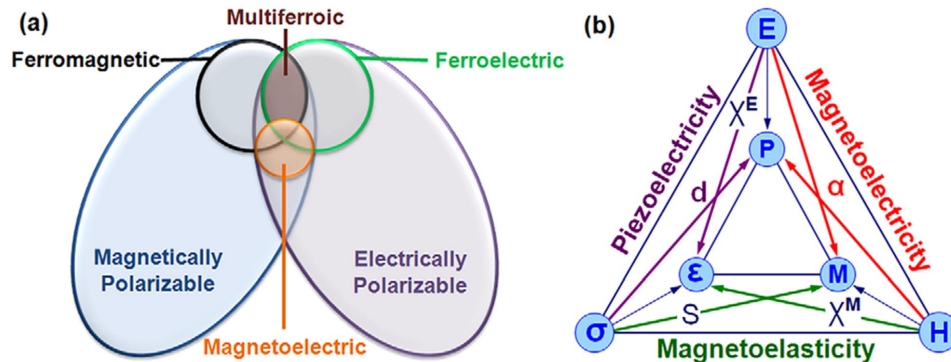


**Figure 2-21. (a) The relationship between multiferroic and magnetoelectric materials. (b) Schematic illustrating different types of coupling mechanisms present in materials. Much attention has been given to materials where electric and magnetic order parameters are coupled. These materials are known as magnetoelectric materials. Taken from** [42]**.**

The quest for a universal memory solution has re-energized the field of multiferroics and magnetoelectrics in the last decade, since pioneering research in the 1950s and 1960s [2], [3], [42]–[48]. A single-phase multiferroic material is one that simultaneously possesses two or all three ferroic order parameters: ferroelectricity (spontaneous polarization that is stable and can be switched hysteretically by an applied electric field), ferromagnetism (spontaneous magnetization that is stable and can be switched hysteretically by an applied magnetic field), and ferroelasticity (spontaneous deformation that is stable and can be switched hysteretically by an applied stress).

The overlap of coupling mechanisms required of theses materials to be classified as multiferroic and coupling mechanisms is depicted in **Figure 2-21** [42]. Here we see that only a small subgroup of all magnetically and electrically polarizable materials is either ferromagnetic or ferroelectric. Fewer still simultaneously exhibit both order parameters. In these select materials there is a possibility of magnetoelectric coupling. Magnetoelectric coupling typically refers to the linear magnetoelectric effect, or the induction of magnetization by an electric field or polarization by a magnetic field. Magnetoelectricity is an independent phenomenon that can arise in any material with both magnetic and electric polarizability, regardless of whether it is classified multiferroic or not. Magnetoelectric coupling may arise directly between the two order parameters, or indirectly via strain. By definition, a magnetoelectric multiferroic must be simultaneously both ferromagnetic and ferroelectric [42], [47].

The magnetoelectric effect in a single-phase crystal is traditionally described in Landau theory by writing the free energy ($F$) of the system in terms of an applied magnetic field $\vec{H}$, and an applied electric field $\vec{E}$ [42], [47]:

$$-F(E,H) = \tfrac{1}{2}\varepsilon_0\varepsilon_{ij}E_iE_j + \tfrac{1}{2}\mu_0\mu_{ij}H_iH_j + \alpha_{ij}E_iH_j + \tfrac{\beta_{ijk}}{2}E_iH_jH_k + \tfrac{\gamma_{ijk}}{2}H_iE_jE_k + ...$$
(Equation 2-7)

The first term on the right hand side describes the contribution resulting from the electrical response to an electric field, where the permittivity of free space is $\varepsilon_0$, and the relative permittivity $\varepsilon_{ij}(T)$ is a second-rank tensor that is typically independent of $E_i$ in non-ferroic materials. The second term is the magnetic equivalent of the first term, where $\mu_{ij}(T)$ is the relative permeability and $\mu_0$ is the permeability of free space. The third term describes the linear magnetoelectric coupling via $\alpha_{ij}(T)$. The third-rank tensors $\beta_{ijk}(T)$ and $\gamma_{ijk}(T)$ represent higher-order (quadratic) magnetoelectric coefficients. These higher order terms are generally much smaller in magnitude than the lower order terms [42], [47].

The magnetoelectric effects can be obtained in the form $P_i(H_j)$ or $M_i(E_j)$ through differentiation and minimization of F with respect to its constituents. One obtains:

$$P_i = \alpha_{ij}H_j + \tfrac{\beta_{ijk}}{2}H_jH_k + ...$$
(Equation 2-8)

and

$$\mu_0 M_i = \alpha_{ji}E_j + \tfrac{\gamma_{ijk}}{2}E_jE_k + ...$$
(Equation 2-9)

Again, the higher order terms are generally small in magnitude when compared to the lower order terms. Thus, in practice magnetoelectric coupling is referred to as a linear effect, simply represented as $P = \alpha H$ (direct magnetoelectric effect) or $M = \alpha E$ (converse magnetoelectric effect). The magnetoelectric response is limited by the relation [42], [47]:

$$\alpha_{ij}^2 \leq \varepsilon_0\mu_0\varepsilon_{ii}\mu_{jj}$$
(Equation 2-10)

This is obtained from *Equation 2-7* by forcing the sum of the first three terms to be greater than zero, excluding the higher order coupling terms. This means that the magnetoelectric effect can only be large in ferroelectric and/or ferromagnetic materials because these materials often posses a large permittivity and permeability, respectively [42], [47].

The promise of coupling between magnetic and electronic order parameters, and the potential to manipulate one through the other has been the focus of much research toward spintronics. Here, the ultimate goal for device functionality would be a single-phase multiferroic with strong coupling between ferroelectric and ferromagnetic order parameters. This would allow for facilitated control over the magnetic nature of the material with an applied electric field. In other words, this coupling could permit data to be written electrically and read magnetically [42]–[46], [48]–[52]. Therefore, materials that exhibit magnetoelectric coupling could resolve issues with energy efficiency in magnetic data storage, where large currents are needed to create localized magnetic fields, or for spin-transfer torque mechanisms. However, significant materials developments are required to realize magnetoelectric materials that could make real contribution to the data storage industry.

Multiferroic materials that exhibit strong magnetoelectric coupling at room temperature are rare; this realization most likely explains the decline of research in this field after its peak in the 1960s. The scarcity of these materials is understood by investigating several factors — symmetry, electronic properties, and chemistry — that affect the functionality of these materials. There are only thirteen point groups in existence that can give rise to multiferroic behavior. Additionally, ferroelectrics by

definition are insulators. The conventional mechanism for cation-off centering requires ions that have a formal $d^0$ electronic state, or an empty $d$-orbital. However ferromagnets require conduction electrons; magnetism is mediated by partially filled $d$-orbitals. Thus there exists a contradiction between the traditional mechanism of off-centering in a ferroelectric and the formation of magnetic order, explaining the scarcity of ferromagnetic-ferroelectric multiferroics [4], [42], [47], [53]. The focus of research in this field has thus been in designing and identifying new mechanisms that can lead to magnetoelectric coupling.

Relatively recent advances in materials fabrication and characterization at smaller scales has breathed new life into the field magnetoelectric multiferroics, and has re-energized research for the ideal material and/or design. This is fueled by the following capabilities: production of high-quality single-crystalline samples, improved first-principles computational techniques for the design of new multiferroics, and advances in thin film growth techniques that have provided routes to structures and phases typically inaccessible by traditional chemical means [4]. Presently, two major sources for large magnetoelectric coupling have been identified: composite materials and multiferroics [42].

Despite these advances, few natural multiferroic single-phase compounds exist, and their magnetoelectric responses are either relatively weak or occur at temperatures too low for practical applications. Strong magnetoelectric coupling at room temperature has been realized in multiferroic composites. These structures combine ferroelectric and ferromagnetic phases, offering great design flexibility. In magnetoelectric composites, neither of the constituent phases are inherently magnetoelectric, but the cross interaction

between phases produces the coupling as an extrinsic effect. Magnetoelectric coupling in these types of structures produce responses several orders of magnitude higher than those in single-phase magnetoelectric materials currently available [43], [44], [54].

The magnetoelectric effect in composite materials is known as a product tensor property, which results from the cross interaction between different orderings of the two phases in the composite [43], [44], [54]. The phases that make up the composite are generally piezoelectric — materials that experience a change in strain as a linear function of applied electric field, or a change in polarization as a linear function of applied stress – – and magnetostrictive — materials that experience a change in strain as a function of applied magnetic field, or a change in magnetization as a function of applied stress. Again, neither the piezoelectric nor magnetic phase has magnetoelectric effect. Thus the magnetoelectric effect is a result of the product of the magnetostrictive effect (magnetic/mechanical) in the magnetic phase and the piezoelectric effect (mechanical/electrical) in the piezoelectric phase [43], [44], [54]:

$$DirectMEeffect = \frac{magnetic}{mechanical} \times \frac{mechanical}{electric}$$ **(Equation 2-11)**

$$ConverseMEeffect = \frac{electric}{mechanical} \times \frac{mechanical}{magnetic}$$ **(Equation 2-12)**

This represents a coupled electrical and magnetic phenomenon via elastic interaction. That is, for the direct effect, when a magnetic field is applied to a composite the magnetic phase changes its shape magnetostrictively. The strain is then transferred at the interface to the piezoelectric phase, resulting in an electric polarization — and vice versa for the converse effect. Thus the magnetoelectric effect in composites is extrinsic depending on the composite microstructure and coupling interaction across the magnetic-

piezoelectric interface. That is, the strength of the coupling in composite structures is not restricted by $\alpha_{ij}^2$, and each phase may be independently optimized for room temperature performance.

The response observed at room temperature in such composites has high technological viability, and has potential to be used as a principle mechanism in spintronics devices. Various magnetoelectric composites in different systems have been investigated in recent years, including (1) bulk ceramic magnetoelectric composites of piezoelectric ceramics and ferrites; (2) two-phase magnetoelectric composites of magnetic alloys and piezoelectric materials, (3) three-phase magnetoelectric composites, and (4) thin films (nanostructured composites) of ferroelectric and magnetic oxides [54].
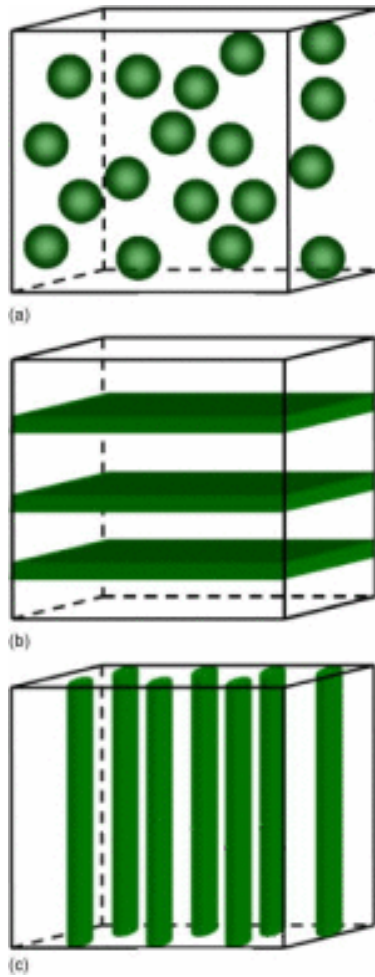
**Figure 2-22. Three common connectivity schemes in two-phase magnetoelectric composites: (a) 0-3 particulate composite, (b) 2-2 laminate composite, and (c) 1-3 fiber/rod composite. Taken from** [44]**.**

Strain coupling requires intimate contact between a piezoelectric and a magnetostrictive material. Two-phase composite structures are described by their phase connectivity using the notations 0-3, 2-2, 1-3, etc., in which each number denotes the dimension of connectivity of the respective phase. For example, a 0-3 type particulate composite describes one-phase particles (denoted by 0) embedded in the matrix of another phase (denoted by 3). These connectivity schemes are depicted in **Figure 2-22** [44].

There are three principle mechanisms for the magnetoelectric response in 2-2 type layered heterostructures: charge-mediation, exchange bias-mediation, and strain mediation [44], [54]. In heterostructures containing ultrathin ferromagnetic films, an electric field could result in the accumulation of charges (e.g. spin polarized electrons or holes) at the interface, which then produces a change in the interface magnetization as a consequence of spin-dependent screening of an electric field [54]. Molegraaf et al. have observed remarkable electric field control of magnetism via the charge- mediated magnetoelectric effect in a *PZT (250 nm)/LSMO (4 nm)* heterostructure [55]. Here the change in the valence state of Mn induced by electrostatic charge modulation demonstrates the electronic origin of the magnetoelectric coupling. Resulting from direct control of magnetism via charge carrier density, the magnetic behavior of the nanostructure shows a hysteresis response as a function of the applied electric field, as demonstrated in **Figure 2-23** [55]. This M-E loop demonstrates cross-coupling between ferroic ground states.
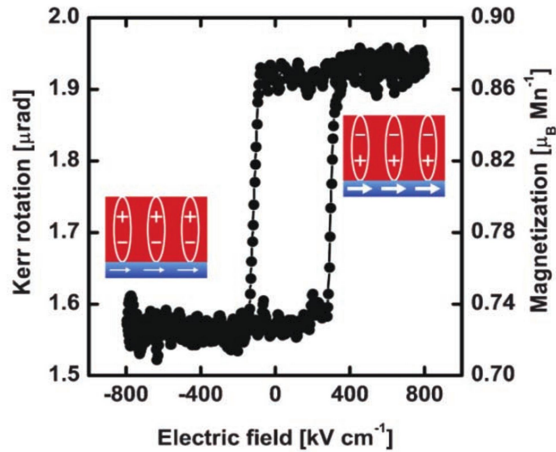
**Figure 2-23. M–E hysteresis curve showing the magnetic response of the PZT/LSMO heterostructure at 100 K as a function of the applied electric field, measured by a MOKE magnetometer. Insets represent the magnetic and electric states in the LSMO layer (blue) and PZT layer (red). Taken from** [55]**.**

Exchange bias, a result from the exchange coupling between the uncompensated interfacial spins of the antiferromagnet and the spins of the ferromagnetic layer, has also been used for electric field control of the magnetic properties in the ferromagnetic films. In the combination of multiferroic BFO with a ferromagnetic layer, an electrically driven change in ferroelectric polarization– and thus antiferromagnetic order through the ferroelectric-antiferromagnetic coupling in the multiferroic BFO– could switch the magnetization of an overlying thin ferromagnetic film by quantum-mechanical exchange [54]. In addition, an electrically driven change in the electrical polarization of a ferroelectric material that is also ferroelastic produces mechanical strain. This strain is transferred to the overlying ferromagnetic thin film. The resulting deformation could also modify the easy-axis anisotropy of the magnetic domains, and thus the macroscopic magnetization.
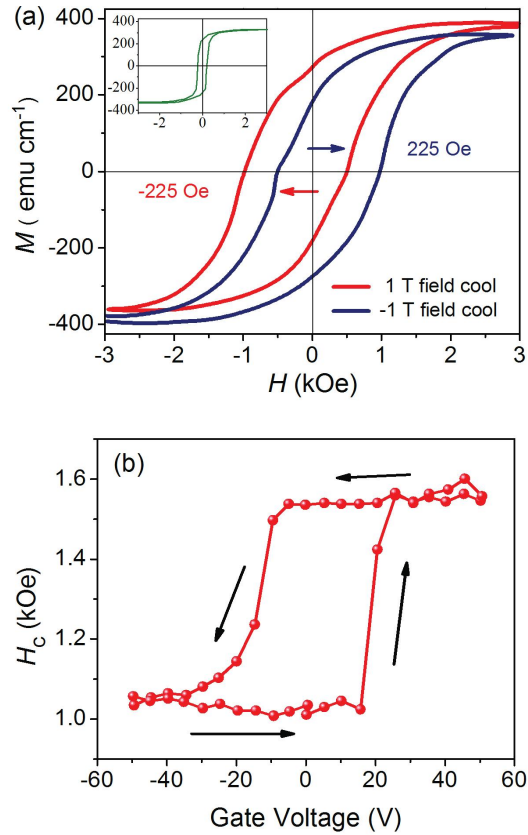
**Figure 2-24. (a) Magnetic hysteresis curves of the BFO/LSMO heterostructure measured by SQUID at 7 K after being field cooled from 350 K in 1 T (red) and in -1 T (blue). The inset shows magnetic hysteresis curve for a BFO/STO/LSMO structure with no exchange bias after field cooling. (b) Change of magnetic coercivity $H_c$ of the LSMO with respect to the applied gate voltage at 5.5 K. Taken from [56].**

Observation of reversible electric-voltage control of exchange-bias has been reported in a multiferroic *BFO/LSMO* epitaxial heterostructure by switching the ferroelectric polarization of BFO, as shown in **Figure 2-24 (a)** [56]. The exchange bias effect in this structure was postulated to arise from the induced interface magnetism in a few nanometers of the BFO layer as a consequence of an electronic orbital reconstruction occurring at the *BFO/LSMO* interface. Here, the strain effect on exchange bias was eliminated in this structure since no exchange bias existed in the *BFO/STO/LSMO*

heterostructure, as demonstrated in the inset of **Figure 2-24 (a)**. The magnetic coercivity $H_c$ of the LSMO was hysteretic with voltage applied to the BFO gate since small changes in the carrier density modified the magnetic properties in LSMO, as demonstrated in **Figure 2-24 (b)** [56].

As discussed earlier, the strain mediated magnetoelectric coupling in composite structures is one main route to achieve magnetoelectric coupling. An external electric field results in a change in shape of the ferroelectric phase through the converse piezoelectric effect during switching. The strain is passed on to the magnetic phase via the magnetostriction. Thus an electric field control of the magnetic behavior of the magnetic nanostructure can be achieved by a strain mediated magnetoelectric coupling. The magnetic films include either metallic (i.e. Fe, Ni, and Ni-Fe alloys) films or oxide-based (i.e. $Fe_2O_4$, CFO, NFO, and LSMO) films– and the ferroelectric substrates used are BTO, PZT, PMN-PT and PZN-PT single crystals or ceramics [54].
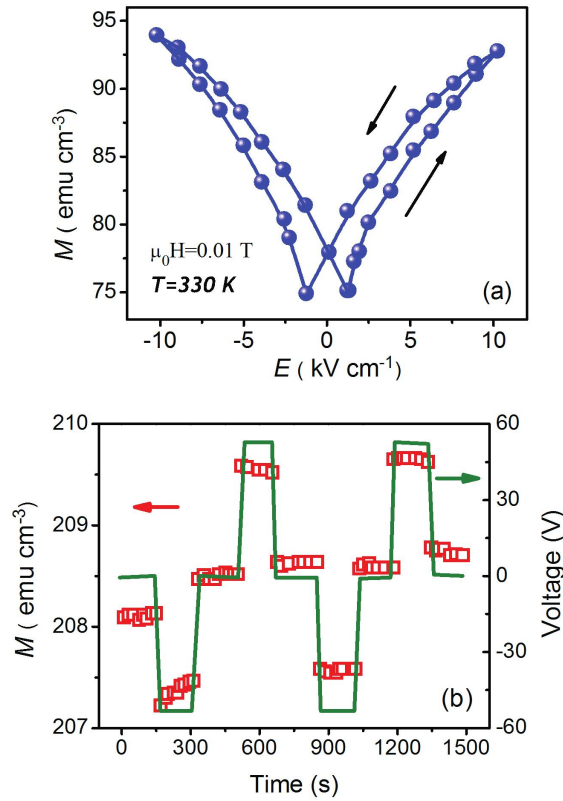
**Figure 2-25. (a) In-plane magnetization of LSMO film grown on single-crystal PMN-PT measured using VSM with external electric field E applied across the PMN-PT substrate** [57]. **(b) The in-plane magnetization M of CFO switches as a function of time with the electric voltage pulse applied on the single-crystal PMN-PT substrate. Taken from** [58].

Electric-field induced changes in M-H hysteresis loops were first observed in ferromagnetic LSMO films grown on ferroelectric single crystal substrates [54]. Thiele et al. observed an electric field modification of magnetization in a composite structure consisting of an LSMO film on a PMN-PT single crystal substrate [57]. By applying an electric field to reversibly compress the isotropic in-plane lattice parameter of the PMN-PT substrate, a large strain-mediated magnetoelectric coupling coefficient ~ *0.06 Oe cm V$^{-1}$* at ambient temperature was extracted from the M-E loop of this system, depicted in **Figure 2-25 (a)** [57]. Note, the M-E loop is butterfly-shaped, tracking the butterfly-

shaped piezo-strain curve of PMN-PT, demonstrating the vital role of the elastic strains for the converse magnetoelectric response in the heterostructure. Analogously, strain-mediate magnetoelectric coupling was reported in ferrite $Fe_3O_4$ and CFO films grown on PMN-PT single crystal substrates [58]. Butterfly-shaped M-E curves also suggest that strain-mediated magnetoelectric coupling plays a dominant role in the electric-field induced change in the magnetic anisotropy of the composite. Of particular interest, a reversible on-off switch (i.e. a high of low M state) of magnetism in the magnetic thin films is demonstrated (see **Figure 2-25 (b)**) [58].

In general, 2-2 laminate type structures are more realizable because crystallographic orientation, layer thickness, and interfacial roughness can be controlled accurately.  Here, different phases can be combined at atomic-level, and by precise control of the lattice matching, epitaxial composite films can be designed; facilitating understanding of magnetoelectric coupling at the atomic scale. However, conscious selection of appropriately matched materials is required in order to maximize the effect. Magnetoelectric coupling is a strain-mediated effect, and strain in these devices arises from differences in lattice parameters and thermal expansions between the films. Attention toward choosing an appropriate substrate with very small difference in lattice parameters from the desired materials, or physical arrangements to relieve substrate clamping in the device, is imperative to achieving large magnetoelectric response [4], [54]. Overall, composites of this structure are a promising mechanism for mediating control of magnetism for data storage applications with reduced power consumption and facile integration in CMOS on-chip designs.

In addition to the materials design of the structure, one must also consider an appropriate experimental method for measuring magnetoelectric coupling in thin films. The classical method for probing magnetoelectric coupling is to measure the magnetoelectric response ($\delta P/\delta H$ or $\delta M/\delta E$) directly as a function of temperature [4]. However, in thin films such measurements are complicated by leakage in dielectric, and small SNR. Because of these difficulties a variety of approaches have been developed to probe magnetoelectric coupling, many of which offer high spatial resolution. In regards to probing converse magnetoelectric effect, these methods include: vibrating sample magnetometry (VSM) or SQUID, magnetic force microscopy (MFM), magneto-optical Kerr effect (MOKE) magnetometry, and Lorentz-force transmission electron microscopy (LTEM).

### 2.3.1 Observation of reversible nanomagnetic switching induced by electric fields

Thus far we have discussed a variety of composite devices along with various connectivity schemes, and magnetoelectric coupling mediation mechanisms. The use of magnetoelectric coupling and multiferroics in spintronics is a rapidly emerging area of research, and a number of possible device architectures have been proposed [4], [44], [54]–[58]. Of these options, a flurry of research has been centered around 2-2 type interfacial heterostructures, where strain-mediation of magnetoelectric coupling is achieved through atomic-scale interaction between individual piezoelectric and magnetostrictive phases. This is due to advances in thin-film growth techniques (i.e. pulsed laser deposition (PLD), molecular beam epitaxy (MBE), and sputtering) have

provided routes to high quality and precise control of properties at the nanoscale. However, such structures are plagued by substrate clamping effects that limit the mechanical response of the constituents, and thus the overall magnetoelectric response. This leads to difficulty in controlling the local magnetization switching in these devices, which is required for a memory element. In order to fully understand the interactions that lead to magnetoelectric coupling, special care must go toward device fabrication, composition, and observation techniques.

The ultimate goal is to realize a device that exhibits strong magnetoelectric coupling for use in MRAM devices. Todd Brintlinger et al. reported such a device, where strain-mediated electric-field control of magnetization was observed in situ, in a bilayer structure [59]. They demonstrate through real time imaging of magnetic domain structures that the occurrence of individual magnetization switching events as an external voltage is continuously varied. The bistable magnetic states are reversible, which is ideal for applications towards magnetic memory.
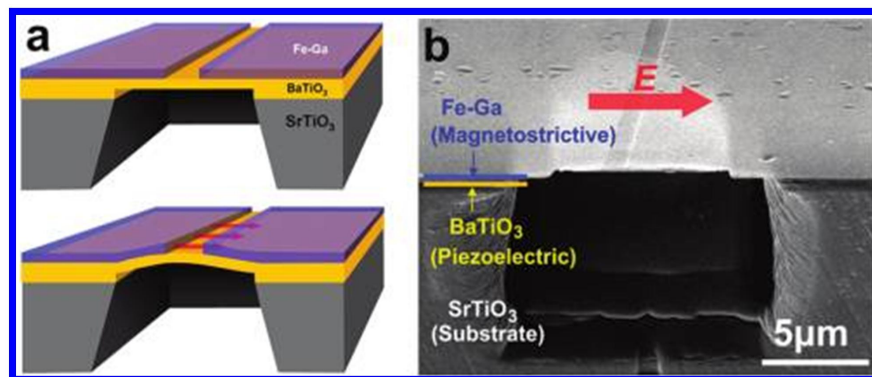


**Figure 2-26. (a) Schematic of FeGa/BaTiO$_3$ thin film bilayer structure. The bottom image represents the electric field (red arrows) that leads to mechanical response in piezoelectric BTO. (b) Scanning electron micrograph (SEM) of device. Taken from** [59]**.**

An epitaxial piezoelectric layer of BTO ($BaTiO_3$) is combined with a polycrystalline magnetostrictive layer of FeGa ($Fe_{0.7}Ga_{0.3}$) in bilayer phase connectivity. The investigated composite structure is depicted in **Figure 2-26**, shown schematically in (a) and experimentally in (b) [59]. The FeGa film is patterned into two conducting electrodes, which are used to directly apply electric fields to the BTO layer. As mentioned earlier, substrate clamping must be addressed in order to realize strong magnetoelectric coupling. To ensure full elastic response in the BTO layer, it is released from the underlying $SrTiO_3$ substrate using focused ion-beam milling. In this manner, an applied electric field generates piezoelectric strain in the BTO layer near the gap region, which in turn transfers the elastic strain to the FeGa film in released region.
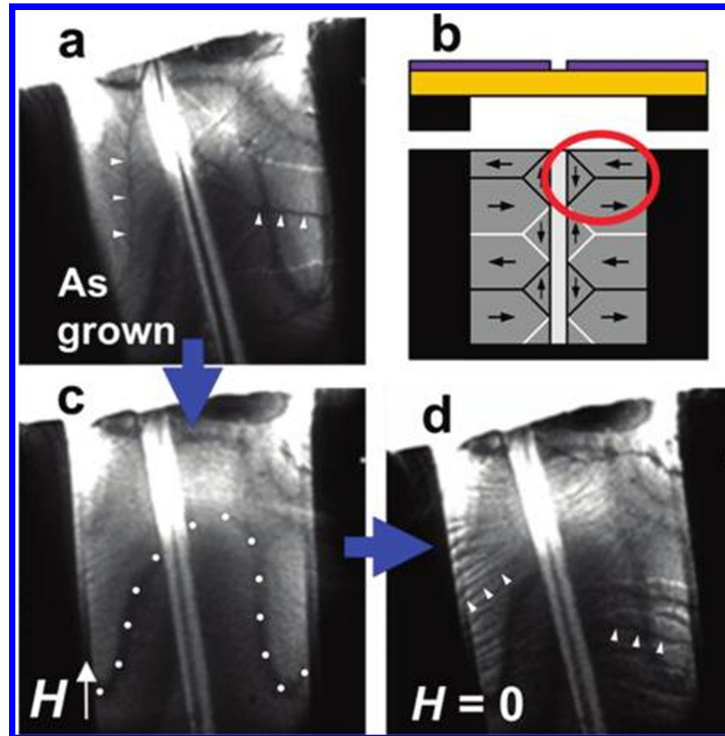
**Figure 2-27. Magnetic response of thin film bilayer device. (a),(c) and (d) represent Lorentz micrographs of the device with magnetic fields applied. Blue arrows indicate the order of operations. (b) A schematic of the device in side-view (top) and plane-view (bottom). A schematic of the resulting magnetic order is depicted in the plane-view as light and dark lines representing domain walls, and arrows representing magnetization. Taken from [59].**

Here, Lorentz-force transmission electron microscopy (LTEM)– a high spatial resolution imaging technique– is employed to characterize local in-plane magnetization with *sub-100 nm* resolution, the scale at which device implementation is envisioned. The magnetic nature of the bilayer is structure characterized with LTEM through the application of external magnetic fields. **Figure 2-27** shows plane-view LTEM images of the bilayer device during sequential application of magnetic field [59]. This contrast is a result of the interaction of the transmitted electron beam with the in-plane magnetization of the FeGa thin film. This technique will be thoroughly reviewed in a later section. The resulting contrast is in the form of sharp light or dark lines, which depict the walls

59

between ferromagnetic domains with different local magnetization directions. In addition to contrast lines of magnetic order, diffuse lines of dark contrast are also seen. These are known as Bragg-diffraction bend contours, and are not magnetic in origin. In **Figure 2-27** (c) and (d), it is demonstrated that application and subsequent removal of a magnetic field establishes local ferromagnetic order (depicted in frame (b)) that is different from its as-grown state seen in **Figure 2-27 (a)**. This establishes both the magnetic character of FeGa and the utility of LTEM as a probe of local magnetization.

Changes in the local magnetization solely using electric fields were demonstrated next. **Figure 2-28** shows the reversible control of magnetic domains induced by electric fields. Frames (a)–(d) represent experimental confirmation of magnetoelectric coupling in the device, and frames (e)–(g) are simulations of the device behavior. During electric field sweeps *(±10 MV/m* in *0.2-0.5 MV/m* steps) discrete magnetization switching events will occur. Frames (b) and (c) are before and after images of the induced magnetic domain wall motion– this motion is confirmed in frame (d), which is the difference of images (b) and (c). Magnetostrictive anisotropy changes induced by the transferred strain induces motion in 90° domain walls as vertically oriented magnetic domains rotate to horizontal orientations.
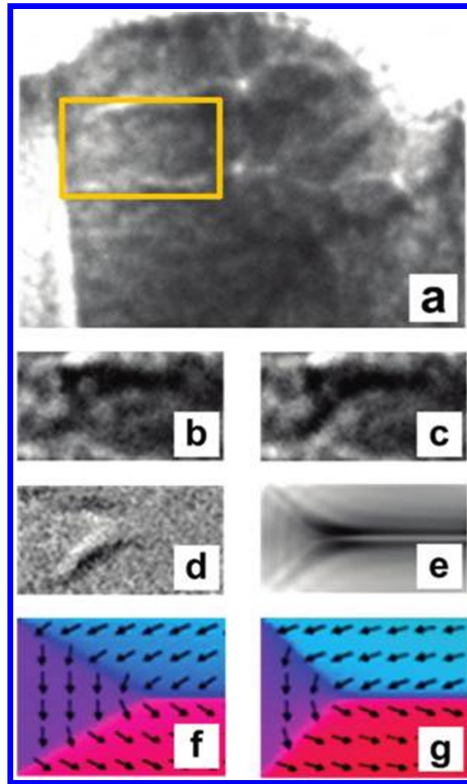
**Figure 2-28. Reversible control of magnetic domain using static electric field. (a) LTEM image of FeGa film with the magnetoelectrically active region framed in the yellow box. (b) and (c) LTEM image of low electric field state and high electric field state, respectively. (d) Difference image obtained from subtracting (c) from (b), proving motion of domain wall. (e) Simulation of (d) using contrast transfer function. (f) and (g) Local magnetic moments in object-oriented micromagnetic framework (OOMMF) simulation. Taken from** [59]**.**

**Figure 2-28** (e) is a simulation of the experimental difference image in frame (d).

Here, contrast is produced according to the local magnetic moments for two different

domain wall configurations that are represented in frames (f) and (g). Using the object-

oriented micromagnetic framework (OOMMF) and measured material parameters for

FeGa, a uniaxial inverse-magnetostriction anisotropy change of *25 kPa* was calculated in

order to recreate the contrast difference observed experimentally. Thus, electrically

induced nanomagnetic switching can be described by a variation in the uniaxial magnetic

anisotropy.

61
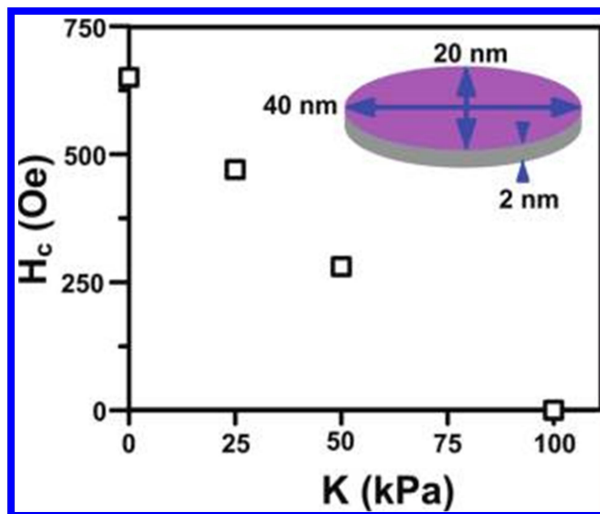
**Figure 2-29. Demonstration of magnetoelectric memory mechanism derived using OOMMF. Inset depicts an individual ellipsoid of magnetostrictive material** [59]**.**

**Figure 2-29** describes a proposed technological implementation of the electrically

tunable uniaxial anisotropy. As reviewed earlier, both demonstrated and proposed

MRAM technologies make us of either current-generated magnetic fields or spin-transfer

torque effects, which require relatively large current densities for writing or erasing

magnetic elements. Here, an MRAM mechanism is proposed that reduces the current

density, and thus power density required for switching; application of a static electric

field to reduce the anisotropy barrier for switching an individual magnetic element. The

demonstrated magnetostrictive switching mechanism cannot by itself produce switching

between the conventional parallel and antiparallel magnetic states used in MRAM

devices as binary logic states. However, magnetostriction can be used to reduce

anisotropy of a selected MRAM element, reducing the current needed to switch the

element. **Figure 2-29** plots the coercive field $H_c$ with uniaxial anisotropy $K$ for a *20 x 40*

*x 2 nm³* ellipsoid of FeGa thin film, determined using OOMMF. With application of an electric field to control magnetic anisotropy, which in turn controls the coercive field, it is possible to realize that the nanomagnetic ellipsoid can be changed from a hard magnet to a soft magnet through varying the voltage. In this manner, it is also possible to influence the global behaviors of a large array of nodes; a universally applied voltage to collective coercive fields reduced to near zero can allow for simultaneous reset through applied magnetic and electric fields. Thus, strain-mediated magnetoelectric coupling provides a mechanism for switching hard and soft magnets– a solution to the contradictory needs of MRAMs, which simultaneously require large coercive fields for stability and small coercive fields for energy-efficient switching.

# Chapter 3: Experimental Approach

## *3.1 Introduction*

Thus far, strain mediation of magnetic properties in magnetostrictive media has been observed in the aforementioned example of a bilayer FeGa/BTO magnetoelectric device. It is noted that magnetoelectric responses were witnessed in regions of 90º domains walls, and thus control of the effect is dictated by magnetic hysteresis. The following work details efforts toward controlling the strain mediation through direct mechanical interaction with the magnetostrictive phase of the system.

Here, an introduction to the experimental details, materials, and methods are presented. In situ methods for directly correlating external action and system response are once again employed with the use Lorentz TEM magnetic imaging techniques while a freestanding FeGa thin film is mechanically deflected with a nano-manipulation holder. The holder consists of an STM tip, which is used to deflect the thin film and generate internal strains within the system. Point-load deflection presents a simple mechanical interaction mechanism, and thus is the best option for probing its direct effects on the local magnetic order. Fabrication methods for continuous and patterned FeGa thin films are reviewed, and the effectiveness of magnetic imaging with these systems is demonstrated.

## 3.2 Magnetostriction in FeGa

We have previously reviewed how magnetocrystalline anisotropy competes with exchange energy to set the width of domain walls. The origin of crystal anisotropy is due mainly to spin-orbit coupling; the orbits of electrons are strongly coupled to the lattice, as the orbital magnetic moments are almost entirely quenched. The crystal anisotropy is essentially the orientation of the magnetization with respect to the crystal lattice axes. This can be expressed in terms of a series expansion of the direction cosines of magnetization relative to the crystal axes [23], [24], [27]. In a hexagonal crystal this energy depends on only the angle $\theta$ between the magnetization vector and the c-axis of the crystal. This energy can be simply represented as, $E = K_1 sin^2\theta$ [23], [27]. Dimensionality also influences the material magnetic properties, and thus contributes to the overall energy. In general, magnetic materials– even polycrystalline structures lacking magnetocrystalline anisotropy– tend to magnetize along the long axis of the specimen versus the short axis. This tendency reflects the shape anisotropy, and is quantized by the demagnetizing field $H_d$ of the specimen as [27]:

$$E_{ms} = -\tfrac{1}{2}\vec{H}_d \cdot \vec{M} \quad \textbf{(Equation 3-1)}$$

There is another source of anisotropy that contributes to the overall magnetization energy. In general when a substance is exposed to a magnetic field, its dimensions change. This effect is known as magnetostriction. Physicist James Joule first described this effect in 1842 when he observed that an iron rod increased in length when

magnetized lengthwise by a weak field [27], [60]. This fractional change in length $l$ is simply an induced strain $\lambda$, and is quantized as:

$$\lambda = \frac{\Delta l}{l}$$ **(Equation 3-2)**

The value of $\lambda$ is conventionally measured at magnetic saturation; an idealized process for achieving magnetostrictive response at magnetic saturation is represented in **Figure 3-1** [60]. The change in length is the result of the rotation of small magnetic domains. This rotation and reorientation thus cause internal strains to develop within the specimen. The strains lead to stretching (in the case of positive magnetostriction) of the material in the direction of the magnetic field. Through this stretching process, the cross section of the specimen is typically reduced in such a way as to keep the volume constant. The size of the volume change is relatively small, and is generally neglected under normal operating conditions. With the application of stronger fields, stronger and more definite reorientation of more domains in the direction of the magnetic field develope. Saturation is achieved when all the magnetic domains have become aligned with the magnetic field [27], [34], [60].
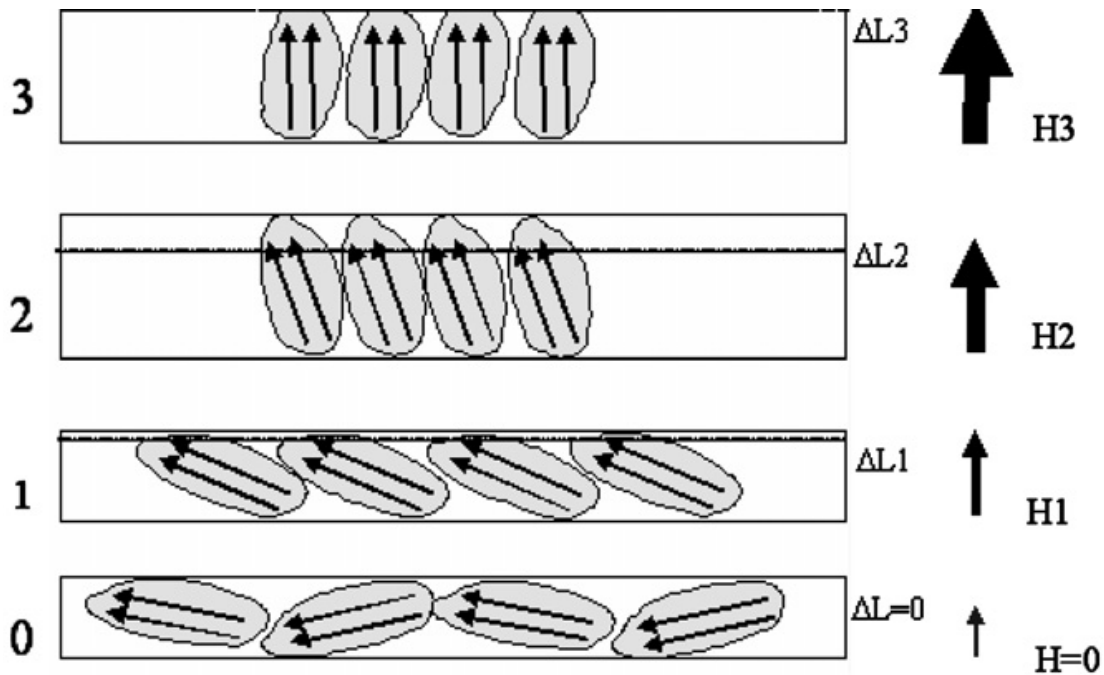
**Figure 3-1. Schematic of magnetostriction of a crystal. Taken from** [60]**.**

Magnetostriction is due mainly to spin-orbit coupling, which is also responsible for crystal anisotropy. This relationship is represented, very basically, in **Figure 3-2** [27]. The black dots represent atomic nuclei, the arrows show the net magnetic moment per atom, and the oval lines enclose the electrons belonging to, and distributed nonspherically about each nucleus. The uppermost row of atoms depicts the paramagnetic state above the Curie temperature $T_c$. With the onset of spontaneous magnetization at temperatures below $T_c$, the spins and the electron clouds rotate into a particular orientation determined by the crystal anisotropy. The nuclei are forced further apart, and the spontaneous magnetostriction is therefore $\Delta L'/L'$. If a strong field is applied vertically, the spins and the electron clouds would rotate 90°, and the domain of which these atoms compose would magnetostrictively strain by an amount $\Delta L/L$ [27].
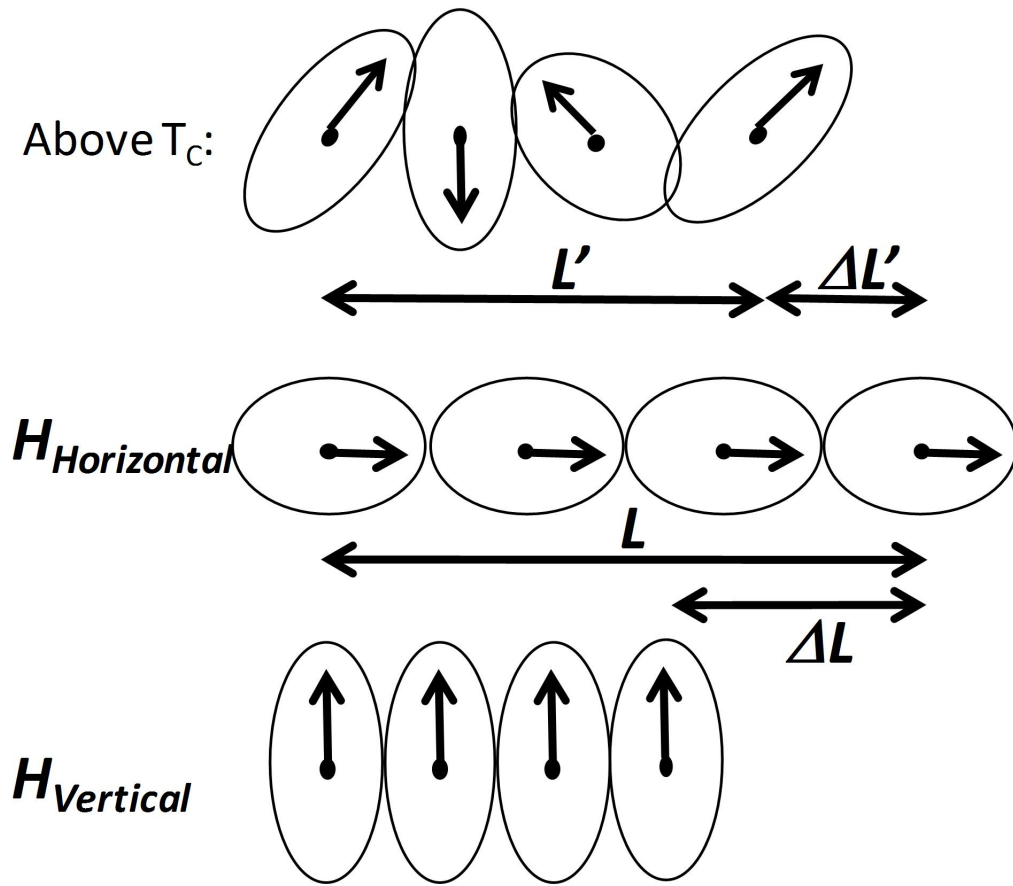
**Figure 3-2. Mechanism of magnetostriction. Adapted from** [27]**.**

Magnetostriction occurs in all magnetic substances. However, even in strongly magnetic substances the effect is usually small (typically on the order of $10^{-5}$ or $\sim 1\ MPa$). Despite this fact, the existence of magnetostriction means that an applied mechanical stress can alter the domain structure and create a new source of magnetic anisotropy. These changes can have a substantial effect on the low-field magnetic properties, such as permeability and remanence (for a material with positive magnetostriction, tensile stress increases the permeability) [27]. This effect of stress on the magnetization properties of a material is thus referred to as the inverse magnetostrictive effect.

The amount of magnetostrictive strain exhibited by a crystal in a particular direction depends on the direction of the magnetization. In the absence of stress the direction of $M_s$ is controlled by crystal anisotropy, as characterized by the first anisotropy constant $K_1$. When a stress is acting, the direction of $M_s$ is controlled by both applied stress $\sigma$ and $K_1$. Thus, these two quantities are involved in the expression for the part of the energy that depends on the direction of $M_s$, and is defined for a cubic crystal as [27]:

$$E = K_1(\alpha_1^2\alpha_2^2 + \alpha_2^2\alpha_3^2 + \alpha_3^2\alpha_1^2) - \tfrac{3}{2}\lambda_{100}\sigma(\alpha_1^2\gamma_1^2 + \alpha_2^2\gamma_2^2 + \alpha_3^2\gamma_3^2) - 3\lambda_{111}\sigma(\alpha_1\alpha_2\gamma_1\gamma_2 + \alpha_2\alpha_3\gamma_2\gamma_3 + \alpha_3\alpha_1\gamma_3\gamma_1)$$

(**Equation 3-3**)

where $\alpha_1$, $\alpha_2$, $\alpha_3$, are the direction cosines of $M_s$, and $\gamma_1$, $\gamma_2$, $\gamma_3$ are the direction cosines of the stress $\sigma$. The first term is the crystal anisotropy energy. The next two terms comprise what is generally known as the magnetoelastic energy $E_{me}$, which involves the magnetostrictive strains and the stress. The equilibrium direction of $M_s$ is that which minimizes the energy. Generally, this direction will be determined largely by crystal

anisotropy when $K_1$ is much larger than $\lambda_{100}\,\sigma$ and $\lambda_{111}\,\sigma$; the stress will control in $M_s$

direction when this condition is reversed. When the magnetostriction is isotropic, the

above equation for magnetoelastic energy reduces to the simple form:

$$E_{me} = \tfrac{3}{2}\lambda\sigma\sin^2\theta = K_\sigma\sin^2\theta \quad \textbf{(Equation 3-4)}$$
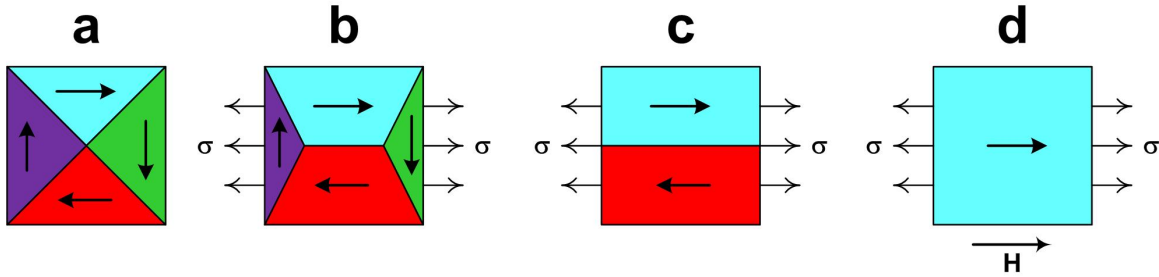


**Figure 3-3. Schematic of magnetization of a material with positive magnetostriction under tensile stress. Adapted from [27].**

If crystal anisotropy is weak, the direction of $M_s$ in the absence of a field will be

controlled largely by the stress. **Figure 3-3** represents the magnetization process of a

small portion of a specimen through inverse magnetostriction [27]. The application of a

small tensile stress to the demagnetized specimen will cause domain walls to move in

such a way as to decrease the volume of domains magnetized at right angles to the stress

axis, resulting in domains having a higher magnetoelastic energy. These domains are

completely eliminated by a higher value of the stress, bringing $E_{me}$ to a minimum. The

domain structure now resembles a uniaxial crystal, and a small applied field is required to

saturate the specimen. **Table 3-1** summarizes the three major contributions to anisotropy

covered in this work [27].

| Kind of Anisotropy | Energy Responsible | Governing Relation $E=K_u\sin^2\theta$ |
|:---:|:---:|:---:|
| Crystal | Crystal Anisotropy | $K_u=K_1$ |
| Shape | Magnetostatic | $K_u=K_s=\frac{1}{2}(N_a-N_c)M^2$ |
| Stress | Magnetoelastic | $K_u=K_\sigma=\frac{3}{2}\lambda\sigma$ |

**Table 3-1. Summary of some uniaxial anisotropies. Adapted from** [27]**.**

Although Joule first reported observing magnetostriction in the early 1840s, magnetostrictive materials did not find device applications (as actuators and sensors) until a much later time. In the 1960s, it was observed that rare-earth metals, such as terbium and dysprosium, exhibited large magnetostriction *(~10,000 ppm*) [61]. Rare-earth metals are generally ferromagnetic at temperatures well below room temperature, but they do not demonstrate significant magnetostriction at room temperature.

In an effort to solve this dilemma, rare-earth metals are alloyed with transition metals (Fe, Ni, Co) that have Curie temperatures above room temperature [27], [61]. These compounds produce large magnetostriction– *2630 ppm* and *650 ppm*, respectively for $TbFe_2$ and $DyFe_2$. Generally magnetostriction and crystal anisotropy display some correlation, as both have physical origins in spin-orbit coupling. Therefore, these abnormally large values of magnetostriction also correspond to large magnetocrystalline anisotropies, requiring large magnetic fields to drive them to saturation [61].

The magnetocrystalline anisotropy can be reduced significantly with attention towards the proportions of Tb and Dy, which lead to the development of commercially known terfenol-D ($Tb_{0.27}Dy_{0.73}Fe_{1.95}$) by researchers at the Naval Ordinance Laboratory [61].  Terfenol-D displays large magnetostriction *(~2000 ppm*) at room temperature and

71

has considerably lower crystal anisotropy when compared to either $TbFe_2$ or $DyFe_2$. However terfenol-D is a brittle material, which has severely limited its applications in smart materials systems where exposure to high shock or tensile strains is probable.

Iron-gallium (galfenol) alloys over the past few years have been gaining increasing interest since their development by Clark et al. at the Naval Surface Warfare Center [62] [60], [61], [63]–[66]. Galfenol alloys offer a combination of moderate magnetostriction (~*350 ppm*) under very low fields (~*100 Oe*) and have very low hysteresis, while exhibiting high tensile strength (~*500 MPa*) and weak temperature dependence [60], [61], [63]–[66]. FeGa is also highly ductile and can easily be grown epitaxially on on a silicon substrate, making it an ideal magnetostrictive material for micro and nano-scale devices. These properties suggest that FeGa can be easily integrated into design spaces where mechanical robustness and magnetic performance are a simultaneous requirement.
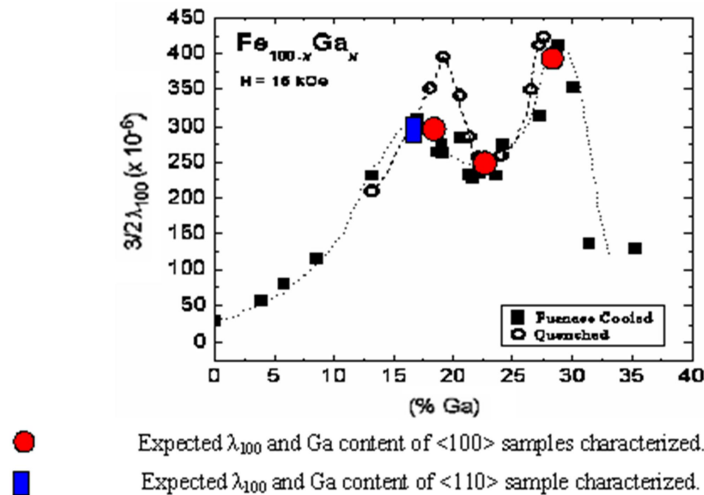


**Figure 3-4. Magnetostriction of FeGa versus Ga content. Taken from** [61]**.**

FeGa materials systems are challenging to characterize, as multiple factors affect their magnetostrictive properties. Clark et al. have shown that magnetostriction varies significantly with Ga content– this trend is shown in **Figure 3-4** – thus, it can be expected that the magnetomechanical behavior is also composition dependent [62], [61]. Magnetostriction is generally measured, and results presented, as strain vs field, and/or magnetic induction vs field curves. The $\lambda$–$H$ and $B$–$H$ curves of <100>-oriented single-crystal for a sample with FeGa 29 at. % Ga content are presented in **Figure 3-5** [61]. Generally, trends for all Ga content ranges (not presented) show that saturation magnetostriction reaches a maximum under compressive stresses of *15–30 MPa*.

This trend is clearly present in the strain vs field curve for 29 at % Ga presented in **Figure 3.5** This compressive stress aligns magnetic moments perpendicularly to compressive stress, yielding the largest magnetostriction possible. However, larger than optimum compressive stresses can lead to a decline in magnetostriction, as is seen in the curve, and explanations for this trend are inconclusive [61]. The $B$–$H$ curve for the respective compressive stresses are each smooth, and absent of any transition regions in term of magnetic character. These results reflect the complexity of achieving large magnetostriction where careful consideration must be given to material fabrication parameters, such as Ga content and stress annealing [60], [61], [65], [67]–[70].
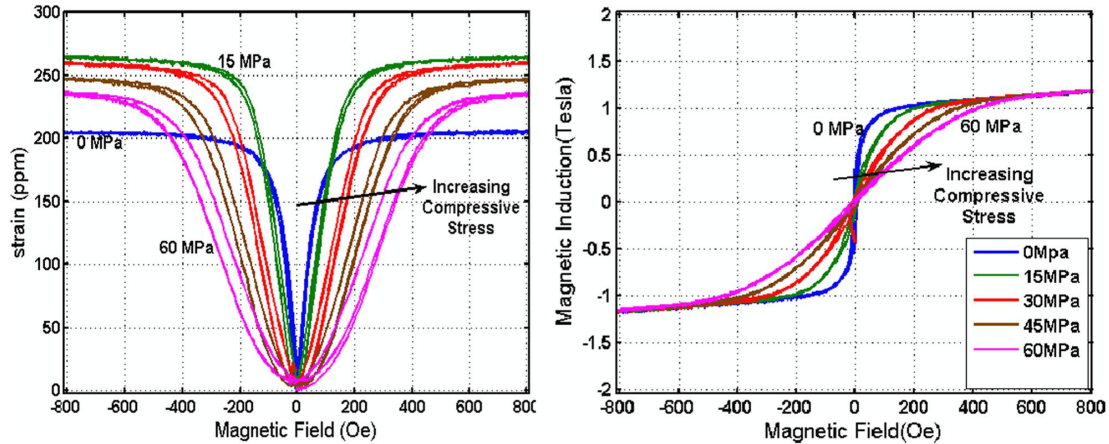
**Figure 3-5. λ–H (left) and B–H (right) of furnace cooled 29 at % <100>-single crystal FeGa with compressive pre-stress: 0, 15, 30, 45, 60, and 80 MPa. Taken from** [61]**.**

Thus far, the characteristics of single-crystalline FeGa have been discussed. Single crystals provide an ideal starting point for characterizing and modeling FeGa behavior. However, polycrystalline forms of the compound are more likely to be used in a commercial setting. The magnetostriction of a polycrystalline system thus depends on grain orientation variations and grain-to-grain interactions with applied magnetic field. Significant work has gone towards developing an effective model to understand and predict polycrystalline magnetomechanical behavior [61], [71].
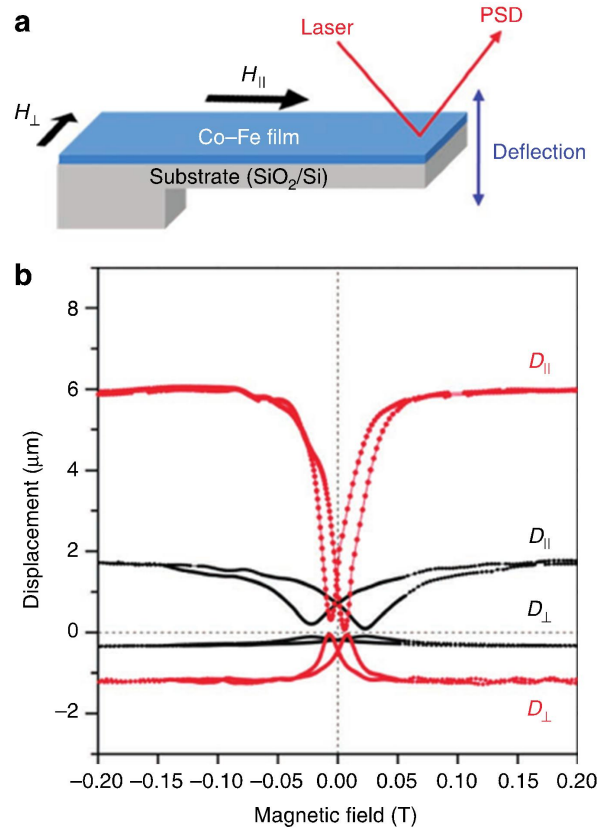
**Figure 3-6. (a) Schematic showing cantilever deflection method for measuring λ. (b) Plot of displacement versus magnetic field for as deposited (black curve) and annealed (red curve) CoFe. This represents an example of how the figure of merit is determined for the $Fe_{0.7}Ga_{0.30}$ film. Taken from [72].**

Given the complications associated in predicting the magnetomechanical behavior of polycrystalline FeGa thin films, it is thus sufficient to accurately measure the magnetostrictive response of the system under investigation for the purpose of this study. Best measurements are achieved through measuring cantilever deflections with the application of parallel and perpendicularly aligned magnetic fields. This technique is schematically depicted in **Figure 3-6** in an example of a *Co–Fe* film, and is a successful method for high-throughput characterization [66], [72], [73]. Here, the material is deposited onto a cantilever array substrate, and the deflection of a laser reflected off of a cantilever is monitored as a function of applied magnetic field. The reflected light is

collected with a position sensitive detector (PSD) and converted to an effective

magnetostrictive constant $\lambda_{eff}$ in accordance with the model placed by du Tremolet de

Lachiesserie and Peuzin [66]:

$$\lambda_{eff} = \frac{2(D_{//} - D_{\perp})E_s t_s^2 (1 + v_f)}{9E_f L^2 t_f (1 + v_s)} \quad \textbf{(Equation 3-5)}$$

where $L$ is cantilever length, $E_f$ and $E_s$ are Young's moduli of the film and substrate,

respectively, $t_f$ and $t_s$ are their respective thicknesses, and $v_f$ and $v_s$ are their respective

Poisson ratios. $D_{//}$ and $D_{\perp}$ represent the measured displacement of the tip of the cantilever

out of the plane of the cantilever, parallel and perpendicular to its long axis, respectively.

This technique was previously employed in measuring the figure of merit in

polycrystalline $Fe_{0.7}Ga_{0.3}$ thin films with film thickness of *30 nm*, for the investigation of

the previously reviewed FeGa/BTO bilayer heterostructure. Saturation magnetostriction

$\lambda_s$ was determined to be *~100 ppm*, which is a reasonable value for a polycrystalline film.

In this present study, the same composition of FeGa was used, and film thicknesses up *30

nm* were investigated. Therefore, this previous determination of the figure of merit will

suffice for the purpose of this study.
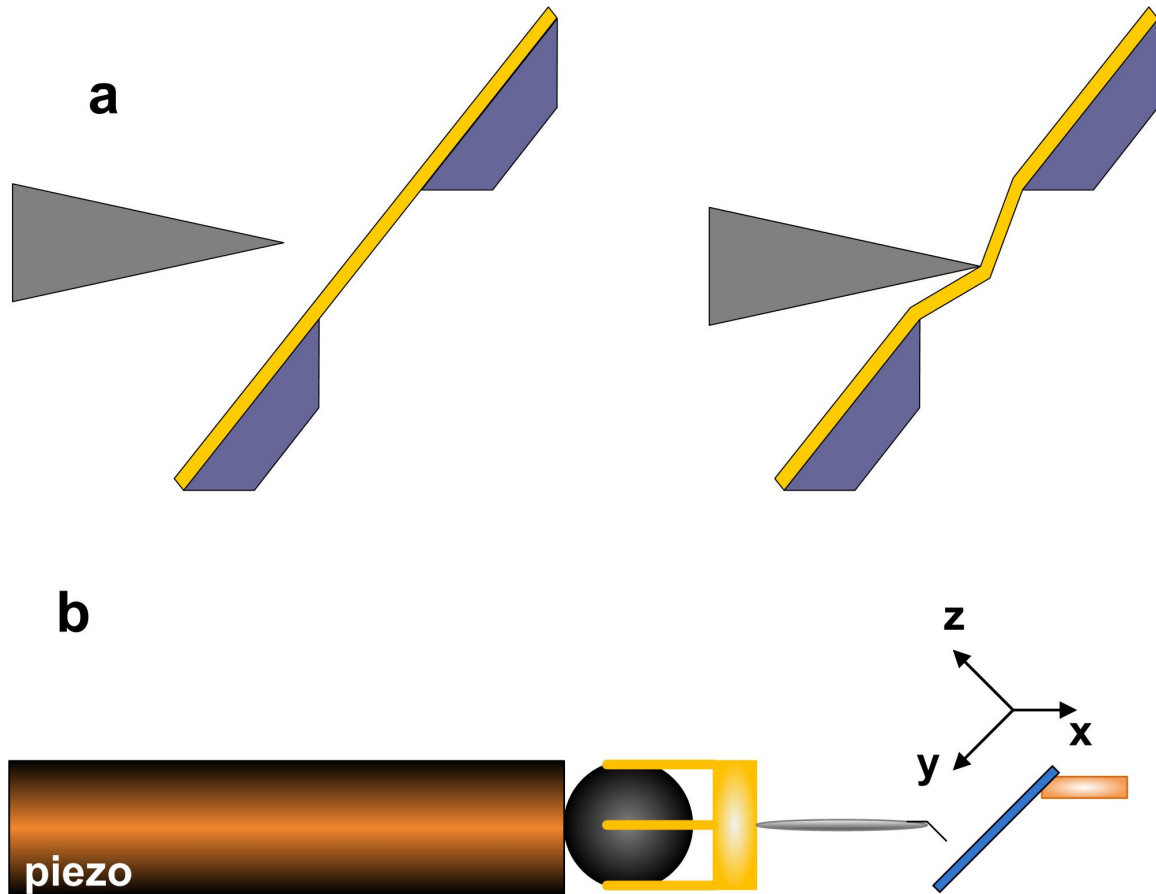
**Figure 3-7. (a) Schematic of mechanism for direct mechanical interaction with FeGa thin film. (b) Schematic of NanoFactory™ TEM-STM holder for in situ manipulation and observation.**

Direct mechanical interaction with magnetostrictive FeGa thin films could help identify an improved means of controlling local magnetization in magnetoelectric heterostructures. For the purpose of this investigation, FeGa thin films– supported by flexible, freestanding $SiN_3$ membranes– are directly strained through external mechanical interaction with a scanning probe, as is illustrated in **Figure 3-7**. Changes in the magnetic order of FeGa thin film are observed in situ with use of Lorentz- force TEM, a powerful

magnetic contrast imaging technique. In this manner, the film experiences hysteresis with changes in external magnetic field (sourced from the objective lens in the column) and applied stress (sourced from point-load deflections of the film with a scanning probe). Post analysis of the magnetic contrast obtained by this technique will give insight toward the impact of the two competing anisotropies on the local magnetic structure.

The use of an in situ technique for experimentation is imperative in order to directly associate magnetostrictive responses to mechanical interaction– the dynamics of the system can be observed in real time. Transmission electron microscopy (TEM) is one of the more powerful tools for characterizing materials and events at the nanoscale given its improvements in both spatial and temporal resolution.

Nevertheless, there are special challenges in using TEM that can limit sample viewing and interaction [74]. The TEM specimen holder is a compact tool, and typical TEMs allow a *2 mm* gap for the specimen in between the two pole pieces of the objective lens. This gap has such spatial limitations in order to maintain the achievable image resolution. Thus, there is limited space available within a conventional TEM for manipulating a specimen. In addition, the depth of focus is also limited, which further restricts the amount of manipulation and movement of a specimen within the pole-piece gap. Finally, conventional TEM specimen holders are built solely for the purposes of specimen imaging. The holders themselves are not equipped for interacting with the sample through external stimuli (i.e. electrical, thermal, mechanical, etc). Thus a specialized in situ specimen holder is required in order for the specimen to experience direct mechanical interaction with magnetic contrast imaging.

A specialized TEM holder built by NanoFactory Instruments™ has the capability of imaging while simultaneously interacting with the specimen. This tool is schematically depicted in **Figure 3-7 (b),** and is shown to scale in **Figure 3-8**. It consists of a compact piezoactuated scanning tunneling microscopy (STM) probe, and is capable of coarse and fine motion in three spatial ranges. Physical contact of the STM tip with freestanding thin film allows for the mechanical interactions necessary to probe magnetoelastic response.
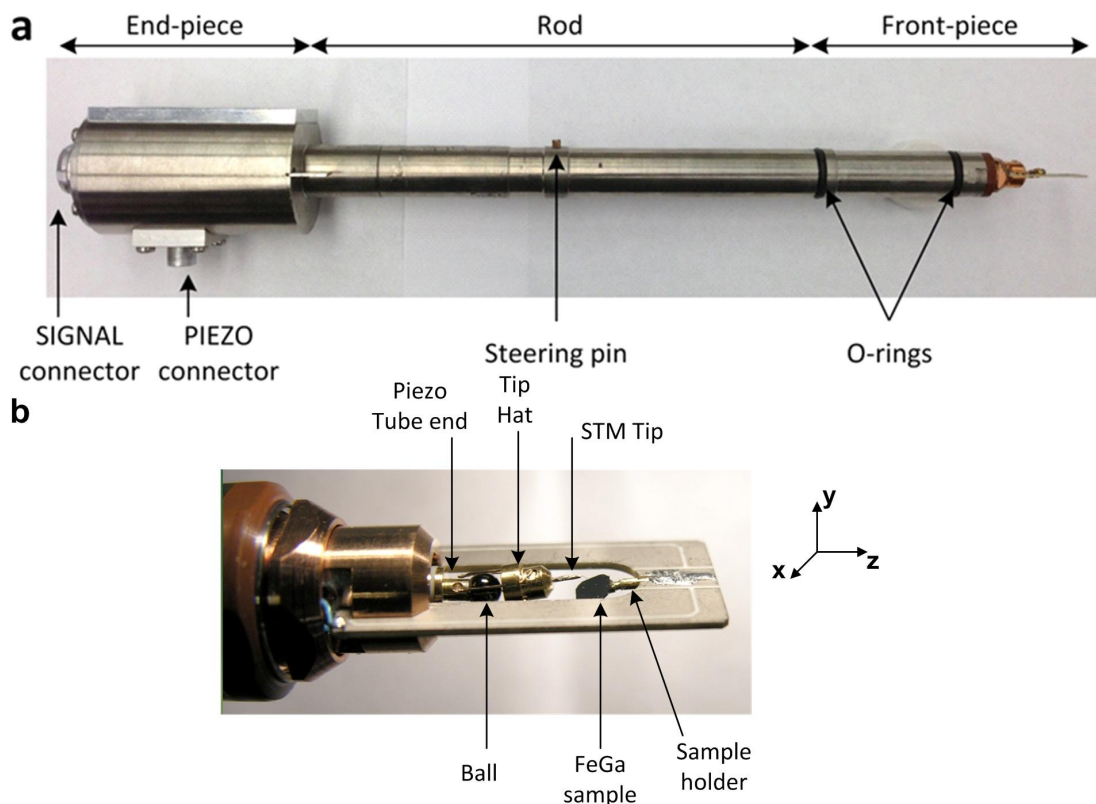


Figure 3-8. (a) NanoFactory™ TEM-STM holder. (b) Close of up front-piece constituents. The only moving part is the tip hat. The STM tip is maneuvered to the film through short pulses of the piezoelectric rod.

**Figure 3.8 (a)** shows the NanoFactory™ holder designed to fit in the JEOL JEM-2100 goniometer. The holder consists of three main parts: end-piece (including

connectors), the rod, and the front-piece. The SIGNAL connector provides signals for excitation and measurements. The PIEZO connector controls signals in the piezoelectric tube. The front-piece contains the three-dimensional positioner system that is fitted to the piezoelectric tube, a closer view is provided in **Figure 3-8 (b)**. As pointed out in the image, the end of the piezoelectric tube has a sapphire ball functionalized with conductive coatings. The six-legged "tip hat" sits directly upon the sapphire ball, anchoring the STM tip. The tip hat is the only moving part of the holder, and is moved by short pulses of the piezoelectric rod. A STM wire ($Pt_{0.8}Ir_{0.2}$, *0.25 mm* diameter, Agilent Technologies) is attached to tip hit, and is fastened with two small screws. Due to its size, the STM wire is a secondary component of the mechanical interaction with the film, serving mainly as a vehicle for probe motion. Attached to the STM wire is a beryllium-copper wire (*25 μm* diameter) that serves as the primary interaction probe for the experiment.

A three-dimensional inertial slider mechanism drives the coarse motion of the tip-hat/STM system. Short high-voltage pulses from the NanoFactory™ controller to the piezotube induce rapid motion of the sapphire bearing. The tip-hat slides against the surface of the ball in response. Hence a "step" is taken in one of the three directions, depending on the direction of the piezo movement. For coarse motion all three directional axes have a motion range of *2 mm*. Measured step sizes for coarse motion varied from *~0.5-30 μm*. Given the unpredictability of the sliding mechanism for coarse motion, the controller was modified to include fine motion control, where the voltage-displacement dependence is more linear and reproducible. The motion range for fine control is limited to *~10 μm*. However, this motion is the best option for interacting with the fragile thin

film system. Coarse motion control is mainly employed to taxi the tip to, or about the film surface. The relative distance between the tip and the film surface is determined by moving the sample to eucentric height, and using the image wobble or stage wobble to track the tip as it is brought toward the film. During a typical study, the film is deflected ~*10 μm* at the center.

The FeGa film is fixed at the opposing end of the front-piece stage with a brass socket system. Brass holding-pins are micro-machined to sit stationary in the socket fixed at the end of the blade. The head of the holding-pin is filed to a 25° incline, and the sample is then permanently fixed to the head using a CircuitWorks® conductive two-part epoxy. The inclined sample arrangement allows the tip to interact with the film orthogonally, and also allows for the sample to experience external magnetic fields in situ, applied by the objective lens, without tilting or rotating the sample stage.

### *3.3.1 Lorentz Transmission Electron Microscopy*

Transmission electron microscopy (TEM) is a powerful and versatile tool allowing for understanding and development of material properties at the atomic scale. Knoll and Ruska first demonstrated the use of electrons for imaging in 1932– made possible by their development of electron lens.  From the perspective of materials science, an important development came in the 1940s with the first thinning of metal foils to electron transparency [74]. Continued advancements in techniques and components have made TEM an integral part of the materials characterization process.

The major attraction to TEM is due mainly to its enhanced resolution when compared to visible-light microscopes. Resolution is defined as the smallest distance between two points that can be resolved in an image. Macroscopic properties of materials

are largely determined by properties at the atomic scale– therefore, smaller imaging

resolutions yield better insight toward atomic scale properties. Resolution is determined

by wavelength $\lambda$ of the source, and is defined by classical Rayleigh criterion [74]:

$$\delta = 0.61 \times \lambda \quad \textbf{(Equation 3-6)}$$

Thus, smaller source wavelengths yield higher resolving power. Louis de Broglie

first theorized that the electron has wavelike characteristics, and that their wavelength is

related to their energy. Independently, Davisson and Germer and Thompson and Reid

later confirmed the theory with electron diffraction experiments, which led to their

implementation as a source in a microscope. Modern TEMs typically operate within a

range of *100–400 kV* electron-accelerating voltages. The relationship between $\lambda$ and the

accelerating voltage of the electron microscope *V* is given by [74]:

$$\lambda = \frac{h}{\sqrt{2m_0 eV}} \quad \textbf{(Equation 3-7)}$$

where *h* is Planck's constant, and *e* and $m_0$ are charge and mass of electron, respectively.

Thus, increasing the accelerating voltage consequently decreases the wavelength. TEMs

are typically operated at *200 kV*, which corresponds to *0.02508 Å* wavelength (*~100*

times smaller than typical atom distances in a solid). However, it is important to note that

modern TEMs cannot resolve at the wavelength limit as the performance of electron lens

greatly impacts the resolution as well. The resolution of modern TEMs is around *1-2 Å*.
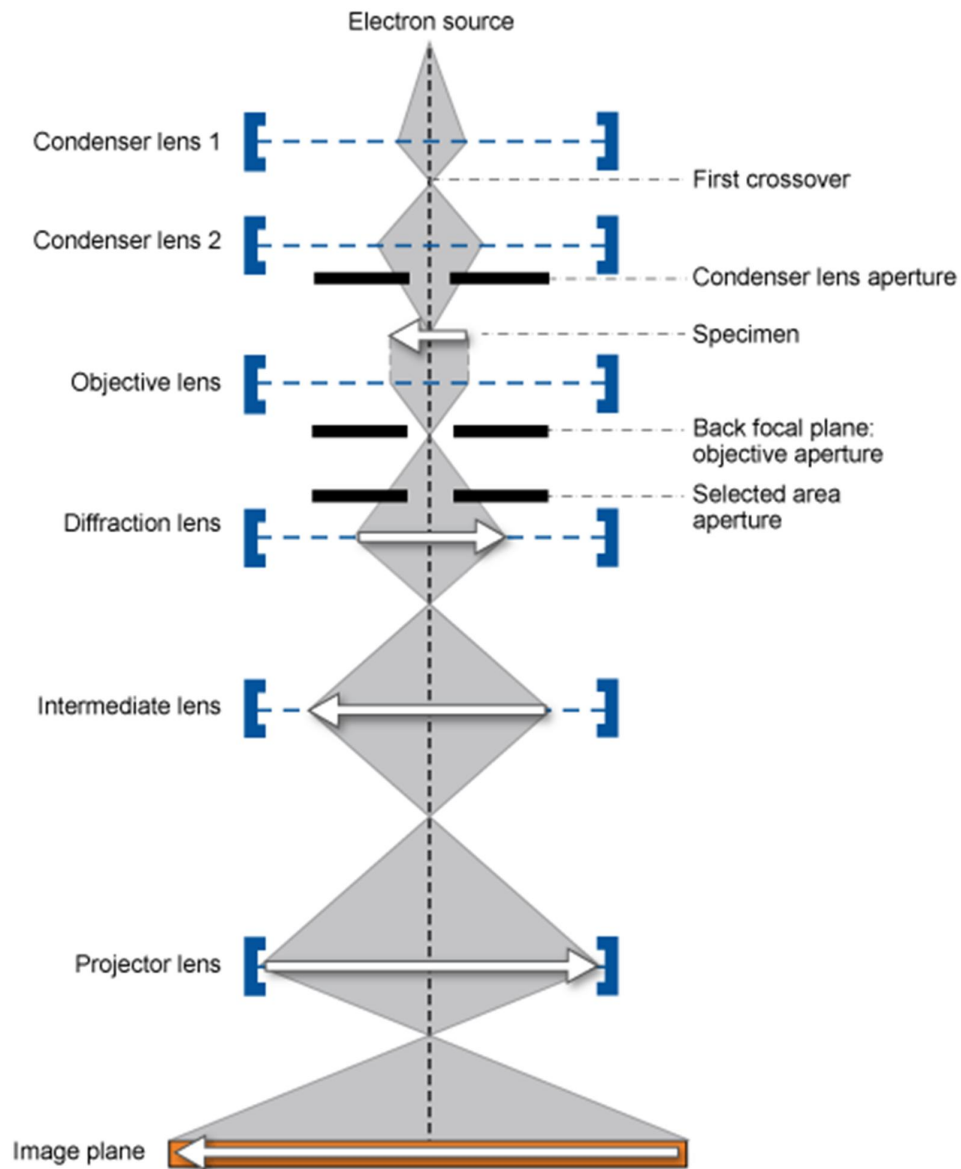
**Figure 3-9. Schematic of electron-optical system for TEM. Adapted from** [74]**.**

The TEM consists of five major components: electron gun, condenser-lens system, specimen stage, objective-lens system and imaging system. These components are schematically represented in **Figure 3-9** [74]. The electron gun consists of an electron source (thermionic or field emission cathodes), Wehnelt cylinder, and an anode to generate an electron beam. The components for a thermionic electron gun are

schematically depicted in **Figure 3-10** [74]. To achieve emission, a filament current

resistively increases the temperature of a $LaB_6$ cathode until emission occurs. Electrons

leaving the cathode accelerate through the potential difference relative to the anode,

acquiring greater energy and velocity. A small negative bias on the Wehnelt cylinder

converge the electrons to crossover prior to the anode, narrowing the beam for passage

through the anode opening and into the illumination system.
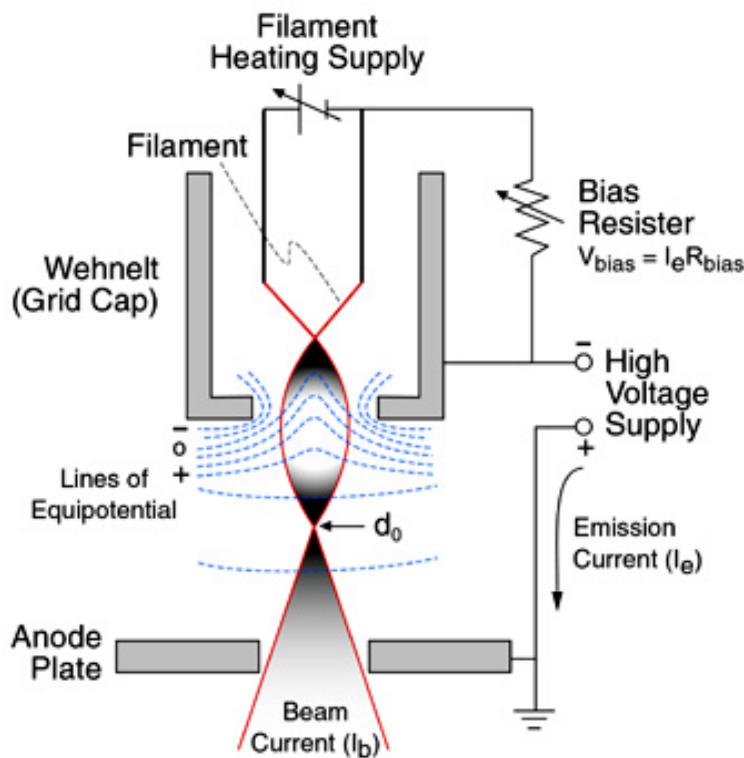


**Figure 3-10. Schematic of a thermionic electron gun. Taken from** [74]**.**

Electron-beam optics are moderated with electromagnetic lenses. A magnetic

electron lens consists of a cylindrically symmetrical core of soft magnetic material with a

gap– known as the polepiece, depicted in **Figure 3-11** [74]. A coil of copper wire

surrounds each polepiece– in passing current through the wire, a magnetic field is created

in the bore space (represented as red lines). The strength of the field in a magnetic lens

controls the ray paths; the depicted electron path through the lens is an analogous

approximation to that of a conventional optical system.
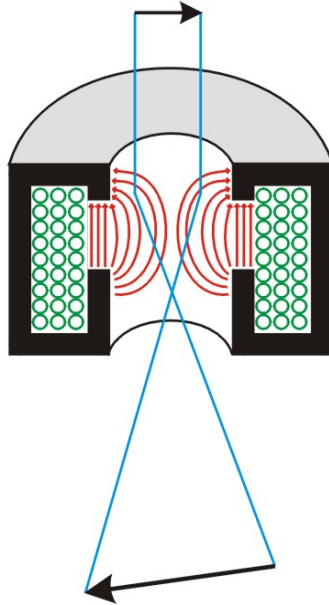


**Figure 3-11. Electromagnetic lens consisting of polepiece and copper wire coils. Adapted from** [74]**.**

When an electron with charge $q$ (equal to $-e$) enters a magnetic field of strength

$\vec{B}$, and an electric field of strength $\vec{E}$, it experiences a force $\vec{F}$ known as the Lorentz

force, which depends on the velocity of the electron, $\vec{v}$ [74]:

$$\vec{F} = -e(\vec{E} + \vec{v} \times \vec{B})$$ **(Equation 3-8)**

Thus, the electron spirals through the lens field with a helical trajectory. This

effect is observed during operation as the image rotates through changes in focus or

magnification, and is depicted in the ray diagram of **Figure 3-11**.

The first set of lenses the electron beam traverses in a TEM is the condenser-lens

system. These lenses focus the electron beam onto the specimen. As seen in **Figure 3-9**,

this system usually consists of at least two lenses (C1 and C2). The first condenser (C1)

lens is a strong magnetic lens with a lower focal length $f$ (< *2 mm*) that concentrates and

demagnifies the electrons leaving the gun.  Ultimately, the achievable resolution is affected by lens defects, such as spherical aberration (scattering at different angles) and chromatic aberration (scattering at different wavelengths). Often there are aberration correction lenses to address these issues, and their affect on the final imaging resolution is minimized. The second condenser (C2) lens is a weak magnetic lens (higher focal length) that converges the beam as it passes through the aperture without affecting the magnification. Focus conditions are varied through changes in current through the lens–increasing the current can result in an over-focused image, while decreasing the current results in an under-focused image.

The specimen is secured to the stage of a specimen holder, and is transferred through an airlock system into the TEM column within the objective-lens system. The specimen position within the column is controlled by the goniometer. The specimen is positioned into the path of the electron beam for measurement of interactions as it traverses the specimen. Generally, electron-specimen interactions are characterized by the nature of their scattering. Electrons that experience no scattering maintain their incident energy through transmission. Elastic scattering is also an energy conserving mechanism. A transmitted beam of elastically scattered electrons is referred to as the diffracted beam. Energy conservation does not occur for inelastic scattering events, thus these electrons experience a loss of energy in transmission. All of these events provide information about the chemistry and structure of the specimen.
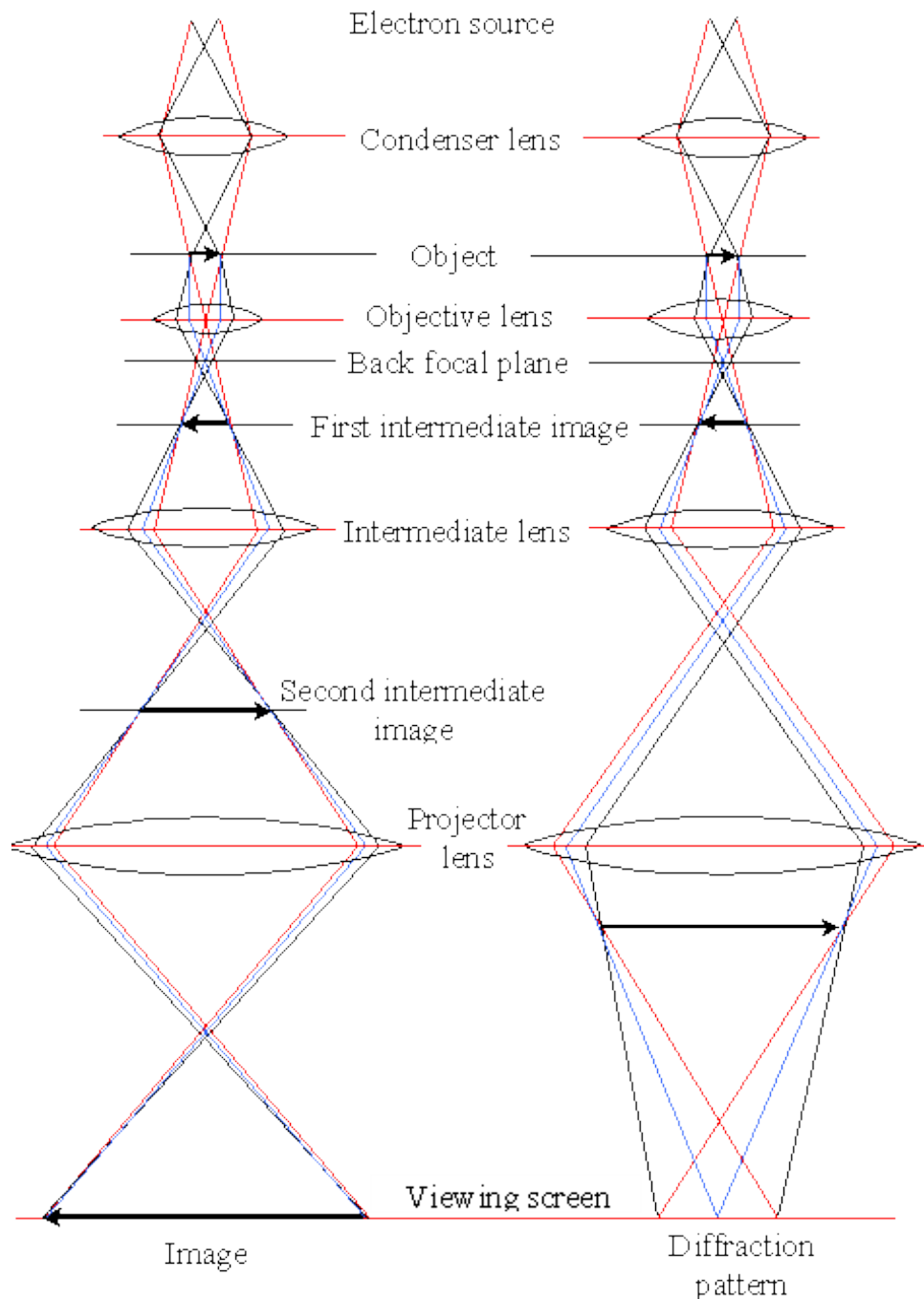
**Figure 3-12. The two basic operations of the TEM imaging system: projecting an image, and projecting a diffraction pattern. Adapted from** [74]**.**

The imaging system consists of the lens-systems that manipulate the image or

diffraction pattern formed from the electron-beam interactions with the specimen. These

include the objective, intermediate, and projector lenses **(Figure 3-12)** [74]. The

objective lens disperses transmitted electrons to create a diffraction pattern in the back focal plane, and recombines them to form an image in the image plane. The intermediate lens magnifies the image by changing the focal length, and TEM magnification ranges of $10^3$-$10^6$ are achievable. Finally, the projector lens projects an image or a diffraction pattern over the viewing plane. The image produced can also be viewed on a computer screen or captured using a CCD camera.

The operating principles of electron-specimen interaction in TEM present a unique opportunity to characterize and probe magnetic structure with high resolution. From the prior discussion of electron trajectories through magnetic fields in the electron lens, it is known that Lorentz force on an electron with velocity $\vec{v}$ is proportional to $\vec{v} \times \vec{B}$. When an electron passes through a thin magnetized film, the electron undergoes a deflection by interaction with the magnetization of the specimen in accordance with the Lorentz force. Lorentz-force TEM (LTEM) takes advantage of this interaction and captures the information in imaging.
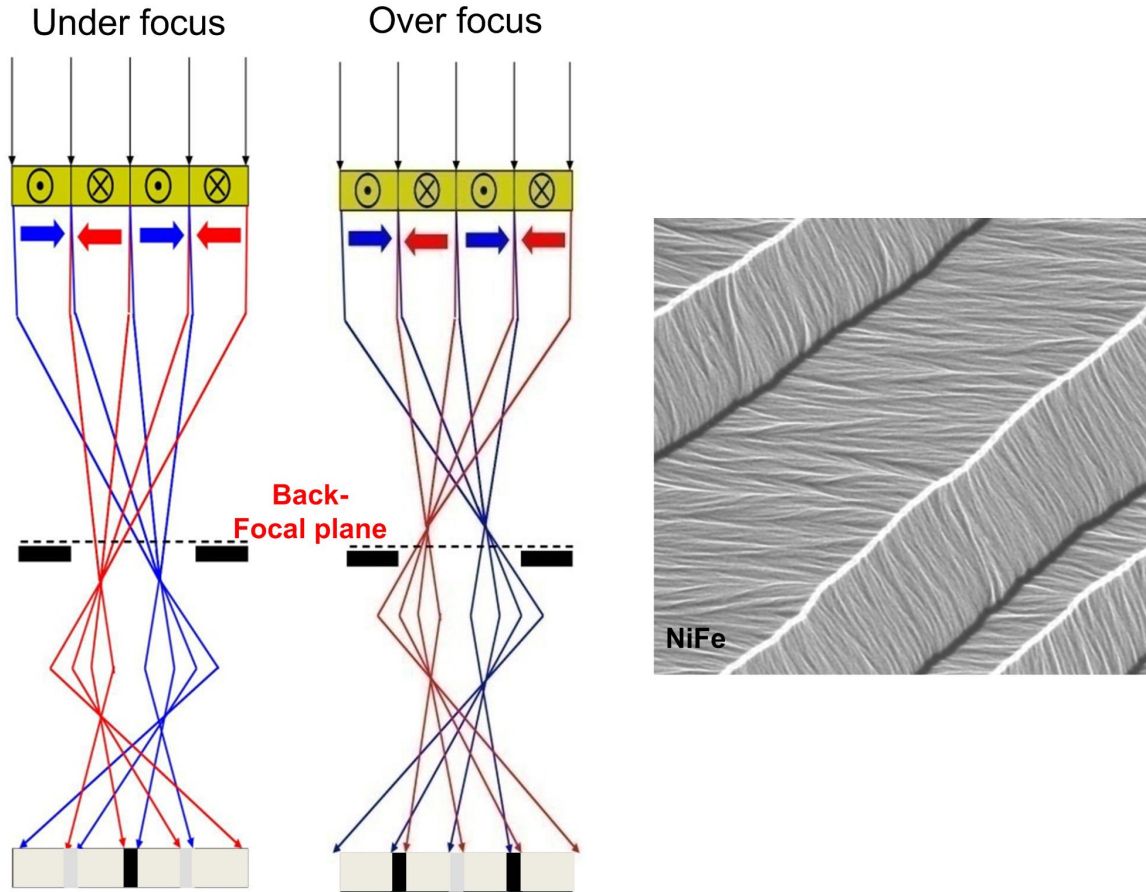
**Figure 3-13. Schematic of TEM electron-optics for Fresnel contrast. The bright/dark lines correspond to domain walls in the permalloy sample. Adapted from** [75]**.**

There are two operating modes of LTEM: Fresnel, and Foucault contrast [74]–[80]. **Figure 3-13 (a)** illustrates the method of TEM operation to achieve Fresnel magnetic contrast [75]. Fresnel magnetic imaging is a form of phase-contrast microscopy, and provides dark and/or bright contrast of domain walls as observed in a permalloy film in **Figure 3-13 (b)**. If electrons pass through a region in the specimen with opposing magnetization $\vec{M}$ in two adjacent domains, these electrons will be deflected in opposite directions. The deflections redistribute the electron-beam intensity over the image plane. Regions of beam divergence (dark lines) and convergence (bright lines) indicate domain walls. Fresnel contrast is obtained by: over-focusing of the condenser to give a small,

distant illuminating source, inoperative objective lens (except for small fields to induce film switching), and projector magnification to create large defocusing of the image [74]–[80]. This mode of magnetic imaging is a useful tool for in situ characterization of domain wall dynamics, and small and slow variations in the magnetization of a specimen.
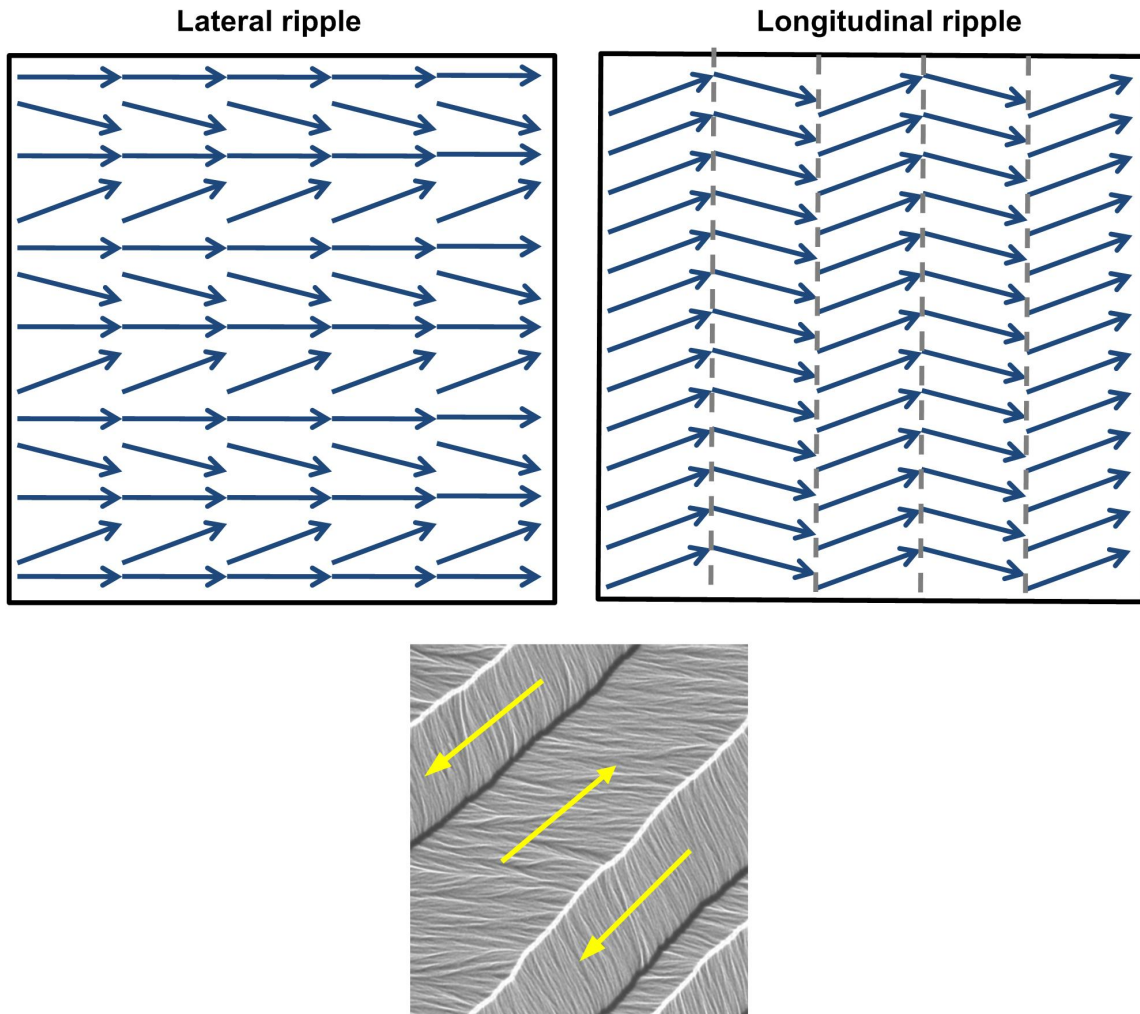


Figure 3-14. Schematic of lateral and longitudinal variations in local magnetic structure. The more energetically favored longitudinal arrangement results in magnetization texture that runs perpendicularly with the overall magnetization of the domain. Adapted from [75].

**Figure 3-13 (b)** shows Fresnel contrast of domain walls in a permalloy thin film. In addition to the regions of major intensity variations (at the domain walls), an intensity

texture throughout the film known as magnetization ripple is also present. **Figure 3-14**

**(a)** illustrates two ways which these intensity variations are possible in any given vector

field [75]. It is assumed that the film consists of grains with randomly oriented easy axis

in the plane of the film. Thus small amplitude, periodic variation in the magnetization

direction occurs either perpendicular to, or parallel to the direction of the net

magnetization, or lateral or longitudinal magnetization ripple, respectively. However, the

magnetostatic self-energy for lateral ripple is generally larger because of interactions at

the grain boundaries. Thus the longitudinal ripple is a more energetically favorable

arrangement [74]–[80].  As a result, bands of uniform intensity running perpendicular to

the principal magnetization direction form in the magnetic contrast image. This texture is

a useful tool as an orthogonal map of the magnetization distribution in the plane of a thin

film, as demonstrated in the permalloy film in **Figure 3-14 (b)**.
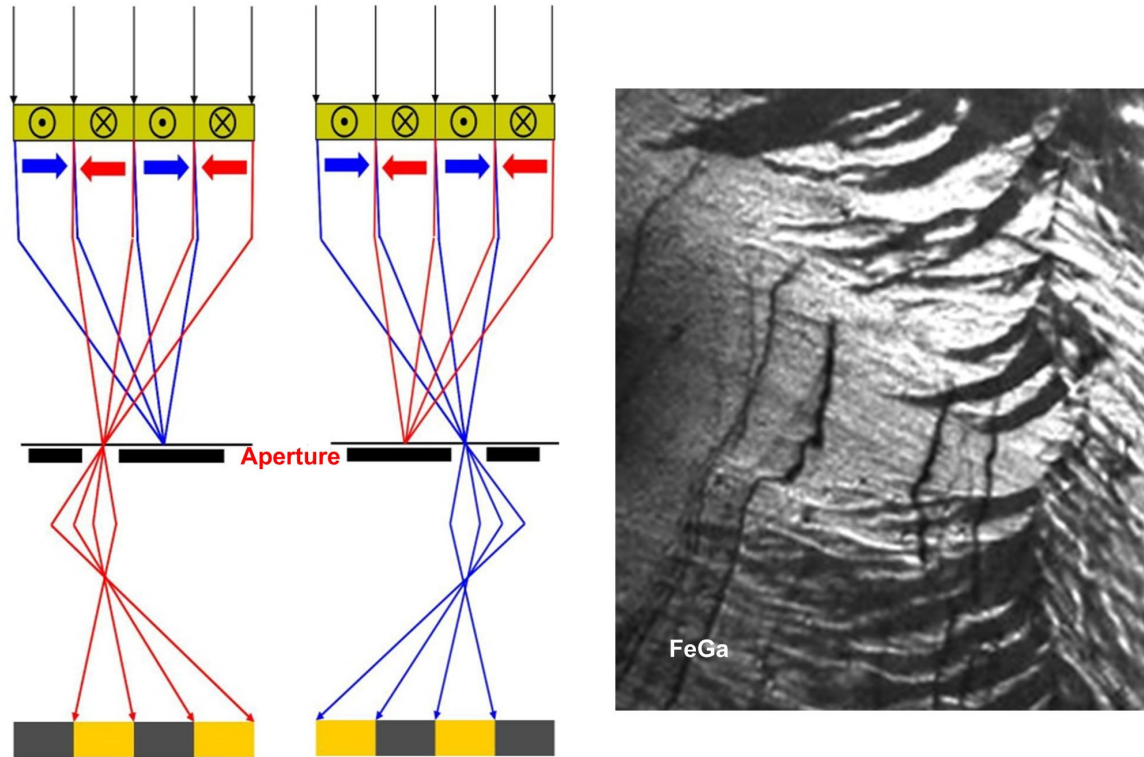
**Figure 3-15. Schematic of TEM electron-optics for Foucault contrast. An aperture in the back focal plane serves as a knife-edge to select or block specific domain deflections. The result is dark field contrast of a magnetic domain, as seen in the FeGa thin film. Adapted from** [75]**.**

In-focus characterization of magnetic domains in a thin film can be achieved with Foucault magnetic contrast imaging [74]–[80]. The mode of operation for generating Foucault contrast is illustrated in **Figure 3-15 (a)** [75]. If there are several domains present in the electron-illuminated area, the electron beam will be deflected in different ways by different domains. This results in a splitting of the diffraction spot. In this case, the objective lens operates at reduced strength to focus the virtual object plane (back focal plane, where the diffraction pattern is realized) on the projector focal plane. An objective aperture at the back focal plane is used as a knife-edge to select or block specific diffraction splitting. This results in a dark-field image of the magnetic domain structure, where the chosen spot will appear bright and all other domains will appear darker, as is observed for the FeGa thin film in **Figure 3-15 (b)**.

Fresnel and Foucault magnetic contrast techniques are used to observe magnetization events occurring in the magnetostrictive FeGa thin films with simultaneous mechanical interaction. These experiments were performed at the University of Maryland's Nanoscale Imaging Spectroscopy and Properties (NISP) Laboratory. A JEOL JEM-2100 $LaB_6$ TEM was used for magnetic characterization with LTEM. The incorporation of the objective mini lens in the TEM, for field-free imaging conditions, with special modification provides the ability of performing LTEM experiments. Electronics external to the microscope moderate current to the objective lens for calibrated control of magnetic fields. In this manner, in situ experiments are performed exploring the hysteresis of magnetostrictive FeGa thin films with applied magnetic field and stress.

### 3.3.2 Thin Film manufacture
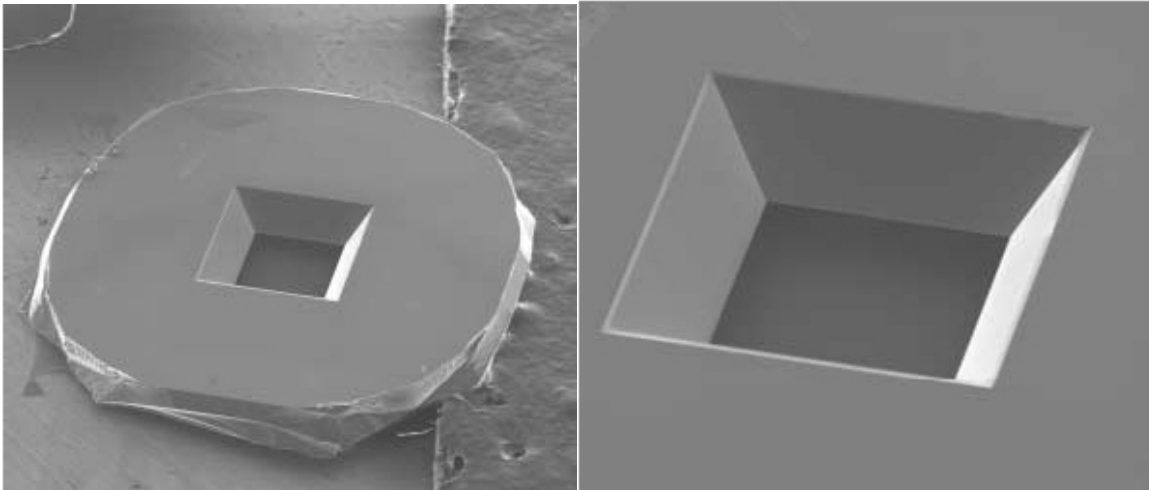


**Figure 3-16. SEM of SiN windows for TEM. Taken from** [81]**.**

Thin films of $Fe_{0.7}Ga_{0.3}$ are deposited using DC magnetron sputtering onto freestanding silicon nitride membranes. Silson™ manufactures silicon nitride membrane windows specifically designed for TEM. The window consists of a *2.65 mm × 2.65 mm*, *200 μm* thick silicon frame, which contains a *0.5 mm × 0.5 mm*, *100 nm* silicon nitride membrane, as pictured in **Figure 3.16**. Low-stress silicon nitride membranes are deposited using low-pressure chemical vapor deposition (LPCVD) onto both sides of a silicon wafer. One membrane serves as a mask for the selective etching process from the backside of the structure (using KOH anisotropic etching), creating a window opening in the center of the structure with membrane supported across. Stoichiometric $Si_3N_4$ membranes have relatively high residual stress, which produces a less robust film. Low stress membranes, used for these experiments, have a Si:N ratio greater than 3:4, or silicon rich, with $SiN_x$ stoichiometry. The thin membrane window facilitates two functions in the experiment: electron transparency for TEM observations, and a mechanically released substrate for enhanced mechanical range.

All samples were deposited in an ultra-high vacuum sputtering chamber. The base pressure prior to deposition was lower than $5 \times 10^{-8}$ *Torr*, and depositions were carried out in high purity Ar (99.9995%) at a pressure of *4.6 mTorr*. The substrates were the SiN/Si windows previously described. All FeGa depositions were performed at room temperature with a target-sample distance of *14.2 cm*. A gun power of *40 W* was maintained through the course of the deposition (~ 3 min) to yield *~20* nm thick films, as measured with surface profilometry.
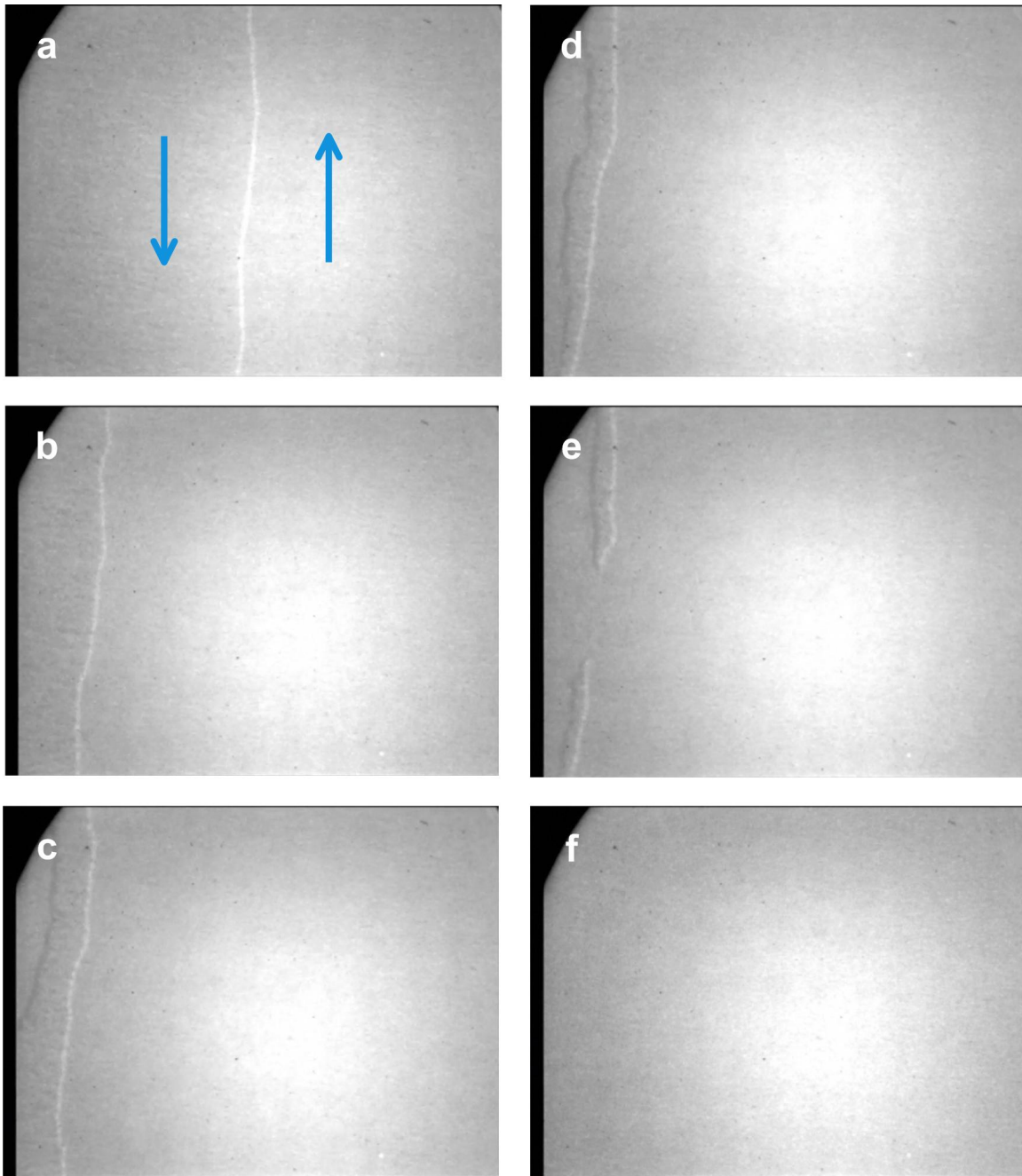
**Figure 3-17. Sequential image "stills" from a video clip demonstrating magnetization reversal in the FeGa/SiN sample with Fresnel contrast LTEM. The reversal is the result of increasing external magnetic field from -160 – +160 G. Blue arrows indicate the polarization for the two domains separated by a 180º domain wall (bright line).**

**Figure 3-17** is a sequence of still images from a video demonstrating a

magnetization reversal process using applied field. The *FeGa (20 nm)/SiN (100 nm)*

sample is secured within a conventional side-entry TEM holder.  The holder stage is tilted 32º with respect to the x-axis in the TEM column in order to experience a magnetic field component from the objective lens within the plane of the film. This is necessary as the film's shape anisotropy is confined parallel to the film surface.

The images in **Figure 3-17** are plan-view of the film with LTEM using Fresnel magnetic contrast. The current to the objective lens is externally controlled to generate a *-160 – +160* G magnetic field sweep for full reversal of the film. In **Figure 3-17 (a)** a bright contrast line is visible, extending from the top to bottom of the frame. This is Fresnel contrast of the 180º domain wall separating the two oppositely polarized domains, magnetization is represented as blues lines. As the magnetic field is increased, the domain polarized in the direction of the field grows in size while the oppositely polarized domain shrinks. This is dynamically observed as motion of the domain wall toward the left of the frame. In frame **(c)** a second domain nucleated outside of the field of view has grown in to view. The oppositely polarized domain continues to shrink with increasing field, until finally the film is uniformly polarized. Through the course of the reversal, the only environmental condition that varied was the current to the objective lens; consequently the objective lens field strength. Thus, as the image contrasts change with the varied field, it is confirmed that these artifacts are of magnetic origin. This demonstrates both the magnetic integrity of the fabricated films, and the capability of LTEM to characterize magnetic properties.

### 3.3.3 Patterned Structures
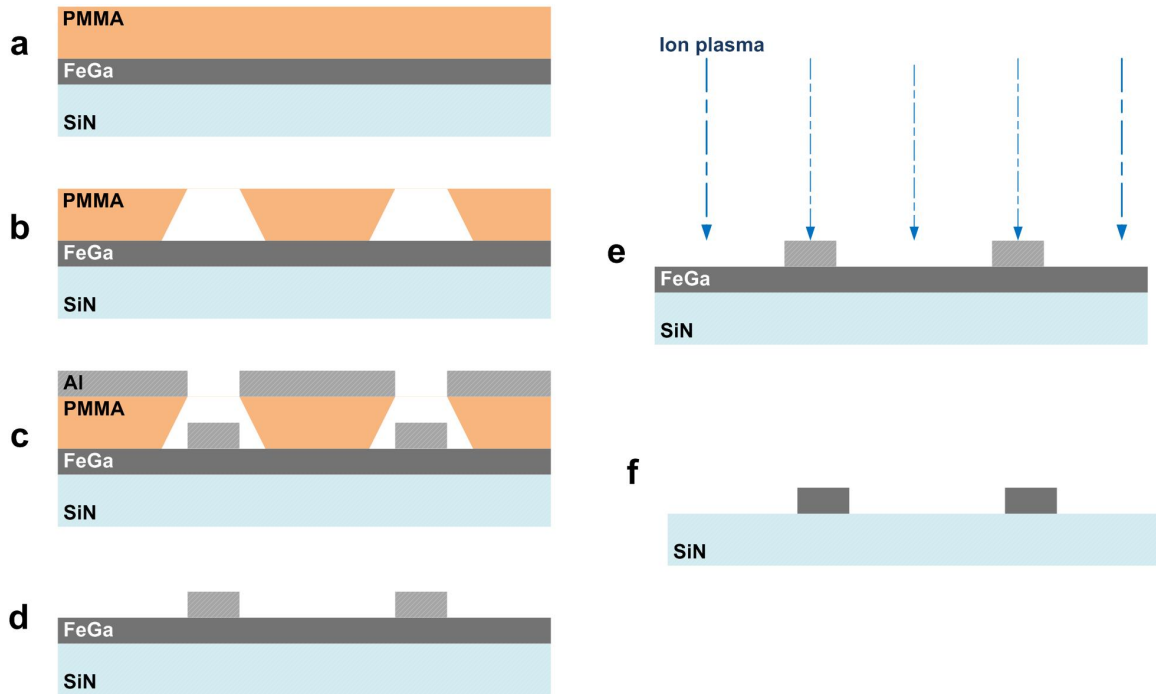


**Figure 3-18. Cross-sectional illustration of lithography process for patterned FeGa magnetic nodes. (a) A PMMA bilayer is spin-cast onto continuous FeGa thin films. (b) Lithographically patterned square voids remain after development. (c-d) Patterned resist serves as a mask for pattern transfer during evaporation of Al film onto the surface. Lift-off reveals a patterned mask of Al squares. (e-f) Subsequent ion-milling etches the Al mask and exposed FeGa film, leaving patterned media on the SiN substrate.**

Magnetic memory nodes are patterned from continuous FeGa thin films on silicon nitride membranes as an array of patterned media using a positive-resist electron-beam lithography method. **Figure 3-18** depicts the patterning process which includes a patterned resist mask for evaporation, and a patterned Al mask for ion-plasma etching. A bilayer resist film of *PMMA 950/PMMA 495* is spin-coated onto the *FeGa/SiN* structure with *6000 rpm* spin speed for 45 seconds (5 sec acceleration and deceleration). Each resist layer is baked for one hour at *180°C*.

The PMMA bilayer is subsequently patterned into a *0.5 mm × 0.5 mm* array of *500 nm × 500 nm* squares using the Raith e_LiNE ultra-high resolution lithography workstation at the University of Maryland's Fabrication Laboratory (FabLab). Electron-beam (*20 kV*–Gaussian round beam) exposure of the PMMA degrades its molecular structure such that exposed areas can be dissolved in a solvent. Thus the resist film serves as mask for pattern transfer.

Subsequent electron-beam evaporation of a *27 nm* Al thin film transfers the pattern such that an array of Al squares sit atop the continuous FeGa film after lift-off. Finally the sample is subjected to ion beam milling, where the both the Al patterned mask and exposed regions of the FeGa are physically etched away**.** Argon ions contained within plasma (formed by an electrical discharge) are accelerated by a pair of optically aligned grids. The highly collimated beam is focused on a tilted work plate inside the chamber that rotates during the milling operation. A neutralization filament prevents the buildup of positive charge on the work plate. The result is a patterned square array of individual magnetic elements on the SiN freestanding substrate, as seen in plan-view in

**Figure 3-19 (a)**. For TEM purposes, a *20 nm* Al thin film is evaporated on to the final

sample in order to prevent charge build-up when exposed to the electron beam.
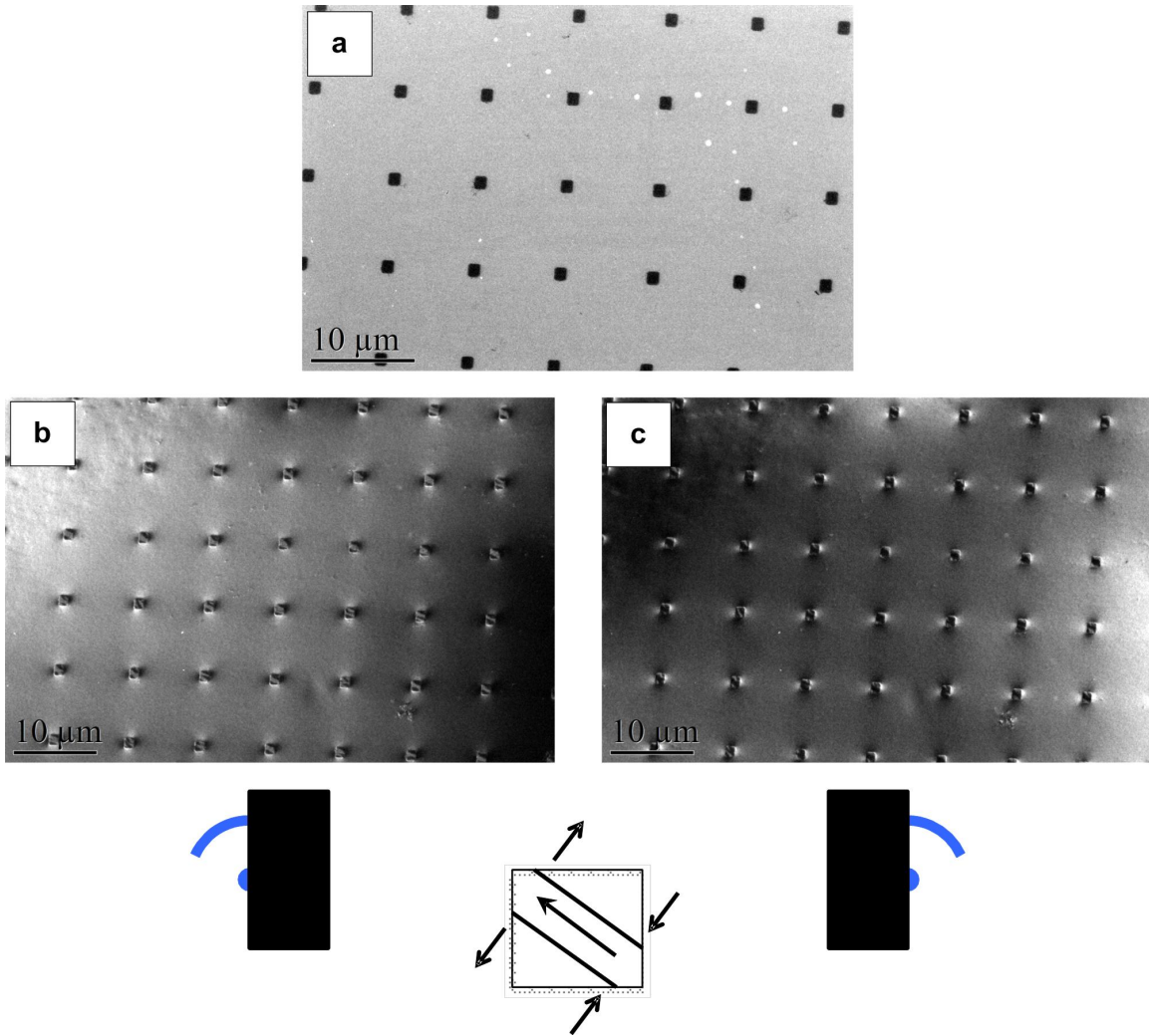


**Figure 3-19. (a) TEM of patterned FeGa array of *500 nm × 500 nm* squares using electron lithography. (b)-(c) Foucault magnetic contrast of the array captures the magnetic order within each element, and is schematically depicted. The contrast along the geometry border is due to the strong edge field. The contrast is simply reversed in these images with repositioning the edge of the back focal plane aperture.**

**Figure 3-19** shows the final result of the patterning process, and also Foucault

magnetic imaging contrast of the patterned sample. Contrast is present within both the

film of the individual elements, and around the edges of the elements. An aperture in the back-focal plane is maneuvered, as depicted in the figure, to block specific electron-beam deflections from their respective domains. The contrast reversal is obtained simply with repositioning the aperture to block the opposing deflection.

Each square element is divided into three domains with net magnetization running diagonally across the element, along the longest length axis of the media in accordance with the shape anisotropy. This domain structure is roughly depicted in **Figure 3-18.** Strong contrast is present on the edges of the element geometries due to the magnetic field associated with each magnetic element itself. Here, the sinks and sources of the magnetization behave as positive and negative "magnetic charges, " and is known as the demagnetizing or stray field (with energy represented in **Equation 3-1**). Thus electron transmission in vicinity of the edge field fringes surrounding each element experience Lorentz-force deflection, which contribute to the contrast. This strong contrast is a useful aid in determining the internal magnetic order, especially as the dimensions of the elements reduce.

# Chapter 4: Results & Analysis

## *4.1 Remanent states*

The FeGa/SiN sample is installed on the NanoFactory™ nanomanipulation holder for in situ experiments so that the effects of applied field and stress can be simultaneously observed with LTEM techniques. **Figure 4-1** shows the resulting domain structure from in situ field and mechanical interactions. The piezo-driven STM tip is taxied to the center of the thin film/membrane, and then pushed into the film in order to apply tensile stress. A beryllium-copper wire fixed to the STM tip is the primary probe for mechanical interaction with the film, and is visible in the micrographs. For scale reference, the wire diameter is *25 μm*. The electron-optical conditions are those necessary for capturing magnetic Fresnel contrast. The objective lens is only minimally excited in order to generate an external magnetic field, and the electron beam is either under-focused or over-focused to realize the phase contrast in the image plane, as illustrated in in **Figure 4-1 (a)**.

**Figure 4-1 (b)–(c)** represent the magnetic remanent state resulting from applied field with simultaneous deflection. In frame **(b)**, the mechanically loaded film is exposed to 80 G in the +X direction. Bright and dark contrast lines indicate the presence of domain walls, the separation of two distinct magnetic domains. In frame **(c)**, the contrast is reversed with a reversal of the field (*80 G* in the –X direction). Present in both frames is magnetization ripple texture throughout the field of view. The texture varies in orientation, wavelength, and amplitude in the region immediately surrounding the

deflection point. As previously reviewed, this texture is a useful guide to the local magnetization as the ripple runs orthogonally with the net magnetization. Thus, with this contrast it is possible to infer the magnetic structure of the film. Overall, the film is polarized in the direction of the applied field. However, the magnetization ripple indicates local deviations from the net polarization closest to the deflecting probe. The blue arrows in **Figure 4-1** depict the local magnetic domain structure in accordance with the ripple. With the application of stress to the film, 45º domains are created in the film.

Foucault contrast of magnetic domains is achieved, as illustrated in **Figure 4-2 (a)**, through the use of an aperture in the back-focal plane to intercept specific electron-beam deflections originating from a particular domain. A diffraction image occurs at this imaging plane, and because of the magnetic structure present in the film, the central diffraction spot (indicated by the cross-mark) is split according to their respective deflection. By positioning an aperture in this plane a particular domain is obscured in the viewing plane, resulting in a dark contrast image of the domain as illustrated in the figure.

The field and mechanical conditions previously described are maintained, thus the images presented in frames **(b)–(c)** represent the magnetic remanent state of the mechanically loaded film. The contrast clearly indicates the creation of domains as a result of the mechanical interaction. The contrast is reversed either with repositioning of the aperture or with field reversal.
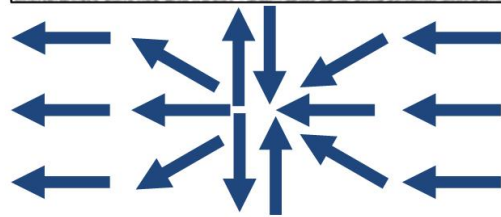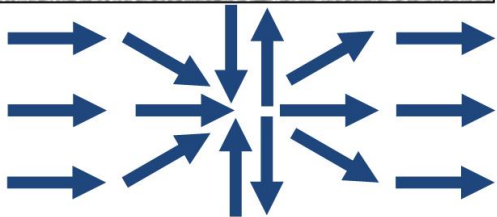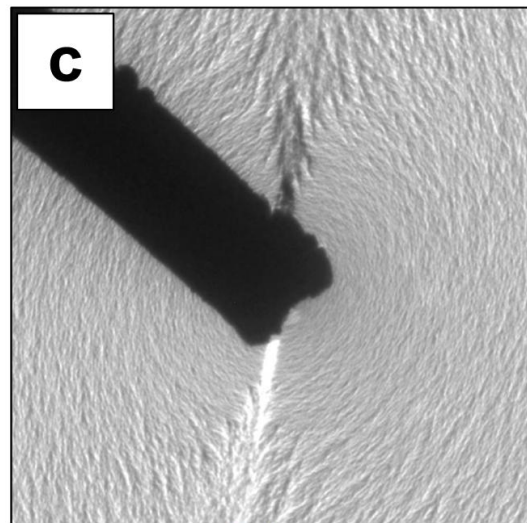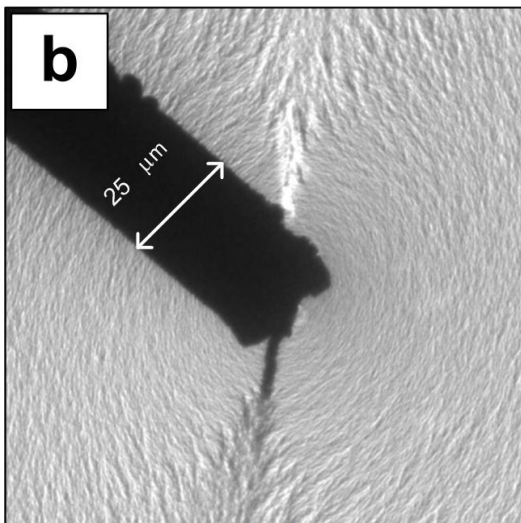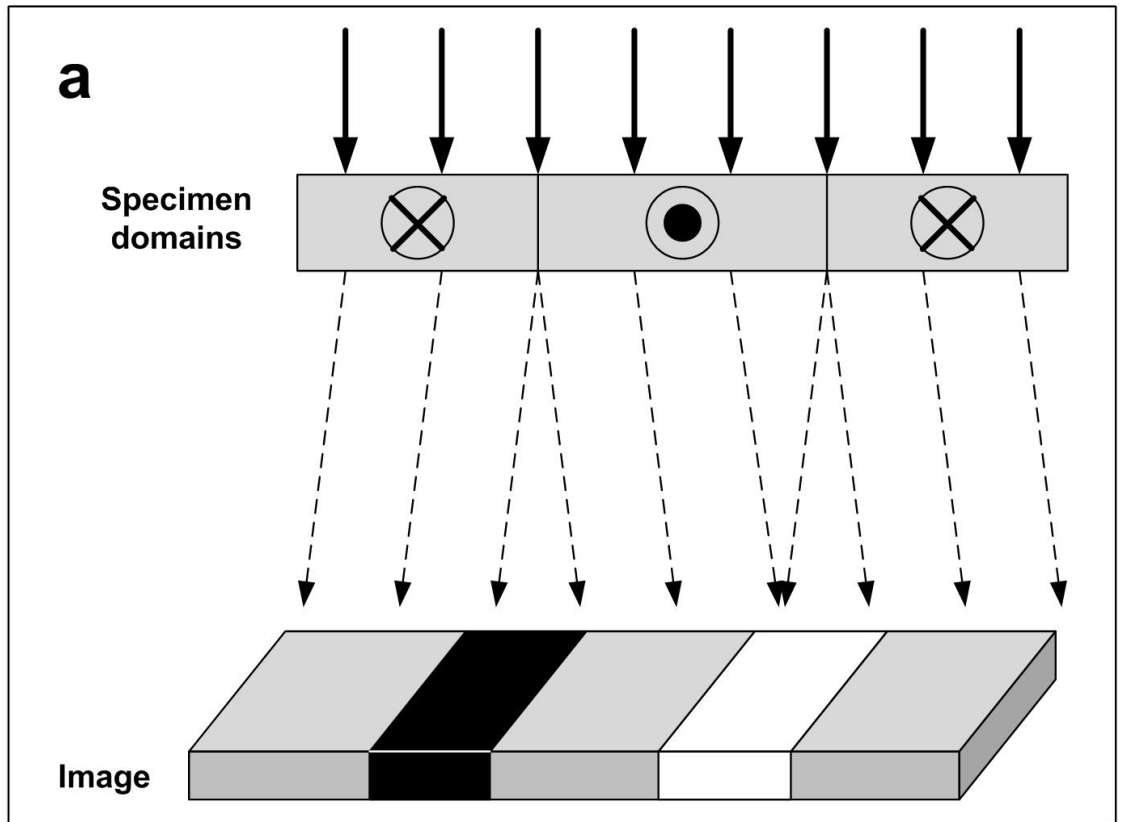
**Figure 4-1. (a) Schematic of LTEM operating mechanism for Fresnel contrast. (b–c) Fresnel contrast of the magnetic domain structure as a result of magnetic and mechanical stimuli. The contrast can be reversed with either a field reversal (resulting in domain reversal) or changing the beam conditions from over- to under- focus.**
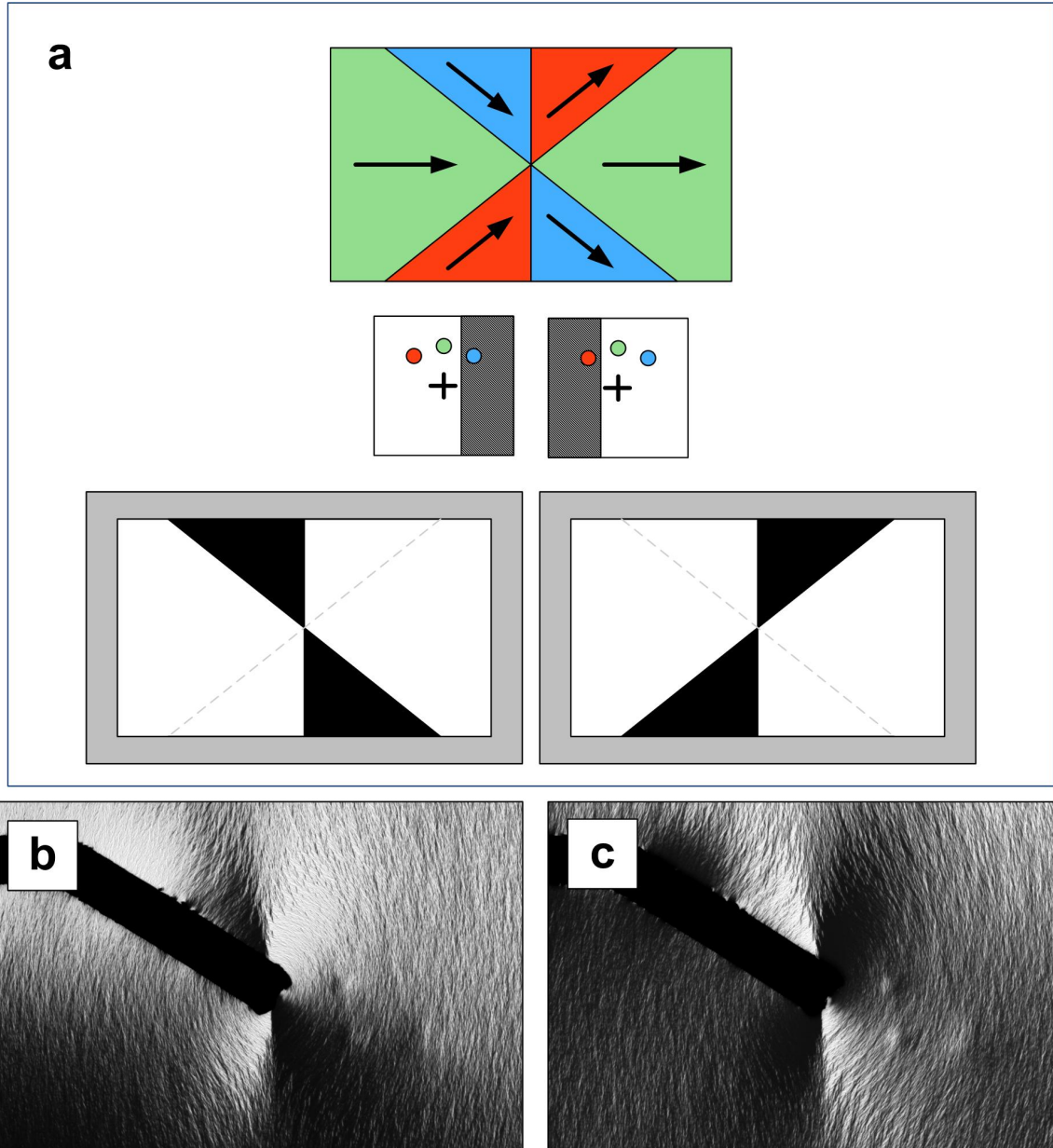
**Figure 4-2. (a) Schematic of LTEM operating mechanism for Foucault contrast. (b–c) Foucault contrast of the magnetic domain structure as a result of magnetic and mechanical stimuli. The contrast can be reversed with either a field reversal (resulting in domain reversal) or repositioning the aperture in the back-focal plane.**

The series of images presented in **Figure 4-3** demonstrate the magnetic and mechanical hysteresis with changes in applied field and strain, respectively. The insets of the images depict the specific history to achieve the resulting domain structure, where the blue dot represents the initial state, the blue line represents its hysteresis, and the red dot represents the final state, which is depicted in the Fresnel contrast LTEM image. Where applicable, applied fields are approximately *80 G* in the –X direction, and the film is deflected approximately *11 μm* from its initial position.

In **Figure 4-3 (a)**, the film experiences both field and stress initial conditions. First, the external field is zeroed, and the probe is retracted from the film (in the image the probe is no longer in contact with the film). The resulting domain structure resembles that of **Figure 4-1**– two distinct contrast lines appear adjacent to the point of contact, perpendicular to the direction of the applied field. As seen before in the region surrounding the probe, the ripple appears to be concentrically arranged closest to the point of contact, which thus suggests a radial configuration of the magnetization. The amplitude and wavelength of the ripple texture– which depend on the mean grain size, the magnetic anisotropy, film thickness, exchange constant, saturation magnetization, and externally applied field– are altered in this region around the probe [75]–[77], [82]. Therefore, since all factors impacting the texture are more or less consistent throughout the film, the changes in the uniaxial anisotropy in this region are stressed-induced and a result of the magnetostriction. However, the texture outside of this region remains relatively un-impacted by the stress field, and is instead influenced by the external field. Thus, there is a critical relationship in the overall anisotropy between the relative

105

strengths of the applied forces, and distance and orientation with respect to the point of film contact.

In **Figure 4-3 (b)**, the film begins with the same initial conditions. First retracting the stress probe, and then removing the external field reverses the hysteresis. The texture throughout the entire field of view runs perpendicularly to the applied field. Thus, the film is uniformly polarized. In the absence of the applied stress, the anisotropy dictated by the external field dominates the system, negating any prior influence of the magnetoelastic anisotropy. This also demonstrates the plasticity of the mechanically-driven magnetic texture, and the erasability of the previous magnetic structure.
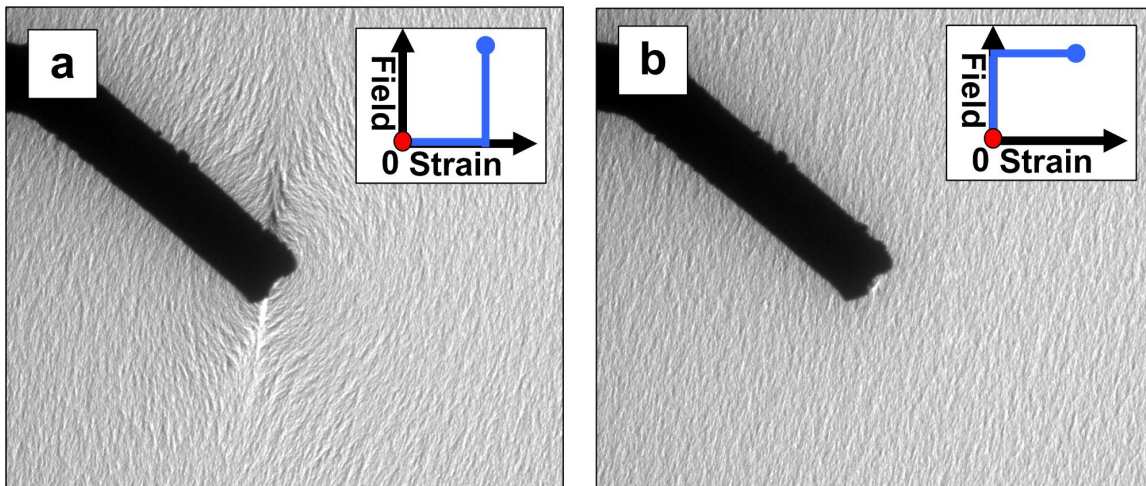


**Figure 4-3. Remanent states as a result of hysteresis in both applied field and strain. The hysteresis is depicted in the inset of the respective figure, detailing the initial state (blue dot), hysteresis path (blue line), and final state (red dot).**

### 4.2 Pure stress effects

Thus far, we have observed the resulting domain structure from mechanical and external field stimuli. The thin film is subjected to point-load deflection at its center

through a transverse force applied by the scanning tip. Since the sample is a two-dimensional system, it is expected that point-loading induces a radially symmetric stress around the source. Therefore it is expected that due to the radial nature of the stress, the induced magnetoelastic anisotropy will also follow the imposed radial symmetry, and it is reasonable to anticipate a radial magnetization arrangement about the point of contact. This is, in fact, what has been observed (see **Figures 4-1, 4-3, and 4-5**). It has been previously reviewed that the magnetic ripple texture present in Fresnel contrast micrographs is due to small undulations of the uniaxial anisotropy about the overall local magnetization, and thus, indicates the local magnetic order.
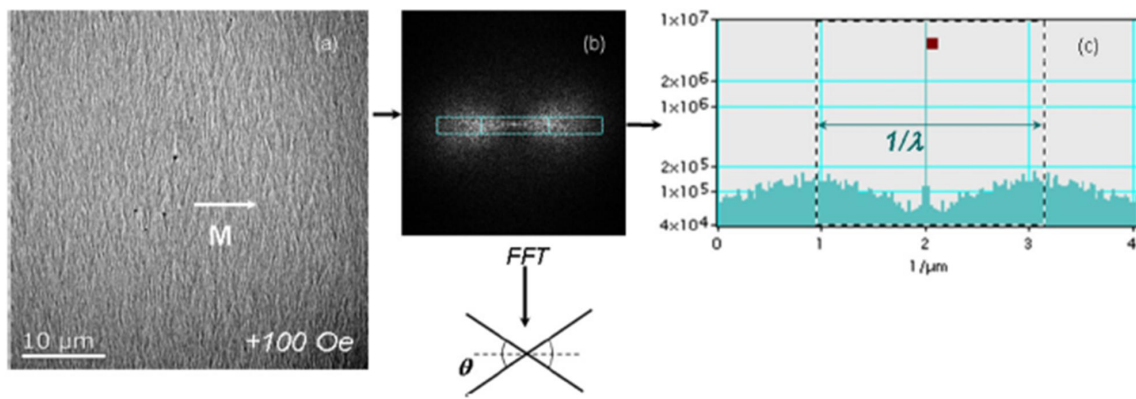


**Figure 4-4 Diagram of the calculation of ripple wavelength from Fourier transform of a Fresnel image. Taken from** [83]**.**

It has been widely seen in the Fresnel contrast images presented thus far, that the ripple does display radial symmetry nearest the probe; the radial effect being a result of the applied stress. Adhering to classical ripple theory, the magnetic ripple can be characterized in terms of the mean wavelength and the mean angle of deviation of the local magnetization [76], [77]. According to the theory, the mean wavelength is expected to vary as a function of the applied field as:

$$\lambda(h) = 2\pi(A/K_u)^{1/2}(h+1)^{-1/2} \quad \textbf{(Equation 4-1)}$$

where $K_u$ is the uniaxial anisotropy constant and $h = H/H_k$ is the reduced magnetic field (with $H_k$ being the anisotropy field). It is possible for the wavelength to be measured by an analysis of the Fresnel contrast images in Fourier space. An example of this analysis from Ngo et al. is presented in **Figure 4-4** [83]. From a fast Fourier transform image (FFT) of a Fresnel image with homogeneous ripple, the mean wavelength can be measured from a line profile of the FFT image modulus along the magnetization direction (presented by the dashed line axis of the triangle). Here, the distance between the two peaks in the profile can be converted into a real space value for the wavelength. However, such an analysis is outside the scope of this dissertation. The primary information that is interpreted from the ripple is the orientation of local magnetization.

From the equation we can see the relationship of the wavelength with the uniaxial anisotropy. For large anisotropy values, the ripple wavelength is expected to be small, while smaller anisotropy produces a larger wavelength. This relationship is also evidenced in the Fresnel images presented herein. During the mechanical loading process (**Figure 4-1 and 4-5**), the magnetic ripple texture with radial symmetry is finer than the texture that exists outside of the influence of the imposed magnetoelastic anisotropy.

Thus, the mechanical interactions are responsible for increasing the anisotropy within this region. Next we will take a closer look at the isolated effects of applied stress on the local magnetic order.
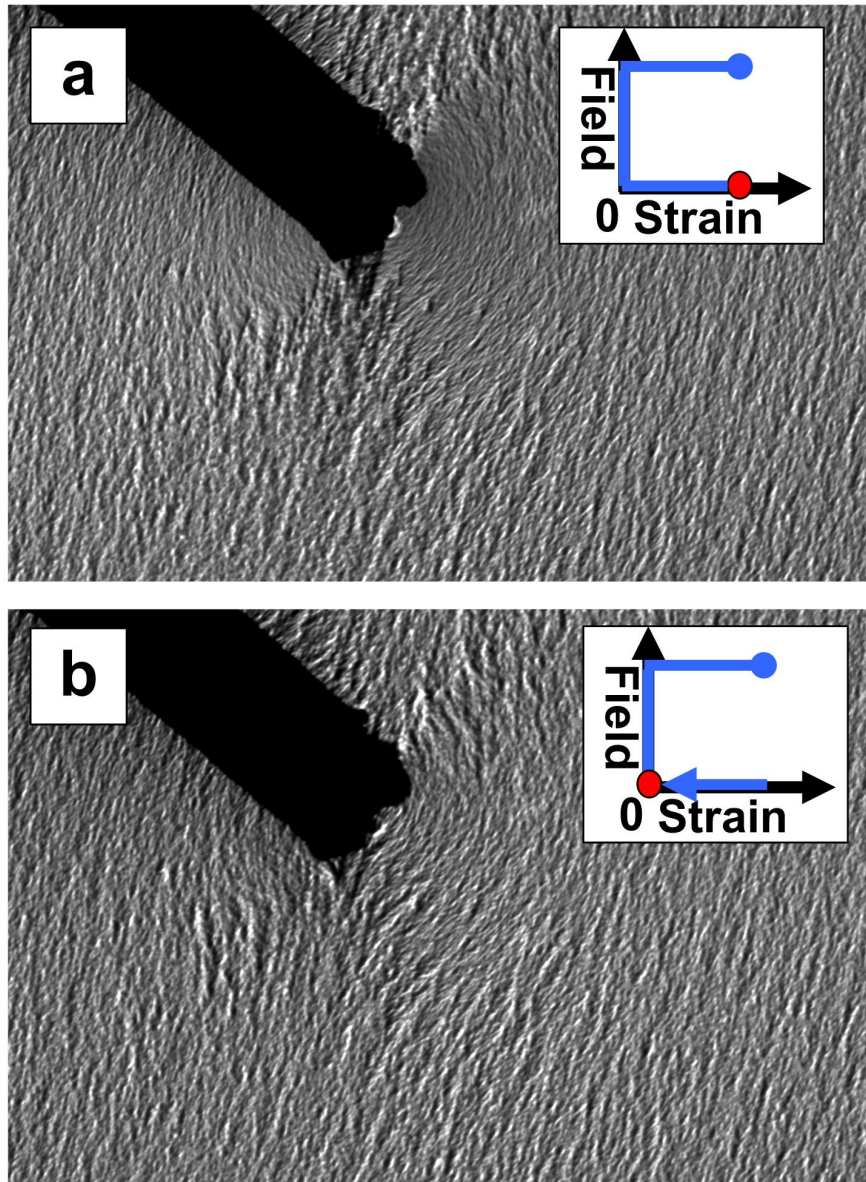


**Figure 4-5. Magnetic remanence purely due to stress effects. (a)-(b) The probe remains pressed into the film, and the remanence is captured in (c) upon retraction of the probe.**

**Figure 4-5** continues on the hysteresis path established in **Figure 4-3 (b)**. The probe is directed back into the film for mechanical loading while the field conditions are maintained at zero. The result is a magnetic domain structure solely due to mechanical interaction, and thus, represents the magnetizing effects of magnetostriction. In **Figure 4-5 (a)**, the purely stress induced magnetic domain structure is seen only through the fine contrast of magnetization ripple and lacks the domain wall contrast that is present with external field. Figure **4-5 (b)** magnified the magnetic structure, where it is clearly visible that the ripple wavelength and amplification are altered in the region surrounding the probe. This effect extends out to a radius of approximately *25 μm* on either end of the probe before the ripple is restored to its initial state. Thus the anisotropy previously established by the field is dominant in regions outside of this radius, and the magnetoelastic anisotropy dominates within the boundary.

      **Figure 4-5 (c)** shows the magnetic remanence observed upon retraction of the probe from the film. Despite increases in the ripple wavelength and amplitude, permanent changes to the anisotropy of the film are seen as the now-familiar radial orientation of the ripple closest to the point of contact. This process thus demonstrates magnetic recording without the use of external magnetic fields.

      Finally, we look at the dynamics of the induced strain when the tip is not stationary. The load of the scanning tip can shift during contact to traverse the surface of the thin film. This is due to spuriously low friction in some samples. Shifting the partial load effectively draws recorded domain walls over the area it scans. **Figure 4-6** demonstrates this effect as image 'stills' extracted from a real time recording of the interaction.

First, without any loading, the film is uniformly polarized in the +Y direction to induce weak uniaxial anisotropy in the film. In field-free conditions, the probe is brought to the film surface to partially load the film. This partial loading is the result of non-orthogonal contact with the film, and thus the tip is unable to transversely deflect the film. In **Figure 4-6 (a)** evidence of the partial deflection is seen in the occurrence of radial magnetic ripple mildly encircling the point of contact. Unlike previous examples of loading, the radius of induced modifications to the magnetic ripple has shrunk to about one-third of its previous span. This feature is indicative of the partial loading.

In frames **(b)** and **(c)** the tip shifts its load in the –X direction towards the top of the image. In its wake there is obvious contrast of a domain wall along with the occurrence of semi-radial ripple symmetry, indicating both strong and weak deviations of the magnetic order along its path. The contact of the tip with the surface decreases as it drags along, this is due to both variances in the film height (as it is secured at an angle in the holder stage) and inconsistencies associated with the coarse motion driving the tip. The contact is restored when the tip arrives in the middle of the image using the fine motion to push it back into the film. The kink in the domain wall in frame **(c)** is a result of this position adjustment. However, this defect is indicative of the spatial resolution of the effect. The domain wall, and other alterations to the local anisotropy, is stable even after the deflection field has cleared the region, thus demonstrating the magnetic remanence associated with the sole use of mechanical stimulus.

In frames **(d)–(f)** the tip motion is reversed to the + X direction, as it rescans its initial path. Upon this reversal, a change to both the domain wall contrast and ripple orientation is captured. The tip effectively reverses the domains it previously wrote, and

111

again, the newly emerged order is stable even with distance from the deflection wake. The reversal is dictated by the direction of the tensile strain, which directly influences the magnetoelastic anisotropy. The strain concentrates at the point of contact and distributes symmetry about the path axis. Thus, the symmetry of the stress field is translated to magnetoelastic anisotropy, which is, in turn, evidenced in the ripple orientation and contrast of the domain wall.

In frame **(g)** the original contact with the film is lost, and the stylus is repositioned next to its original path. The tip traces a path next to the previously scribed domain wall in the center of the image. Both dark and bright contrast walls lie adjacently, thus demonstrating the stability of a previously written wall, even as it lies in the vicinity of opposing anisotropy.

Now that the effects of pure stress have been witnessed, we next analyze the energy associated with this interaction, and how it impacts the local magnetic order.
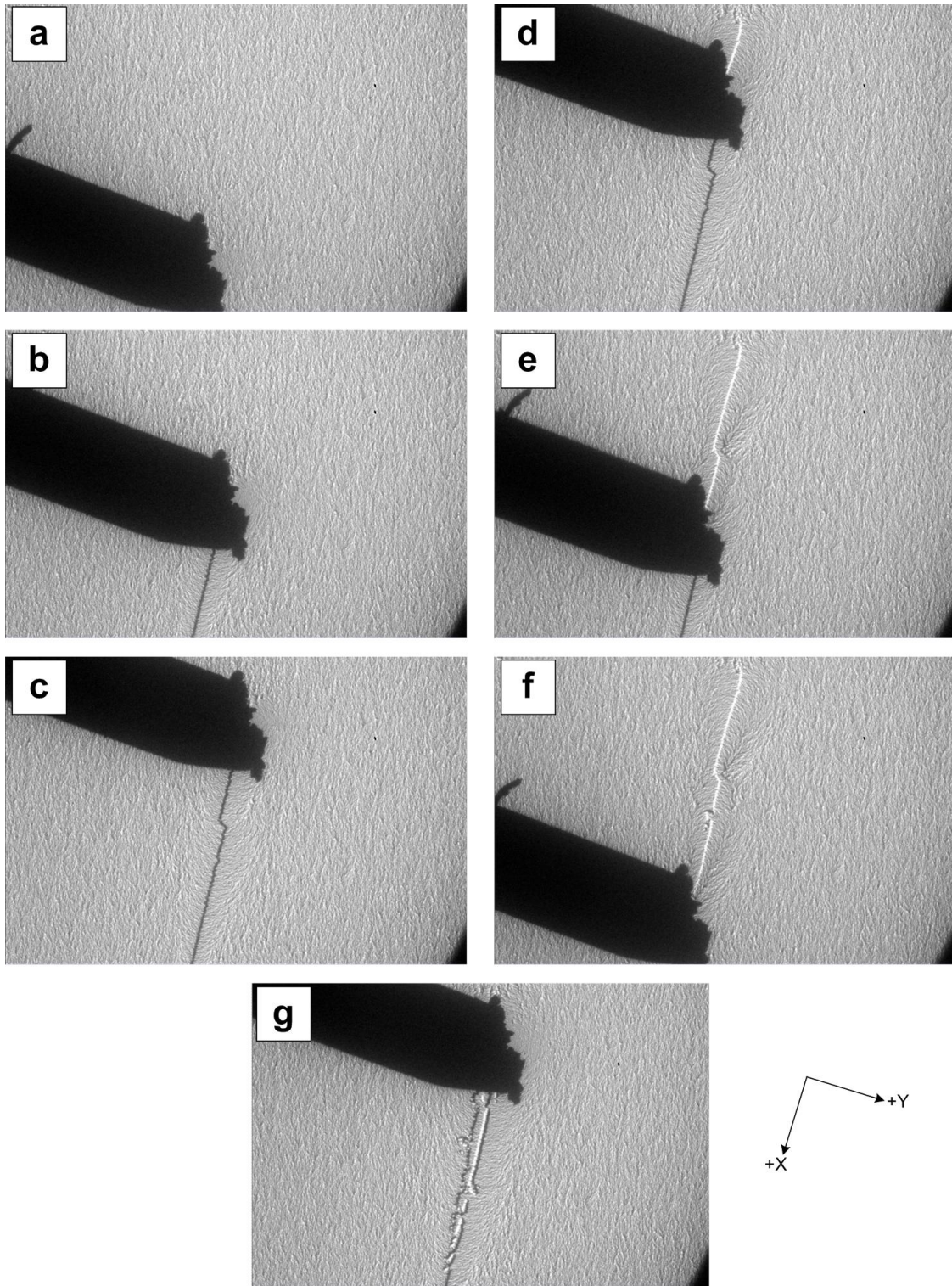
**Figure 4-6. Image stills from a real-time recording domain wall writing with applied stress. (a)–(c) The stylus maintains partial loading as it travels in –X. Dark domain wall contrast as well as semi-radial ripple remains after its passing. (d)–(f) The tip motion is reversed, and it retraces its original path going +X. Bright domain wall contrast replaces the dark contrast, and the ripple is also reoriented. (g) The stylus is repositioned next to the previous path and draws a dark contrast wall alongside the remaining wall.**

## 4.3 Analysis of magnetoelastic effects

### 4.3.1 Heuristic Model

The magnetic ripple featured in Fresnel contrast images has proved to be a valuable tool for analysis of the magnetic structure thus far. Once again, we rely on this texture to understand more about how magnetoelastic effects on the domain structure is realized. **Figure 4-7 (a)** displays Fresnel contrast of a mechanically loaded continuous FeGa film simultaneously immersed in *+80 G* external field along the +X direction. There are two main ripple textures present in the film: one that appears with radial symmetry about the tip, and one that runs perpendicularly with the applied field (surrounding the radial region). Our attempt to explain the domain structure that results from these interactions begins with measuring the magnetization orientation, or rather, the angle $\phi$ that lies between $\vec{M}$ and the applied magnetic field (which is depicted in **Figure 4-7**).

The ripple texture in this image was measured manually, where the angle $\phi$ is extracted from a canted line that runs parallel with the local striations in the ripple. **Figure 4-7 (b)** depicts the resulting map of $\phi$ and its variance in a space parameterized by the radial distance $\vec{r}$ from the point of contact, and the azimuthal angle $\theta$ about that origin. Here we see the emergence of 45º domains that form around the tip, and outside of a critical region, the magnetization remains unaffected by the applied stress; instead following the imposed field anisotropy. Thus $\phi(\vec{r})$ is a result of these two competing anisotropies. We next explore this relationship.

114
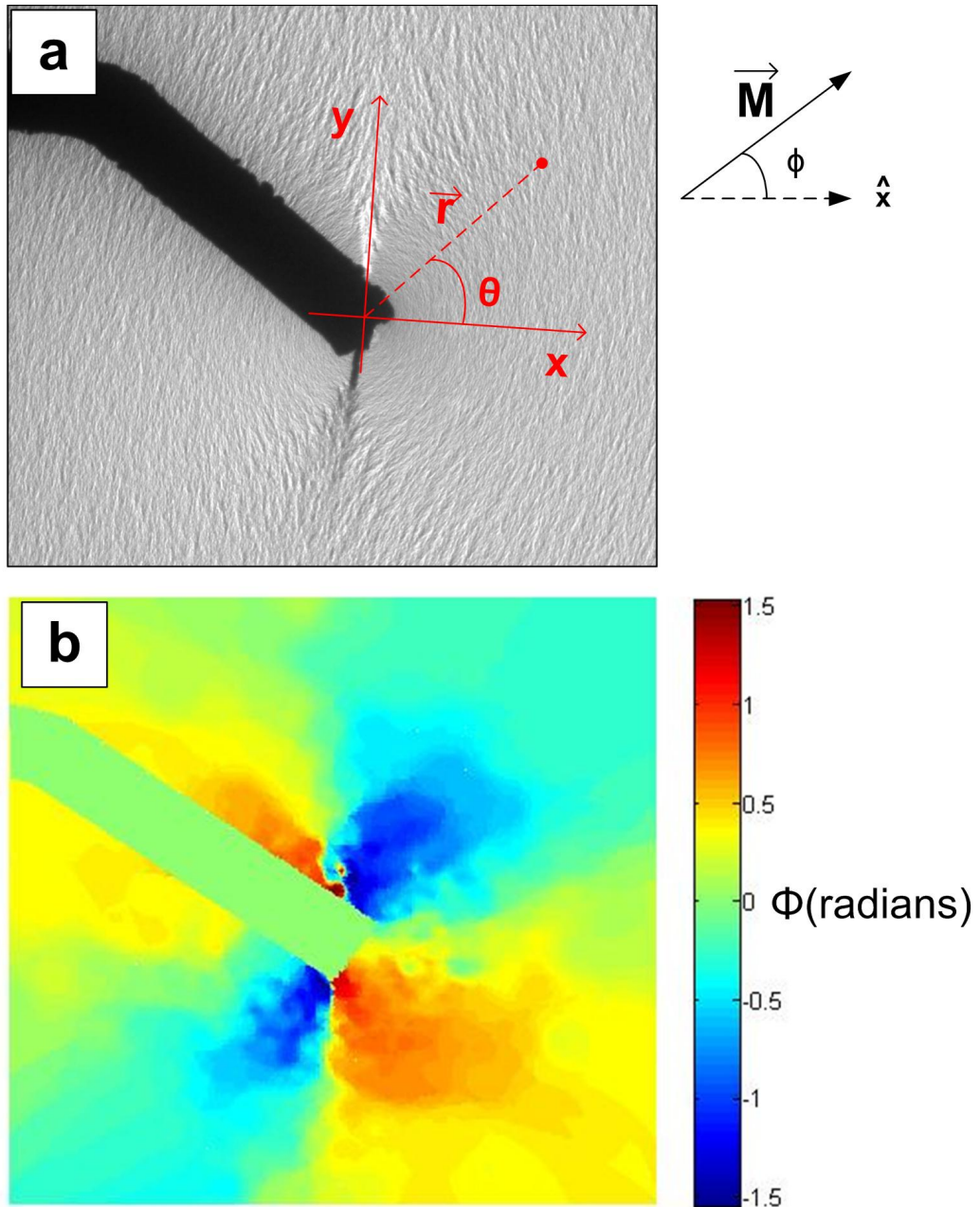
**Figure 4-7. (a)** Fresnel contrast of FeGa film experiencing both mechanical loading and applied field. The magnetization $\vec{M}(\vec{r})$ is characterized by the rotation $\phi$ away from the direction of the field generated uniaxial anisotropy. **(b)** $\phi(\vec{r})$ is manually measured from the ripple texture, which lies orthogonally to $\vec{M}(\vec{r})$. The magnetic domains are thus characterized by $\phi(\vec{r})$.

Generally, micromagnetic dynamics are based on the same variational principle, which is derived from thermodynamic principles. This principle dictates that the vector field of magnetization directions is chosen such that the total free energy, or the energy that can be converted to do work on a dipole moment, reaches an absolute or relative minimum [27], [84]. Thus, the magnetic state of a system is a competition among exchange, anisotropy, magnetoelastic, and magnetostatic energies.
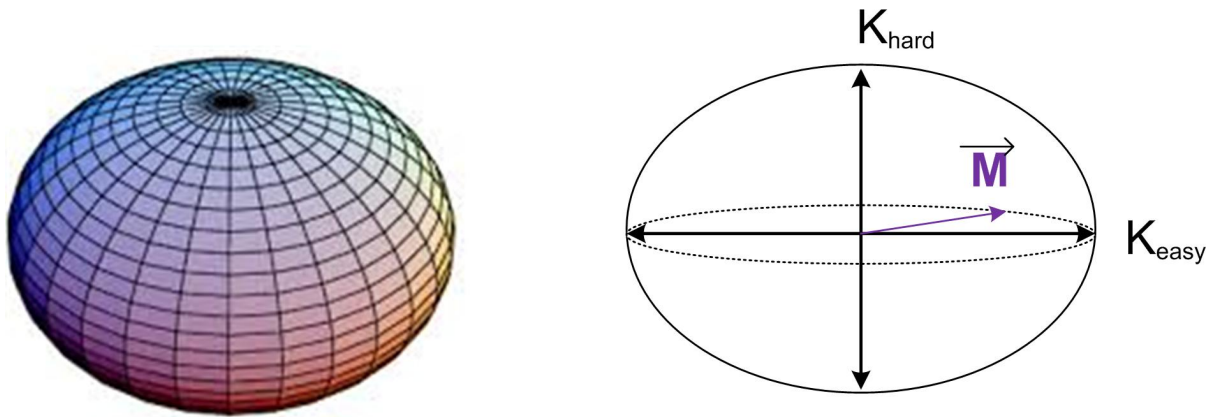


**FIGURE 4-8. "Energy surface" representing the uniaxial anisotropy for a polycrystalline thin film. The axes of the oblate spheroid describe the hard and easy axes of magnetic anisotropy, where the larger axis represents the preferred alignment for magnetization. Thus the uniaxial anisotropy for a thin film generally lies in-plane, and thus magnetization is restricted to this dimensionality.**

When considering a polycrystalline thin film, the anisotropy energy is generally confined to the plane of the film in order to reduce the strong magnetostatic energy associated with the surface. One can simply visualize the anisotropy energy surface for such a system as an oblate spheroid, where the axes are directionals of the uniaxial anisotropy vector $\vec{K}(\vec{r})$, as illustrated in **Figure 4-8**. Thus, with the semi-major axis of the spheroid being the long axis of the energy surface, this axis represents the easy axis of the magnetic system; the magnetization will primarily lie in the $x$–$y$ plane of the sample,

116

with some degeneracy. The degeneracy is thus broken, and magnetization induced, through the interaction of the sample with external forces.

For these experiments, the applied field energy, also known as Zeeman energy, and the magneto-elastic interaction energy are responsible for determining the stable magnetic state since other contributions are relatively small. Thus, the free energy of the system is expressed as:

$$U\left(\vec{M}(\vec{r}),\vec{r}\right) = \left|\vec{K}_{ME}(\vec{r})\right|\sin^2\left(2\pi\hat{M}(\vec{r})\cdot\hat{K}(\vec{r})\right) + \vec{M}(\vec{r})\cdot\vec{H}(\vec{r})$$ **(Equation 4-2)**

where $\left|\vec{K}_{ME}(\vec{r})\right|$ is the magneto-elastic anisotropy energy of the semi-major axis, and

$\hat{K} = \vec{K}_{ME}/\left|\vec{K}_{ME}(\vec{r})\right|$ is the unit vector along the easy axis. The left-hand term represents the magnetoelastic energy term, and the right-hand term represents the Zeeman energy term. To simplify, we define $\phi(\vec{r})$ as the direction of $\hat{M}(\vec{r})$, the vector field of magnetization, and $\theta(\vec{r})$ as the direction of $\hat{K}(\vec{r})$ in the x-y plane, with the assumption $M_z = 0$ and $K_z = 0$. It is also assumed that $\vec{H}(\vec{r}) = H_{appl.}\hat{x}$. With these simplifications, the energy becomes:

$$U(\phi(\vec{r}),\vec{r}) = \left|\vec{K}_{ME}(\vec{r})\right|\sin^2(\phi(\vec{r}) + \theta(\vec{r})) - MH\cos(\phi(\vec{r}))$$ **(Equation 4-3)**

or

$$U(\phi(\vec{r}),\vec{r}) = \eta(\vec{r})\sin^2(\phi(\vec{r}) + \theta(\vec{r})) - \cos(\phi(\vec{r}))$$ **(Equation 4-4)**

where $\eta(\vec{r})$ is the ratio of the magnetoelastic and Zeeman energies. For this heuristic model, we assign an inverse relationship between the magnetoelastic anisotropy and $\vec{r}$ ( $\eta(\vec{r}) \approx 1/\vec{r}$ ), which describes that with large $\vec{r}$ the magnetoelastic anisotropy is small (thus the Zeeman energy dominates) and with small $\vec{r}$ the magnetoelastic anisotropy is large (dominating the energy sum).

The stable magnetization direction $\phi(\vec{r})$ can be found by minimizing the total

energy as $\partial U(\phi(\vec{r}),\vec{r})/\partial\phi = 0$. The values of $\phi(\vec{r})$ for minimized energy are displayed in

**Figure 4-9** as a map of a space parameterized by $\vec{r}$ and $\theta(\vec{r})$; the features of this map are

compared with a Foucault contrast image of the magnetic domains from the experiment.

Generally, the features of the domain structure in this map are similar to those found in

the experiment. Two cardioid domains emerge in the region of small $\vec{r}$ with symmetry

about the direction of uniaxial anisotropy. The domain walls separate two magnetic

domain lobes; the magnetization within these domains displays a strong variance with $\vec{r}$.

The domain walls extend until it reaches a critical distance $\vec{r}_{critical}$ where the two

competing energies are in equilibrium. Beyond this critical point, the Zeeman energy

dominates, the variance with $\vec{r}$ is neglected, and the magnetization follows the anisotropy

of the applied field ($\phi = 0$).
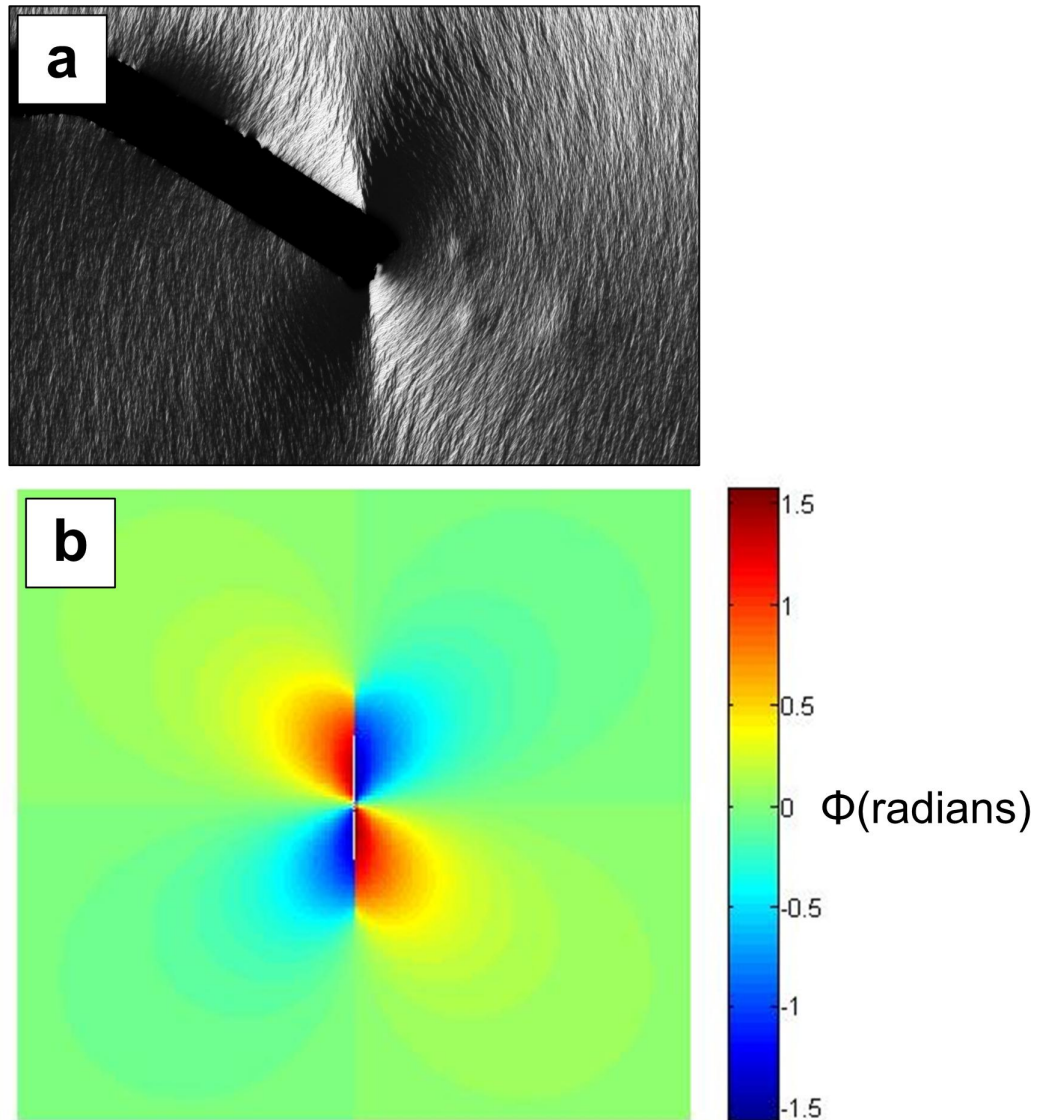
**Figure 4-9. (a) Foucault magnetic contrast of a mechanically loaded field simultaneously experiencing applied field. An aperture in the back-focal plane obscures deflections induced by specific domains. This provides contrast of magnetic domains. (b) A heuristic model of $\phi(\vec{r})$, where the applied stress contributing to the magnetoelastic energy is assumed to take the form $\sigma(\vec{r}) = 1/r$.**

This spatial relationship of $\phi(\vec{r})$ seen in the calculated map is readily observed in the landscape of the energies acting on the system. **Figure 4-10** depicts the form of both contributing energies, and their combined form, against $\phi$. The energy minimum

determines the stable value of $\phi$. In **Figure 4-10 (a)**, the form of the Zeeman energy is minimized at $\phi = \pi$. Thus where energy of the applied dominates $\phi$ assumes this value which is evidenced both in the micrographs and the calculated form of the energy.

The magnetoelastic energy minima as seen in **Figure 4-10 (b)**, support two stable configurations for $\phi$. However $\phi$ also displays dependence on $\theta(\vec{r})$ – the minima vary from $\phi = 0$ to $\phi = \frac{\pi}{2}$ and $\phi = \pi$ to $\phi = \frac{3\pi}{2}$ as $\theta$ varies from 0 to $\frac{\pi}{2}$. Thus, within the region of influence of the magnetoelastic energy, $\phi$ rotates from alignment with the applied field to perpendicular alignment. Since the magnetoelastic energy is determined by the magnetostriction, this 90º rotation is expected, as the symmetry of magnetostrictive anisotropy is unable to do work necessary for 180º rotations [27], [59], [84].

These two energies compete in the system to determine the stable magnetization configuration, and we have thus far seen the spatial dependence of $\eta(\vec{r})$ – the ratio of the two anisotropies– both experimentally and in the model. The combined effect is seen in the three forms depicted in **Figure 4-10 (c)**, representing the three regimes of $\eta(\vec{r})$. For $\eta(\vec{r}) \ll 1$, the minima exist at $\phi = 0$ and $\phi = 2\pi$, thus the magnetization is primarily determined by the applied field energy, which ultimately selects between the two stable values. For $\eta(\vec{r}) \approx 1$, the energy stabilizes at $\phi \sim \frac{\pi}{4}$, approaching the stress induced anisotropy. This represents the critical distance, where $\phi$ is transiting from the stress induced anisotropy, to the applied field anisotropy. For $\eta(\vec{r}) \gg 1$, the combined energy form closely resembles that of the magnetoelastic energy term. Thus the induced stress anisotropy is dominant within this regime, and the anisotropy is stable at $\phi = \frac{\pi}{4}$.

As previously defined, the anisotropy coefficient for the magnetoeleastic energy $\left|\vec{K}_{ME}(\vec{r})\right|$ has an explicit dependence on $\vec{r}$. For magnetostrictive anisotropy energy, this term is expressed as $\frac{3}{2}\lambda_s\sigma(\vec{r})$, where $\lambda_s$ is the coefficient for magnetostriction at saturation, and $\sigma(\vec{r})$ is the applied stress, which introduces the variance with $\vec{r}$. Thus far, we have used an ansatz that $\sigma(\vec{r}) \sim \frac{1}{r}$, which has generally matched the observed competition between the two anisotropies. In order to develop a better model of the applied stress in terms of the mechanical properties of the system, we next turn to mechanics of membrane deflection.
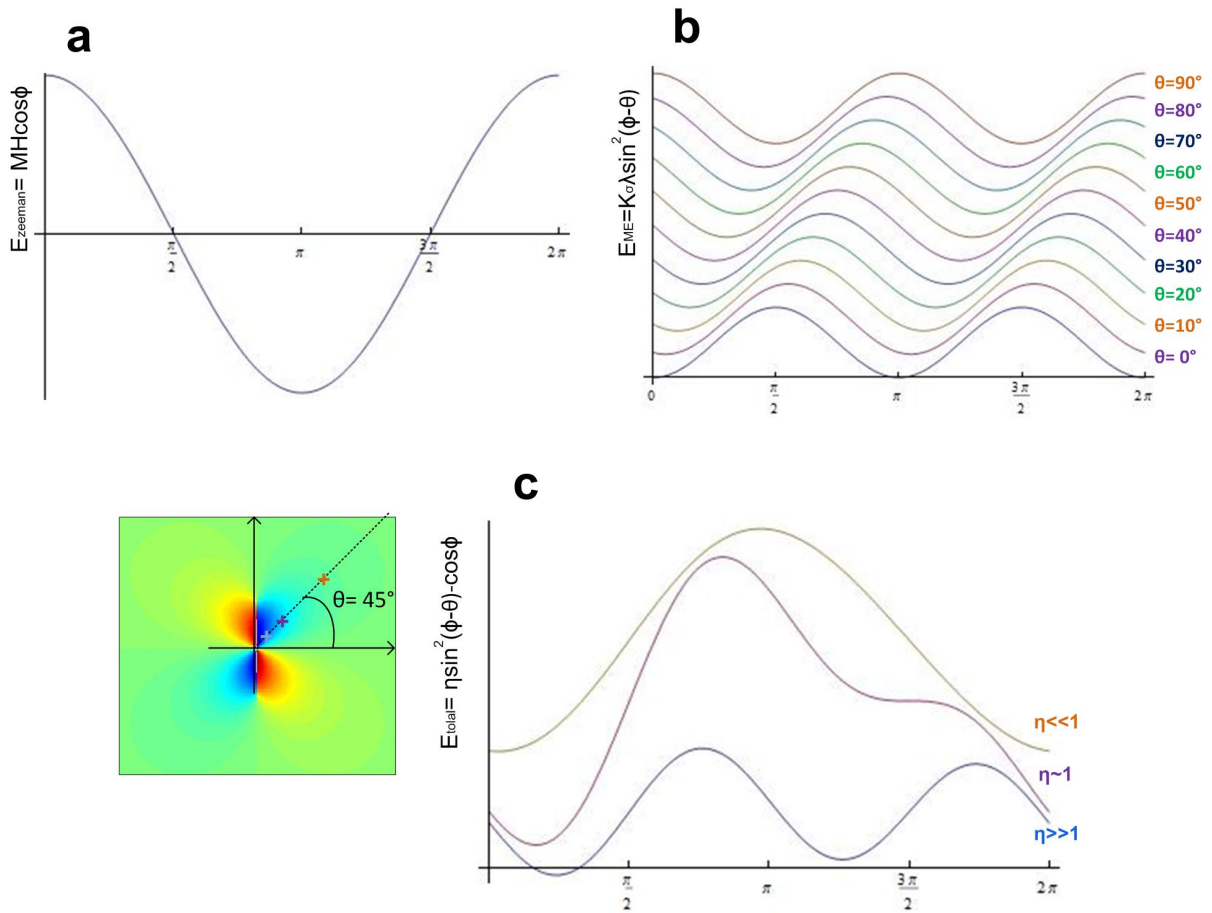
**Figure 4-10.** The "energy landscapes" of both competing energy terms (a) applied (Zeeman) field, (b) magnetoelastic energy, and (c) the combined effects. In (b) the phase of the magnetoelastic energy shifts with increasing $\theta$, thus magnetization rotation angle $\phi$ shifts from $n\pi$ to $(2n-1)\pi/2$. In (c) the energy landscapes represent fixed $\theta=45°$, and the ratio of the anisotropies $\eta$ is varied.

### 4.3.2 Mechanical stress model
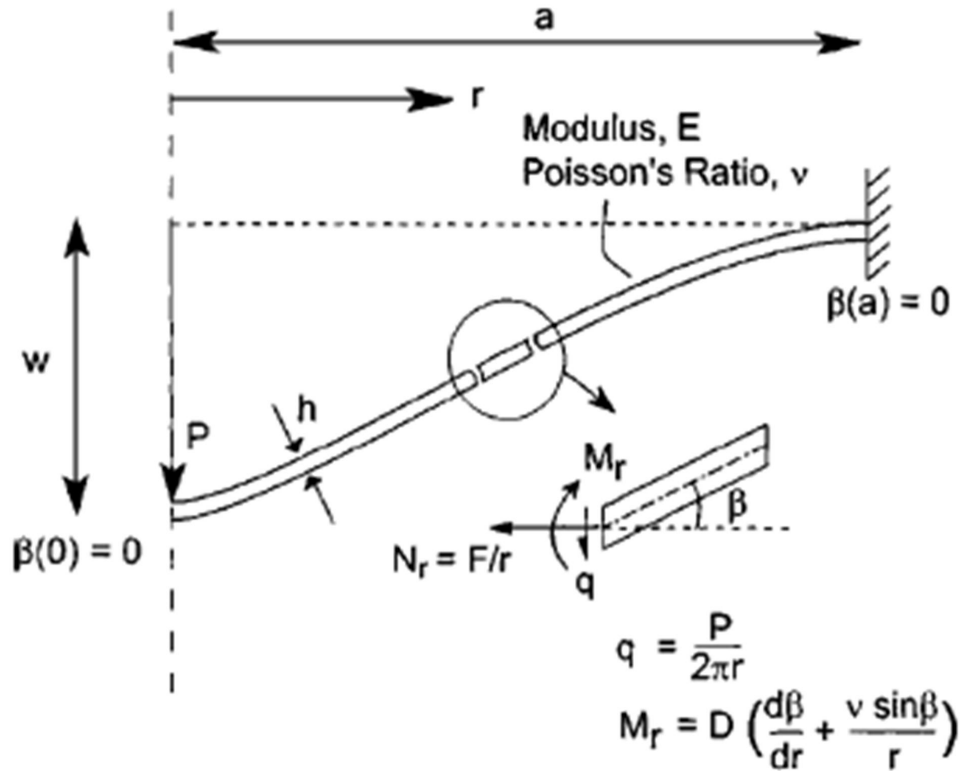


**Figure 4-11. Schematic illustration of the dimensions and variables used in the analysis of a thin circular film subjected to a point load. Taken from** [85]**.**

We seek a model for the mechanics of the *FeGa/SiN* membrane system experiencing transverse loading. Komaragiri et al. have provided a comprehensive description of the mechanical response of freestanding circular elastic films subjected to point-loads in terms of closed-form solutions [85]. Here, we extend the solutions for the membrane behavior to the square plate of our system, with dimensions approximately equal to the circle plate radius. Mechanical response for rectangular films are generally more complex and numerically evaluated, which has been demonstrated by Timoshenko

and Woinowsky-Krieger [86]. **Figure 4-11** shows the relevant dimensions and variables used to describe the film behavior. Small strains are assumed, such that the deformation of the film can be described by the simplified Reissner theory (an example that can be found in [87]). The compatibility and equilibrium equations obtained from the theory are:

$$AL_r F + 2r\sin^2(\beta/2) = 0 \quad \textbf{(Equation 4-5)}$$

and

$$D(L_r \beta + B - \sin\beta) - rF\sin\beta + r^2 q\cos\beta = 0 \quad \textbf{(Equation 4-6)}$$

for, $\{\beta\} \to 0$ and $\beta(a) = 0$

where $\beta$ is the angle of rotation, $F$ is a stress variable ($F = rN_r$, where $N_r$ is the conventional stress resultant in the radial direction). The variable $q$ is the vertical shear stress resultant, and, for a downward point load of magnitude $P$ at the center of the film, $q = P/2\pi r$. In these equations:

$$L_r = r^2\frac{d^2}{dr^2} + r\frac{d}{dr} - 1 \quad \textbf{(Equation 4-7)}$$

represents a homogenous linear differential operator, $D$ is the bending stiffness, and $A$ is the stretching compliance of the film defined as:

$$D = \frac{Eh^3}{12(1-\upsilon^2)} \quad \text{and} \quad A = \frac{1}{Eh} \quad \textbf{(Equations 4-8 and 4-9)}$$

where $E$ is the elastic modulus of the film, $h$ is the film thickness, and $v$ is the film's Poisson ratio. Thus, the extensional strain is given by:

$$\varepsilon_r = A(r^{-1}F\cos\beta + q\sin\beta - \upsilon\frac{dF}{dr}) - \varepsilon_0 \quad \textbf{(Equation 4-10)}$$

where $\varepsilon_0$ is a small positive prestrain caused by residual stresses that occur during the processing of the film. The vertical deflection of the film is defined by:

$$w(r) = \int_r^a \sin\beta(s)\,ds \quad \textbf{(Equation 4-11)}$$

where the deflection of the plate at the edge ($r = a$) is assumed to vanish. These equations are applied to nonlinear Föppl membrane theory, which corresponds to scenarios where bending stiffness is neglible in comparison to the stiffness generated by stretching, attributed to large deflections or small thicknesses. In this regime, membrane behavior dominates the prestretch. The solutions in this regime follow Schwerin's classic solution, yielding:

$$\beta(r) = \left(\frac{8P}{9\pi Ehr}\right)^{1/3} \quad \textbf{(Equation 4-12)}$$

$$F(r) = \frac{P}{2\pi\beta(r)} = \tfrac{3}{4}\left(\frac{P^2 Ehr}{3\pi^2}\right)^{1/3} \quad \textbf{(Equation 4-13)}$$

and

$$\frac{w(0)}{a} = \left(\frac{3P}{\pi Eah}\right)^{1/3} \quad \textbf{(Equation 4-14)}$$

However, this solution satisfies the boundary conditions only for a Poisson's ratio given by $v = 1/3$. For Poisson's ratios other than one-third and zero prestrain, the approximate membrane solution for point loads goes as:

$$\frac{w(0)}{a} = f(v)\left(\frac{P}{Eah}\right)^{1/3} \quad \textbf{(Equation 4-15)}$$

where $f(v) \approx 1.0491 - 0.1462v - 0.15827v^2$.

These solutions were applied to the magnetoelastic anisotropy term, where $\sigma(r) = E \cdot \varepsilon_r$. The mechanical behavior of the system was calculated using material parameters extracted from literature, for the SiN membrane. As this phase of the system is thicker than the FeGa film, the membrane behavior is largely determined by its

properties. Constants and coefficients concerning the magnetostrictive properties of the system were used for the FeGa phase of the system; these have been previously measured for the calculations performed for the FeGa/BTO bilayer device [59].

**Figure 4-12** displays the resulting map of $\phi(\vec{r})$, as determined from minimizing the energy of the system, where the magnetoelastic anisotropy includes the induced stress as calculated from the membrane theory. Many features in this model oppose those found both in experiment and in the original heuristic model. While $\phi$ maintains its variance with $\theta$, $\phi$ no longer displays a strong relationship with $\vec{r}$. According to the membrane theory, the mechanically induced anisotropy is dominant throughout the film, creating 180º domain walls from the top to the bottom of the film. This theory also suggests that the applied stress σ varies little with $\vec{r}$, which is evident in the extension of the domains through to the film edges. This domain structure is prevalent until the onset of the applied field anisotropy, where the entire film becomes uniformly polarized.

Thus, simply extending the heuristic model to include a model of the applied stress supported by mechanical membrane theory does not accurately capture the dynamics of the system. It is possible that magnetostatic interactions generated from the induced anisotropy contribute to the stability of the final domain structure, and such interactions have been excluded from the model thus far. We now turn to a micromagnetic model that is capable of evolving these possible energy interactions.
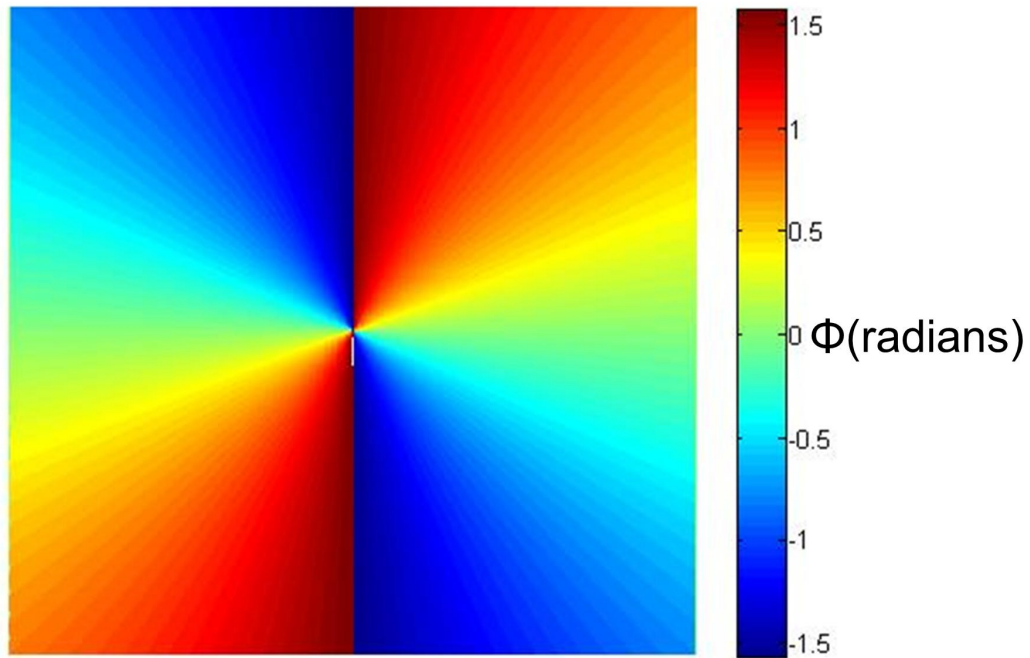
**Figure 4-12. Map of $\phi(\vec{r})$ determined from energy minimization. The stress $\sigma(\vec{r})$ is determined according to theoretical behavior of a plate experiencing central point-loading.**

### 4.3.3 LLG formalism & micromagnetics

Micromagnetism is the continuum theory of magnetic moments. It neglects the quantum-physical description of matter by ignoring its atomic nature, and instead assumes continuum physics for a classical magnetization vector field [25], [27], [84]. Such a theory began with Landau and Lifshitz, who in 1935 calculated the structure of a domain wall between two adjacent antiparallel domains. Their formulation is the starting point of any dynamic description of micromagnetic processes. It describes the precession of the magnetization around the effective field, or in other words, the gyroscopic nature of magnetization dynamics. The formulation is represented as:

$$\frac{\partial \vec{M}}{dt} = -\gamma\left(\vec{M} \times \vec{H}\right) - \lambda \frac{\vec{M} \times (\vec{M} \times \vec{H})}{M^2} \quad \textbf{(Equation 4-16)}$$

The first term describes the precession motion, and the second term introduces damping (which corresponds to local and quasi-local energy losses of the magnetization in the continuum), where for the time being, λ is an adjustable damping parameter. The constant $\gamma_G = ge/2mc$, where $e$ and $m$ are the charge and mass of the electron, $c$ is the speed of light, and $g$ is the spectroscopic splitting factor ($= 2$ for electron spin). The damping term allows the magnetization to align with the effective field until both vectors are parallel in the static solution. An alternative damping term was proposed by Gilbert:

$$-\frac{\alpha}{M}\left(\vec{M} \times \frac{d\vec{M}}{dt}\right), \quad \text{where} \quad \alpha = \frac{\lambda}{\gamma_G M} \quad \textbf{(Equation 4-17)}$$

This modification better represents the behavior of ferromagnets when the damping is large. Thus, the Landau-Lifshitz equation can be rewritten as the Landau-Lifshitz-Gilbert equation:

$$\frac{\partial \vec{M}}{\partial t} = \gamma_G\left(\vec{M} \times \vec{H}\right) - \frac{\alpha}{M}\left(\vec{M} \times \frac{d\vec{M}}{dt}\right) + \gamma_G \alpha^2\left(\vec{M} \times \vec{H}\right) \quad \textbf{(Equation 4-18)}$$

Later, William F. Brown Jr. developed a theory called micromagnetism. Here, we allow $\vec{M}$ to have a direction, which is a continuous function of its position $\vec{r}$ in the crystal. The various energies of the system (exchange, anisotropy, magnetostatic, etc.) are then expressed in terms of these directions throughout the crystal. The micromagnetic equations are derived by minimization of the total free energy with respect to the unit vector field $M(\vec{r})$ using variational calculus– thus describing the equilibrium state at

every point, versus the global interpretation of domain theory.

The micromagnetic equations associated with this class of analysis are complicated and generally non-linear and non-local, and therefore are difficult to solve analytically. Thus, micromagnetic simulations of a ferromagnetic material system are generally performed with micromagnetic solvers which solve these equations numerically and with appropriate boundary conditions. We use the object-oriented micromagnetic framework (OOMMF), a public domain micromagnetics program developed by Michael Donahue and Don Porter at the National Institute of Standards and Technology [88]. It includes a problem editor, a 2D micromagnetic solver, and a magnetization file display program. It utilizes a Landau-Lifshitz ODE solver to relax 3D spins on a 2D mesh of square cells, using FFTs to compute the self-magnetostatic field. Anisotropy, applied field, and initial magnetization can be varied pointwise and arbitrarily shaped elements can be modeled.

We model a *250 μm x 250 μm*, *20 nm* thick FeGa film using saturation magnetization $M_S = 1.360 \times 10^4$ *A/m*, and exchange stiffness *A = 0 J/m*. A Zeeman (applied) field of *80 G* along +X is initialized and maintained through the course of the evolution of the domain structure. The areal dimensions for the model have been reduced in order to accommodate reasonable computation time on conventional processing machines. The cell size is one-thousandth of the sample size, which is relatively large for consideration of the exchange interaction (generally A= $1.4 \times 10^{-11}$ J/m). At this scale the exchange interaction can thus be neglected, which we have done. However, model size reduction can enhance other energies (such as demagnetization and stray fields) that would minimally contribute to the dynamics of the system in practice. For this reason, the

edge field for our sample geometry is first solved, and then removed from further iterations of the solver. In this manner, the model captures the dynamics of a continuous film, and not limited by the boundary conditions of its areal geometry.

The OOMMF program is unable to specify magnetoelastic anisotropy or energy, thus these interactions are generally excluded from simulations performed with this program. Furthermore, the stress-induced anisotropy is spatially non-uniform, which is also unable to be specified in the input file. We instead express the induced anisotropy as a uniaxial anisotropy, which is externally generated and referenced in the magnetization input file. In this manner we are able to incorporate the spatially varying stress anisotropy in accordance with membrane theory.
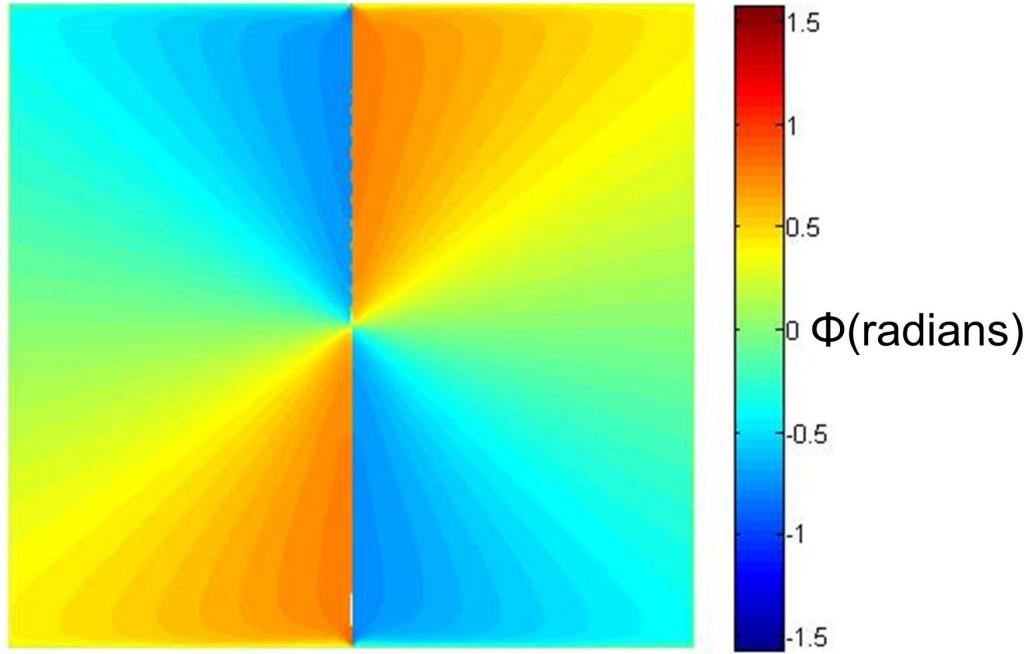
**Figure 4-13. Map of $\phi(\vec{r})$ determined from energy minimization using the OOMMF solver. The stress $\sigma(\vec{r})$ is determined according to theoretical behavior of a plate experiencing central point-loading.**

Our model initiates with a single domain FeGa thin film with the previously specified geometry, external field, and material parameters. The induced magnetoelastic anisotropy is specified in the model as an imported anisotropy vector field file, which defines the applied stress in accordance with **Equation 4-10** where *a = 2.5 x 10^{-4} m* (film radius), *h = 1.0693 x 10^{-7} m* (film thickness as measured with ellipsometry), *E = 2.85 x 10^{11} N/m^2* (Young's modulus of low stress SiN [89]), *v = 0.23* (Poisson's ratio of low stress SiN [89]), *$w_0$ = 1.1 x 10^{-5} m* (maximum center deflection), *$\varepsilon_0$ = 3.20 x 10^8 N/m^2* (low stress SiN prestrain [90], [91]), *$\mu$ = 3.1 H/m* (permeability of FeGa [92]). Thus the magnetoelastic energy takes the form $E_{ME} = \gamma_\sigma \frac{3}{2} \lambda \sigma_{theo.}(\vec{r}) \sin^2(\phi - \theta)$. Here $\gamma_\sigma$ is a scaling

term introduced to scale the effect of the magnetoelastic energy relative to the Zeeman

energy term. While the physical basis for this term is not yet established, it serves as an

empirical factor that scales the effect of the magnetoelastic energy to accurately capture

the effect of stress on the observed magnetomechanical behavior. Once the

demagnetization edge field has been calculated and removed from subsequent iterations,

the evolver proceeds to minimize the energy of the system and display the most probable

resulting magnetostatic state.

**Figure 4-13** depicts the final magnetization state in terms of the magnetization

angle $\phi$ with $\sigma(\vec{r})$ defined by plate theory. $E_{ME}$ is scaled such that the 45º domain angles

that are prominent in the measured magnetic structure (see *Figure 4-7 (b))* are present,

and to effectively scale the two energy terms relative to one another. Once again, the

domain shape opposes that which was captured in the Fresnel contrast images, which

suggests σ has little variance with $\vec{r}$ . In the mode, the induced anisotropy is present

through the entire freestanding film, which contradicts the experimentally witnessed

domain structure.  Thus, it appears that simple linear scaling of the two energy terms does

not adequately describe their interaction. From here, we look to other models to capture

magnetomechanical behavior.

### 4.3.4 Threshold model
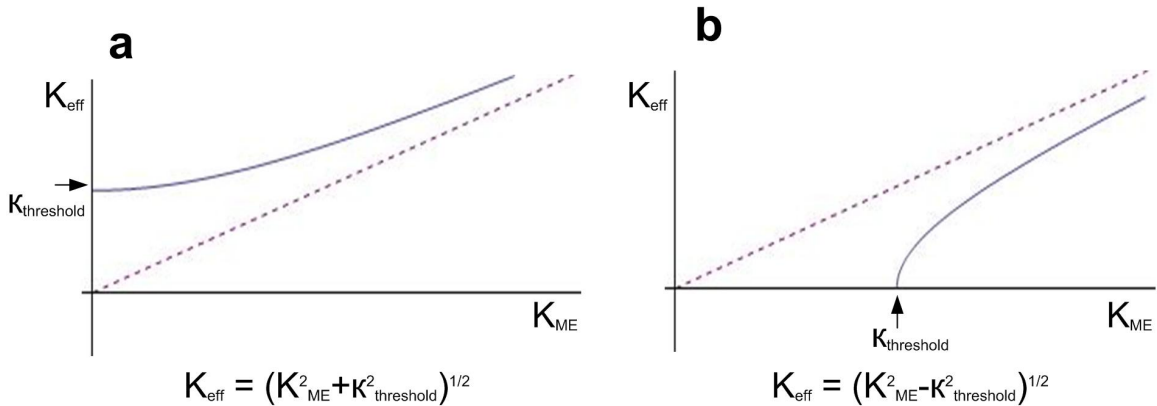


Figure 4-14. Functional forms representing a threshold for anisotropy onset. (a) the practice of adding unassociated terms in quadrature is common, however it does not describe the sudden onset of magnetoelastic effects in the system. (b) Rather subtracting in quadrature creates a threshold barrier where magnetoelastic effects are realized. The dashed line represents a linear relationship between the effective and magnetoelastic anisotropies.

For our experiments it is clear that there is competition between the two anisotropy terms (see **Figures 4-1 and 4-3**), and the heuristic model has proven to be useful in order to show the balance in the relationship between the competing energies. The magnetoelastic effects on the anisotropy extend through to a critical point in the film, and this point is determined by the strength of the applied field. The magnetoelastic effects are only realized when the applied stress is strong enough to overcome the anisotropy introduced by the external field and the local domain ripple. Thus, this presents an anisotropy threshold where the onset of the magnetoelastic effects becomes evident in the effective anisotropy of the film in overcoming a threshold barrier. Therefore, the effective anisotropy depends on the strength of the stress-induced anisotropy relative to the onset threshold.

It is a common practice in simple error analysis to add in quadrature the independent uncertainties of measured quantities that are added or subtracted, and this

behavior is shown in **Figure 4-14 (a)**. Here the effective anisotropy is determined by adding in quadrature the anisotropy due to magnetoelastic effects and an anisotropy barrier $K_{threshold}$. However, in associating the anisotropies in this manner the effective anisotropy is largely determined by the magnetoelastic effect, even at small values of applied stress. This is not the behavior that has been observed experimentally and does not describe the magnetoelastic onset.

A function that describes this sort of behavior is depicted in **Figure 4-14** (b) where the effective anisotropy is determined by the induced anisotropy subtracted in quadrature with the barrier anisotropy, represented as $K_{eff} = \left( K_{ME}^2 - K_{threshold}^2 \right)^{\frac{1}{2}}$. In this manner magnetoelastic effects are not realized until $K_{ME} > K_{threshold}$; when $K_{ME} >> K_{threshold}$, the effective anisotropy is largely determined by the induced anisotropy, and the relationship scales nearly linearly (as indicated by the dashed line in **Figure 4-14**). While this model accurately captures the empirical magnetomechanical behavior of the system, a physical significance of this behavior has yet to be determined. Nevertheless, the threshold model offers convincing insight toward the interaction of the two energy terms, which are presented next.
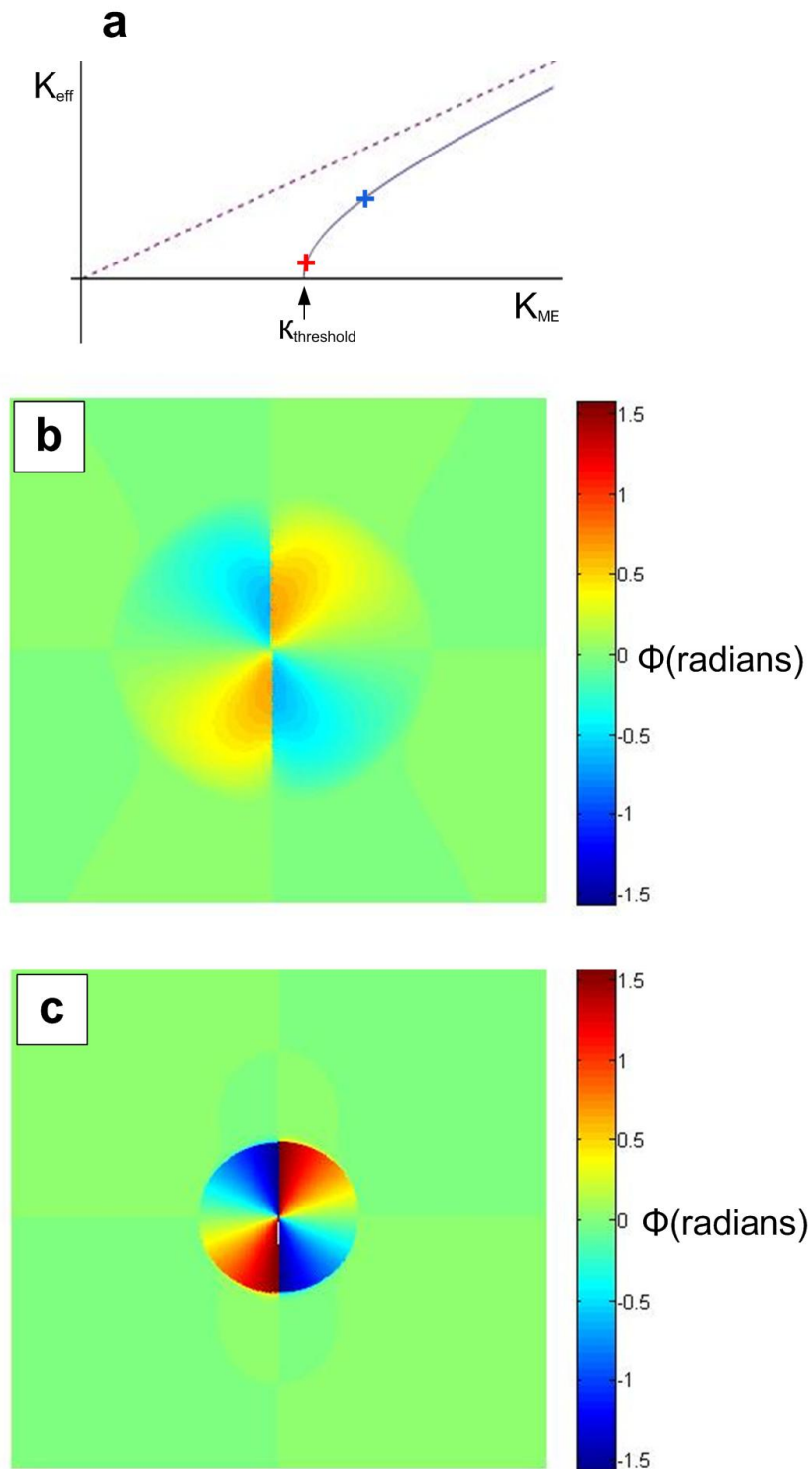
**Figure 4-15. Map of $\phi(\vec{r})$ determined from energy minimization using the OOMMF solver. The stress $\sigma(\vec{r})$ is determined according to theoretical behavior of a plate experiencing central point-loading with an imposed threshold condition for the onset of magnetoelastic effects. The strength of the magnetoelastic effect is scaled for (a) weak and (b) strong post-onset effect.**

The threshold model places a condition on the effective anisotropy that is input to the OOMMF solver. The onset of magnetoelastic effects depends on the anisotropy of the film, when the anisotropy is small the barrier is also small, and vice versa. In our experiments, the film anisotropy can be mediated with external field. Thus, we first specify the threshold as a product of the saturation magnetization and the applied external field, represented as $K_{threshold} = \mu_0 M_S H$. This threshold condition is then imposed on the anisotropy inputs for the OOMF solver. When the applied anisotropy is smaller than the threshold, the effective anisotropy is determined by the unipolar anisotropy imposed by the external field. However, when the applied anisotropy is greater than the threshold, the effective anisotropy is determined as

$$K_{eff} = \gamma_\sigma \left( K_{ME}^2 - K_{threshold}^2 \right)^{\frac{1}{2}} \quad \textbf{(Equation 4-19)}$$

where again $\gamma_\sigma$ scales the strength of the effect, and $K_{ME}$ follows the plate theory.

**Figure 4-15 (a)** displays the result of imposing a threshold condition on the effective anisotropy. Here, reasonable values for the strength scale and threshold were chosen, such that the effective anisotropy is defined as early onset magnetoelastic effects. The resulting domain structure mimics the cardioid 45° domain structure captured in the experiment. This model successfully captures the local variance of the applied stress with both $\theta$ and $\vec{r}$, and maintains the critical equilibrium of the competing anisotropies out toward critical distance.

In **Figure 4-15 (b)** the applied anisotropy is scaled such that the formation of 180° domain walls separate the magnetic lobes of the cardioid, and locally, the effective stress is predominantly defined by the applied anisotropy. Thus with strong applied stress, the

local variance of the anisotropy with $\bar{r}$ reduces and the effective anisotropy approaches a linear relationship with the applied anisotropy.

*4.3.5 Ripple anisotropy & Mechanical hysteresis (Pure stress results)*
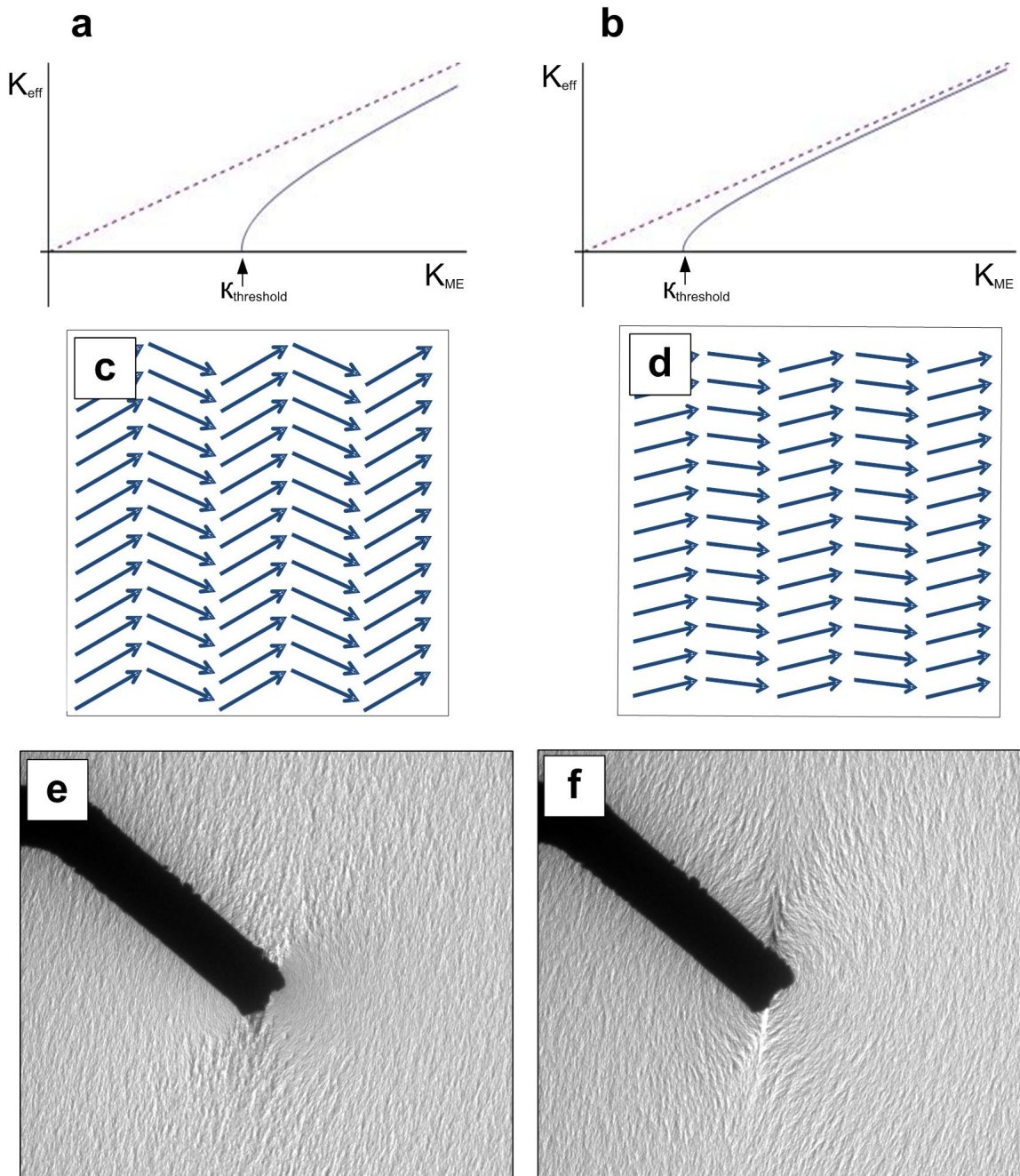


**Figure 4-16. (a)–(b)Threshold manipulation mediates the relative strength of the magnetoelastic effects. This is most readily achieved through manipulating the uniaxial anisotropy of the film, which is probed via the ripple texture. High threshold is a result of (c) low anisotropy, and low threshold is a result of (d) high anisotropy. The effect of the threshold is observed for both (e) low and (f) high anisotropy cases, where pure stress effects have smaller impact on the effective anisotropy, and applied field assists the onset of magnetoelastic influences.**

The threshold model we present in the prior section places implications on the final domain structure; especially for pure stress effects on the effective anisotropy. As previously stated, the onset of magnetoelastic effects depends on the anisotropy of the film. When the anisotropy is small the threshold barrier is also small, and vice versa. The uniaxial anisotropy is modified with applied field, which is evidenced experimentally with changes in the magnetization ripple wavelength as dictated by **Equation 4-1**. **Figure 4-16** depicts the dependency of the threshold, and thus the effective anisotropy due to applied stress, on the uniaxial anisotropy of the film. As previously described and witnessed, polycrystalline thin films display ripple texture which is present due to the slow variation of the uniaxial anisotropy about the net magnetization. Films with reduced uniaxial anisotropy generally show coarse ripple texture in Fresnel images. With the application of external field, the magnetization becomes increasingly aligned with the field direction. The ripple wavelength is reduced, and film assumes a larger uniaxial anisotropy.

This relationship is roughly depicted in **Figure 4-16 (c)** and **(d)**, which represent low anisotropy, coarse ripple texture, and high anisotropy, fine ripple texture, respectively. Low anisotropy films display higher threshold, as shown in **Figure 4-16 (a)**. Thus this requires relatively strong applied stress in order to realize magnetoelastic effects. The micrograph in frame **(e)** represents a film with no field hysteresis, and is mechanically loaded (as previously described in the case for pure stress effects). In the resulting domain structure, we see that the magnetoelastic effects are reduced when compared to the effects displayed in a film that has experienced both applied stress and field (as seen in **Figure 4-16 (f)** where the domains are larger and have increased

magnetization). Increasing the field reduces the threshold, thus an applied anisotropy of equal scale has a larger influence on the effective anisotropy in a film under high field versus a film under low field conditions. Thus, this model successfully explains the discrepancies between the domain structure depending on its hysteresis with applied field and stress, though a physical basis for the threshold barrier remains unknown.

# Chapter 5: Conclusions & Outlook

## *5.1 Mechanical threshold*

### *5.1.1 Field effects*

Multiferroic materials present a unique opportunity to realize coupling between two or more ferroic phases. This feature has reenergized research of these materials as magnetoelectric coupling applied to magnetic-RAM (MRAM) devices would be a gain in reducing power demands, as well as reading and writing speeds of current market mainstays. Magnetoelectric materials and their constituent material phases, have been challenging to effectively characterize. Therefore, the direct association of external stimuli is a powerful probing method for understanding the association of electrical, magnetic, or elastic responses inherent to a material system, particularly in efforts to understanding the interaction mechanism.

Characterization of a bilayer, heterostructure, magnetoelectric device was demonstrated where the ferromagnetic response in magnetostrictive FeGa thin films was directly associated with a range of applied electric field using Lorentz TEM magnetic imaging techniques (see **Figures 2-26 – 2-29**). It was observed that *~7–11 MV/m* electric fields applied to the piezoelectric $BaTiO_3$ film induced local magnetic ordering in regions of 90º domains in the FeGa, reporting an induced magnetostrictive anisotropy of *25 kPa* via strain. This mechanism was applied to a MRAM concept technology, where micromagnetic modeling of the effect in individually patterned magnetic nodes (with

141

relevant dimensions for maintaining high bit density) demonstrated the reduction of the coercivity of each node. Thus, requiring smaller external fields for writing, and as a result, substantially reducing the power demands of conventional MRAM technologies. However, moving the technology forward requires better local control of the effects, and we have explored improving magneto-response locally through direct mechanical interaction with magnetostrictive materials via non-uniform strains.

In situ methods for characterizing magneto-response systems offer significant quantitative information of the system interactions through probing mechanisms at smaller scales, and thus allow for fine-tuning of the effect at smaller scales. In this work we have presented various experimental accounts of magnetomechanical effects in magnetostrictive FeGa thin films deposited on freestanding, flexible $Si_3N_4$ substrates. Here, we have combined nanomanipulation instrumentation along with Lorentz-force TEM magnetic imaging techniques for in situ insight towards the interactions of the magnetostrictive thin film with external field and mechanical stimuli. In this experimental setup a 25 $\mu m$ wire was used to mechanically load the film at the center of the window, and small excitations to the objective electromagnetic lens exposed the specimen to fields as large as 160 $G$.

With both Fresnel and Foucault magnetic imaging techniques, magnetic ordering in response to simultaneous field and stress external parameters was observed. The non-uniformity and radial symmetry due to the nature of the point-load induced stress generated radial magnetic order about the point of contact. Fresnel contrast captured domain walls separating the two primary domains formed in the process, while Foucault

contrast captured the domain structure as a symmetric cardioid within 50 $\mu m$ of the deflecting tip.

Magnetic ripple texture present in Fresnel contrast images served as an orthogonal map of local magnetic order, and was used to characterize the induced magnetization in terms of its rotation angle $\phi$ with respect to its radial position $\theta(\vec{r})$ about tip. The stress and field induced magnetic domains are primarily characterized as 45° domains, but the magnetization rotation is observed to vary with $\vec{r}$ and in some regions approached 180° (especially in vicinity of the domain walls). Hysteresis with both field and stress chart the interaction of two competing energies of the film: stress induced magnetoelastic energy, and field induced Zeeman energy (see **Figure 4-3**).

These energy terms capture the magneto-mechanical interactions of the system and their competition is evident in radial magnetic order about the probe. The extent of the induced magnetoelastic anisotropy is evidenced by changes in the ripple texture, and also in the length of the domain wall. The termination of the domain wall marks an equilibrium in the strengths of the two energy terms, and beyond this point the magnetization is dictated by the applied field.

Heuristic modeling of the interaction (where $\sigma(\vec{r}) = 1/r$) successfully captured the interaction of the two competing energies as the local effect of the magnetoelastic anisotropy gradually declines (see **Figure 4-9**). However, in expanding this model to include the theoretical mechanics of a thin plate experiencing point-load deflection, the interaction of the two energy terms proved to be more complex as the competition between the two terms no longer displayed strong spatial dependence (see **Figures 4-12** and **4-13**). Ultimately, the empirical magnetoelastic effects are described through

imposing a threshold barrier (in which the effective anisotropy is expressed by subtracting the anisotropy strength of the induced stress and barrier in quadrature) for the onset of the behavior. Thus the realization of magnetoelastic effects depends not only on the strength scale of the effect, but also on the initial anisotropy of the thin film.

The threshold model thus places strict limitations on realizing magnetoelastic effects in a pure stress environment. The domain structure of the film with hysteresis solely due to applied stress lacked high magnetization rotation angles, and thus lacked sharp transitions between domains (see **Figure 4-1**). The threshold model suggests that for a given applied stress, the resulting domain structure is determined by its strength relative to the threshold. Thus the discrepancy in the domain structure between the film experiencing both field and stress, and the film experiencing stress alone, lies in the difference in ripple anisotropy, where high ripple texture corresponds to high threshold and low ripple texture corresponds to low threshold.

As polycrystalline films consist of individual grains, the inter- and intra-granular interactions ultimately determine the uniaxial anisotropy of the overall film. As seen in the Fresnel contrast images, magnetization ripple is a direct effect of the magnetostatic intergranular interactions and magnetization variation throughout the film, and the ripple wavelength varies inversely with uniaxial anisotropy. Coarser ripple texture is seen in the Fresnel images of the film in the absence of external field, which thus suggests weaker anisotropy; when applying an external field, stronger anisotropy is induced and finer ripple texture is observed. Thus, by moderating the ripple anisotropy of the film, the external field assisted in lowering the threshold barrier, thereby allowing for the

144

realization of stronger magnetoelastic effects compared to those observed with the use of applied stress alone.

It was demonstrated that by scaling the strength of the magnetoelastic effect, stronger magnetization rotations could be achieved where full 90º rotations are possible within the induced domain. Herein lies a unique application of magnetoelastic effects in magnetostrictive systems for MRAM device implementation. It has been emphasized that magnetization achieved via inverse magnetostriction is invariant to distinguished 180º rotations due to the symmetry inherent to the effect; the magnetostrictive effect can only produce a force on a 90º domain wall. Here, owing to the radial symmetry of the induced strain in the film, two adjacent, opposing 90º rotations occur. The final state of each domain is thus out of phase by 180º. In other words, though magnetostriction does not inherently demonstrate 180º rotations, two distinct 180º states can be achieved with radial, non-uniform applied stress.

### 5.1.2 Quantification of threshold

In order to guarantee strong magnetoelastic effects, it is important to understand the requirements of the system to overcome the threshold barrier. It has been previously demonstrated that the threshold is effectively moderated with modifications to the ripple anisotropy (**Figure 4-16**), which has been achieved here with application of external field. While the physical origins of the threshold remain unknown, it is clear that the threshold barrier (which is related to the ripple anisotropy) can be represented as an unknown function of applied field, with $\kappa_{thresh}\left(\vec{H}\right)$. Given that large ripple anisotropy (coarse ripple texture) is present in zero-field conditions, we expect $\kappa_{thresh}\left(0\right)$ to be

comparatively larger than $\kappa_{thresh}\left(\vec{H}\right)$, where $\vec{H}_1$ is any given applied field. In **Figure 4-15**, two strength scales of the threshold are presented for applied fields $\vec{H}_1$ and $\vec{H}_2$, with the former representing the weaker effect and the latter representing the stronger effect. The empirical map of $\phi(\vec{r})$, measured manually from the Fresnel images consists mostly of rotations $\phi = 45^o$, however larger rotations are also present, especially in regions closest to the tip. Nonetheless, the empirical map is best described by the map of $\phi(\vec{r})$ based on the threshold $\kappa_{thresh}\left(\vec{H}\right)$, and for this model $\kappa_{thresh}\left(\vec{H}_1\right) = 60.639 \ kPa$ where $\vec{H}_1 = 160 \ G$. In the case of pure stress effects, the film is mechanically loaded in the absence of applied field; in matching the model to the observed effects the calculated barrier is given as $\kappa_{thresh}(0) = 75.799 \ kPa$, a difference of $\sim 15 \ kPa$ from the model describing lower ripple anisotropy. This describes the anisotropy reduction necessary to observe strong magnetoelastic effects in films exclusively with stress hysteresis.

### 5.1.3 Methods to possibly reduce threshold

In order to achieve stronger magnetoelastic effects, it is necessary to reduce the threshold barrier, which involves reducing the ripple anisotropy. This is best achieved with epitaxial growth of single crystal thin films, which conventionally exhibit high uniaxial anisotropy. Polycrystalline films are composed of individual grains with inter-granular variability in the uniaxial anisotropy; thus the anisotropy in polycrystalline materials is typically reduced when compared to single crystal materials. Furthermore, the variation in granular order can complicate the effect of stress as the magnetostrictive properties depend on an averaging of the effect in individual crystals. Generally, the

stress is considered to vary grain-to-grain. Thus, a single crystalline thin film negates both of these concerns.

However, this solution is not as industrially applicable if such a mechanism is to be applied to market devices. Polycrystalline films are generally inexpensive to engineer, and offer facile fabrication techniques. For this reason, there is an industry preference for polycrystalline films where possible. It is therefore important to consider ways to induce anisotropy in thin films, and minimize the inter-granular variations that cause high magnetization ripple anisotropy. A uniaxial anisotropy can often be produced in magnetic thin films if the deposition is carried out in the presence of an applied magnetic field, where the easy axis follows the direction of the applied field. In this manner, it is possible to obtain uniaxial anisotropy constants similar to those achieved in treated bulk specimens.

In addition to this method, another possible arrangement to achieve strong uniaxial anisotropy is to employ an exchange bias mechanism. Exchange bias describes the shifting of the magnetic hysteresis loop. This effect is caused by the interfacial exchange coupling between a ferromagnet and an antiferromagnet, where the competition for magnetic order results in the creation of an exchange bias field. This effect is widely used to stabilize the magnetization of magnetic layers in spin-valve structures for giant magnetoresistance (GMR) and tunneling magnetoresistance (TMR) sensors. The use of this mechanism to engineer anisotropy and suppress magnetization ripple has previously been demonstrated [82], [93]–[96]. Thus with two possible methods to reduce the magnetization ripple, future work can help determine the form of the threshold and achieve stronger magnetoelastic effects in the film.

## 5.2 Patterned Specimens

It has been previously discussed that patterned media for magnetic data storage can help to achieve the desired bit densities for future MRAM devices. For magnetoelectric structures, proposals for novel MRAM technologies have involved patterned structures at the nanoscale [22], [59], [97]. We have presented our initial efforts toward testing the direct mechanical interaction mechanism on prototype-patterned media, which consisted of a *500 μm x 500 μm* array of *500 nm x 500 nm* lithographically patterned FeGa squares.

The magnetic order is inferred from Foucault magnetic contrast of the edge field respective to each individual element. Currently, the dimensions of the patterned squares have been reduced to *300 nm x 300 nm* and *200 nm x 200 nm* in an effort to achieve a single domain state in each element. Though reduced dimension arrays have been produced, they have not yet been magnetically or mechanically characterized. Thus future experimentation will involve the magnetic characterization of patterned specimens, and subsequent in situ mechanical interaction. Here, the ultimate goal is to demonstrate the direct control of magnetoelastic effects on patterned media, and thus understand an improved means to control magnetization dynamics at smaller scales.

The free energy for magnetic media with reduced dimensions must be reevaluated for modeling as the shape anisotropy is increased with size limitations and thus competes with the magnetoelastic effects. The shape anisotropy energy is described by the relation:

$$E_{shape} = K_u \sin^2 \phi \quad \textbf{(Equation 5-1)}$$

where $K_u = (N_x - N_y)/2M^2$ is the shape anisotropy constant, $N_x$ and $N_y$ are, respectively, the demagnetization factors parallel and perpendicular to the long axis of the element.

The minimum of the shape anisotropy energy corresponds to the magnetization vector lying along the long axis of the element. Thus the magnetoelastic effects must compete with the strengthened energy in order to rotate the magnetization ±90º from the long axis of the element.

Strategic placement of the mechanical loading tip about the patterned array can induce local magnetic rotations within individual elements for an MRAM device without the use of external magnetic fields. We have previously seen that with reduced ripple anisotropy (lower threshold) strong magnetoelastic effects can induce ±90º rotations, and thus effectively creating relative ±180º magnetization states. Tip placement in the vicinity of magnetic elements dictates the rotation with the non-uniform nature of the stress field. Mechanical 'writing' was previously demonstrated in the continuous FeGa thin film (**Figure 4-6**), and has also been reported by Lu et al. in ferroelectric media through flexoelectric biasing [98]. Thus these methods demonstrate unique alternatives to achieving bit stability in RAM devices without the need of power hungry polarizing fields.

## *5.3 Outlook and future work*

### *5.3.1 Future modeling of the threshold effect*

OOMMF simulations do not account for local disorder in the magnetic character of a given structure. The threshold model has been representative of the impact of these variations present in our specimen, and has provided quantitative insight in the strength of the ripple anisotropy. Future work toward exploring the threshold effect, and the effect of magnetization ripple characteristic of polycrystalline materials, will be in including

these inter-granular variations and defining the minimum of ripple anisotropy that may lead to enhanced magnetoelastic effects. Future modeling will also address the implications of strong shape anisotropy for the case of patterned media; a mask representing the geometry of the array can be specified in OOMMF simulations.

The mechanical response of freestanding membranes described in section 4.3.2 was sourced from a comprehensive treatment of circular elastic thin films. Circular film geometries simplify the analysis, where the axisymmetry allows for closed form solutions. However, this symmetry is not present in our system, and thus the solutions must be obtained in terms of a series expansion. Linear response to center point-load have been described by Timoshenko and Woinowsky-Krieger– this analysis may require numerical solutions to the induced extensional strain [86]. Future modeling should address the altered mechanical form as a result of these boundary conditions.

### 5.3.2 Quantification of threshold

While the physical basis for the threshold remains unknown, the functional form of the threshold can be obtained with additional collection of $\kappa(\vec{H})$ data points. The experiment begins in zero-field conditions with the film mechanically loaded. With incremental increases in the external field, magnetoelastic effects become more pronounced as the ripple anisotropy decreases and simultaneously the extent of the effect is moderated in the same manner.

Quantification of the threshold is also possible with quantitative analysis of the ripple wavelength. The relationship between ripple wavelength and uniaxial anisotropy has been previously presented (**Figure 4.4** and **Equation 4.1**). Here, it has been

demonstrated that ripple wavelength can be effectively measured with FFT analysis of Fresnel contrast images, and thus the local uniaxial anisotropy of the specimen can be obtained.

### 5.3.3 Methods to possibly reduce threshold

It has been proposed that reducing ripple anisotropy in the FeGa thin films is possible via single crystalline epitaxial growth of thin films, inducing uniaxial anisotropy in polycrystalline films with field application during deposition, or suppressing ripple using an exchange bias mechanism/structure. Polycrystalline materials are ubiquitous in industrially produced devices, and have been an essential feature in top leading MRAM technologies such as longitudinal and perpendicular recording schemes in HDDs. If this trend is to continue and become applicable in magnetoelectric to magnetoelastic devices, the impact of polycrystalline structure on the overall device performance must be optimized.

This work has demonstrated a means to directly control magnetization through the sole usage of applied stress, and furthermore has demonstrated how a non-uniform stress can achieve stable ±180º magnetization states, which are the cornerstone of current successful magnetic memory mechanisms and a core feature for binary logic architectures. Strain engineering in magnetoelastic and magnetoelectric systems has proven beneficial in overcoming the symmetry limitations that accompany inverse magnetostriction, and thus, in structures such as strain-mediated magnetoelectric bilayers, it is possible to realize local control of the effects in ways necessary to contribute to MRAM technologies.

# References

[1]     S. H. Kang and K. Lee, "Emerging materials and devices in spintronic integrated circuits for energy-smart mobile computing and connectivity," *Acta Mater.*, vol. 61, no. 3, pp. 952–973, Feb. 2013.

[2]     D. I. Khomskii, "Multiferroics: Different ways to combine magnetism and ferroelectricity," *J. Magn. Magn. Mater.*, vol. 306, no. 1, pp. 1–8, Nov. 2006.

[3]     L. W. Martin, S. P. Crane, Y.-H. Chu, M. B. Holcomb, M. Gajek, M. Huijben, C.-H. Yang, N. Balke, and R. Ramesh, "Multiferroics and magnetoelectrics: thin films and nanostructures," *J. Phys. Condens. Matter*, vol. 20, no. 43, p. 434220, Oct. 2008.

[4]     R. Ramesh and N. A. Spaldin, "Multiferroics: progress and prospects in thin films.," *Nat. Mater.*, vol. 6, no. 1, pp. 21–9, Jan. 2007.

[5]     "The Mobile Internet Report," New York, 2009.

[6]     S. M. Sze, *Semiconductor Devices*. New York: John Wiley & Sons, Inc., 2002.

[7]     W. A. Triebel and A. E. Chu, *Handbook of Semiconductor and Bubble Memories*. Englewood Cliffs, NJ: Prentice-Hall, Inc., 1982.

[8]     C. Chappert, A. Fert, and F. N. Van Dau, "The emergence of spin electronics in data storage.," *Nat. Mater.*, vol. 6, no. 11, pp. 813–23, Nov. 2007.

[9]     D. S. Jeong, R. Thomas, R. S. Katiyar, J. F. Scott, H. Kohlstedt, A. Petraru, and C. S. Hwang, "Emerging memories: resistive switching mechanisms and current status.," *Rep. Prog. Phys.*, vol. 75, no. 7, p. 076502, Jul. 2012.

[10]    A. Makarov, V. Sverdlov, and S. Selberherr, "Emerging memory technologies: Trends, challenges, and modeling methods," *Microelectron. Reliab.*, vol. 52, no. 4, pp. 628–634, Apr. 2012.

[11]    C.-U. Pinnow and T. Mikolajick, "Material Aspects in Emerging Nonvolatile Memories," *J. Electrochem. Soc.*, vol. 151, no. 6, p. K13, Jun. 2004.

[12]    J. M. Slaughter, R. W. Dave, M. DeHerrera, M. Durlam, B. N. Engel, J. Janesky, N. D. Rizzo, and S. Tehrani, "Fundamentals of MRAM Technology," *J. Supercond.*, vol. 15, no. 1, pp. 19–25, Feb. 2002.

[13]    N. P. Vasil'eva and S. I. Kasatkin, "Magnetic Random Access Memory Devices," *Autom. Remote Control*, vol. 64, no. 9, pp. 1369–1385, Sep. 2003.

[14]  S. A. Wolf, D. D. Awschalom, R. A. Buhrman, J. M. Daughton, S. von Molnár, M. L. Roukes, A. Y. Chtchelkanova, and D. M. Treger, "Spintronics: a spin-based electronics vision for the future.," *Science*, vol. 294, no. 5546, pp. 1488–95, Nov. 2001.

[15]  T. Kawahara, K. Ito, R. Takemura, and H. Ohno, "Spin-transfer torque RAM technology: Review and prospect," *Microelectron. Reliab.*, vol. 52, no. 4, pp. 613–627, Apr. 2012.

[16]  S. Parkin, C. Kaiser, A. Panchula, K. Roche, and M. Samant, "Magnetically engineered spintronic sensors and memory," *Proc. IEEE*, vol. 91, no. 5, pp. 661–680, May 2003.

[17]  H. Zabel, "Progress in spintronics," *Superlattices Microstruct.*, vol. 46, no. 4, pp. 541–553, Oct. 2009.

[18]  A. K. Sharma, *Advanced Semiconductor Memories*. Piscataway, NJ: John Wiley & Sons, Inc., 2003.

[19]  M. T. Bohr, "Nanotechnology goals and challenges for electronic applications," *IEEE Trans. Nanotechnol.*, vol. 1, no. 1, pp. 56–62, Mar. 2002.

[20]  Y. Nakagome, M. Horiguchi, T. Kawahara, and K. Itoh, "Review and future prospects of low-voltage RAM circuits," *IBM J. Res. Dev.*, vol. 47, no. 5.6, pp. 525–552, Sep. 2003.

[21]  F. Nasirpouri and A. Nogaret, *Nanomagnetism and Spintronics: Fabrication, Materials, Characterization, and Applications*. Hackensack, NJ: World Scientific Publishing Co. Pte. Ltd., 2011.

[22]  O. Fruchart and A. Thiaville, "Magnetism in reduced dimensions," *Comptes Rendus Phys.*, vol. 6, no. 9, pp. 921–933, Nov. 2005.

[23]  R. Skomski, "Nanomagnetics," *J. Phys. Condens. Matter*, vol. 15, no. 20, pp. R841–R896, May 2003.

[24]  H. J. de Wit, "Soft magnetic multilayers," *Reports Prog. Phys.*, vol. 55, no. 2, pp. 113–155, Feb. 1992.

[25]  M. Kruzík and A. Prohl, "Recent Developments in the Modeling, Analysis, and Numerics of Ferromagnetism," Aug. 2006.

[26]  C. S. Edmund, "Ferromagnetism: magnetization curves," *Reports Prog. Phys.*, vol. 13, no. 1, pp. 83–183, Jan. 1950.

[27]  B. D. Cullity and C. D. Graham, *Introduction to Magnetic Materials*. Hoboken, NJ: John Wiley & Sons, Inc., 2009.

[28]  A. H. Bobeck, P. I. Bonyhard, and J. E. Geusic, "Magnetic bubbles&#8212;An emerging new memory technology," *Proc. IEEE*, vol. 63, no. 8, pp. 1176–1195, 1975.

[29]  W. F. Beausoleil, D. T. Brown, and B. E. Phelps, "Magnetic Bubble Memory Organization," *IBM J. Res. Dev.*, vol. 16, no. 6, pp. 587–591, Nov. 1972.

[30]  R. E. Fontana and S. R. Hetzler, "Magnetic memories: Memory hierarchy and processing perspectives (invited)," *J. Appl. Phys.*, vol. 99, no. 8, p. 08N902, Apr. 2006.

[31]  Rick Merritt and R. Merritt, *Hard drives go perpendicular*. [[EE Times]], 2005.

[32]  S. N. Piramanayagam, "Perpendicular recording media for hard disk drives," *J. Appl. Phys.*, vol. 102, no. 1, p. 011301, Jul. 2007.

[33]  H. J. Richter, "The transition from longitudinal to perpendicular recording," *J. Phys. D. Appl. Phys.*, vol. 40, no. 9, pp. R149–R177, May 2007.

[34]  A. Hubert and R. Schafer, *Magnetic Domains*. New York, NY: Springer-Verlag Berlin Heidelberg, 2000.

[35]  M. H. Kryder, E. C. Gage, T. W. McDaniel, W. A. Challener, R. E. Rottmayer, and M. F. Erden, "Heat Assisted Magnetic Recording," *Proc. IEEE*, vol. 96, no. 11, pp. 1810–1835, Nov. 2008.

[36]  A. Chung, J. Deen, J.-S. Lee, and M. Meyyappan, "Nanoscale memory devices.," *Nanotechnology*, vol. 21, no. 41, p. 412001, Oct. 2010.

[37]  C. Augustine, N. N. Mojumder, X. Fong, S. H. Choday, S. P. Park, and K. Roy, "Spin-Transfer Torque MRAMs for Low Power Memories: Perspective and Prospective," *IEEE Sens. J.*, vol. 12, no. 4, pp. 756–766, Apr. 2012.

[38]  T. M. Maffitt, J. K. DeBrosse, J. A. Gabric, E. T. Gow, M. C. Lamorey, J. S. Parenteau, D. R. Willmott, M. A. Wood, and W. J. Gallagher, "Design considerations for MRAM," *IBM J. Res. Dev.*, vol. 50, no. 1, pp. 25–39, Jan. 2006.

[39]  D. Pinna, A. Mitra, D. L. Stein, and A. D. Kent, "Thermally assisted spin-transfer torque magnetization reversal in uniaxial nanomagnets," *Appl. Phys. Lett.*, vol. 101, no. 26, p. 262401, May 2012.

[40]   I. L. Prejbeanu, S. Bandiera, J. Alvarez-Hérault, R. C. Sousa, B. Dieny, and J.-P. Nozières, "Thermally assisted MRAMs: ultimate scalability and logic functionalities," *J. Phys. D. Appl. Phys.*, vol. 46, no. 7, p. 074002, Feb. 2013.

[41]   I. L. Prejbeanu, M. Kerekes, R. C. Sousa, H. Sibuet, O. Redon, B. Dieny, and J. P. Nozières, "Thermally assisted MRAM," *J. Phys. Condens. Matter*, vol. 19, no. 16, p. 165218, Apr. 2007.

[42]   L. W. Martin, S. P. Crane, Y.-H. Chu, M. B. Holcomb, M. Gajek, M. Huijben, C.-H. Yang, N. Balke, and R. Ramesh, "Multiferroics and magnetoelectrics: thin films and nanostructures," *J. Phys. Condens. Matter*, vol. 20, no. 43, p. 434220, Oct. 2008.

[43]   G. Srinivasan, "Magnetoelectric Composites," *Annu. Rev. Mater. Res.*, vol. 40, no. 1, pp. 153–178, Jun. 2010.

[44]   C.-W. Nan, M. I. Bichurin, S. Dong, D. Viehland, and G. Srinivasan, "Multiferroic magnetoelectric composites: Historical perspective, status, and future directions," *J. Appl. Phys.*, vol. 103, no. 3, p. 031101, Feb. 2008.

[45]   G. Lawes and G. Srinivasan, "Introduction to magnetoelectric coupling and multiferroic films," *J. Phys. D. Appl. Phys.*, vol. 44, no. 24, p. 243001, Jun. 2011.

[46]   D. I. Khomskii, "Multiferroics: Different ways to combine magnetism and ferroelectricity," *J. Magn. Magn. Mater.*, vol. 306, no. 1, pp. 1–8, Nov. 2006.

[47]   W. Eerenstein, N. D. Mathur, and J. F. Scott, "Multiferroic and magnetoelectric materials.," *Nature*, vol. 442, no. 7104, pp. 759–65, Aug. 2006.

[48]   J. P. Velev, S. S. Jaswal, and E. Y. Tsymbal, "Multi-ferroic and magnetoelectric materials and interfaces.," *Philos. Trans. A. Math. Phys. Eng. Sci.*, vol. 369, no. 1948, pp. 3069–97, Aug. 2011.

[49]   Y.-H. Chu, L. W. Martin, M. B. Holcomb, M. Gajek, S.-J. Han, Q. He, N. Balke, C.-H. Yang, D. Lee, W. Hu, Q. Zhan, P.-L. Yang, A. Fraile-Rodríguez, A. Scholl, S. X. Wang, and R. Ramesh, "Electric-field control of local ferromagnetism using a magnetoelectric multiferroic.," *Nat. Mater.*, vol. 7, no. 6, pp. 478–82, Jun. 2008.

[50]   J. Cui, J. L. Hockel, P. K. Nordeen, D. M. Pisani, C. Liang, G. P. Carman, and C. S. Lynch, "A method to control magnetism in individual strain-mediated magnetoelectric islands," *Appl. Phys. Lett.*, vol. 103, no. 23, p. 232905, Dec. 2013.

[51]   C. A. F. Vaz, "Electric field control of magnetism in multiferroic heterostructures.," *J. Phys. Condens. Matter*, vol. 24, no. 33, p. 333201, Aug. 2012.

[52] "Multiferroicity: the coupling between magnetic and polarization orders - 000018730902920554." [Online]. Available: http://www.tandfonline.com/doi/pdf/10.1080/000018730902920554. [Accessed: 18-Jul-2013].

[53] N. A. Hill, "Why Are There so Few Magnetic Ferroelectrics?," *J. Phys. Chem. B*, vol. 104, no. 29, pp. 6694–6709, Jul. 2000.

[54] J. Ma, J. Hu, Z. Li, and C.-W. Nan, "Recent progress in multiferroic magnetoelectric composites: from bulk to thin films.," *Adv. Mater.*, vol. 23, no. 9, pp. 1062–87, Mar. 2011.

[55] H. J. A. Molegraaf, J. Hoffman, C. A. F. Vaz, S. Gariglio, D. van der Marel, C. H. Ahn, and J.-M. Triscone, "Magnetoelectric Effects in Complex Oxides with Competing Ground States," *Adv. Mater.*, vol. 21, no. 34, pp. 3470–3474, Sep. 2009.

[56] S. M. Wu, S. A. Cybart, P. Yu, M. D. Rossell, J. X. Zhang, R. Ramesh, and R. C. Dynes, "Reversible electric control of exchange bias in a multiferroic field-effect device.," *Nat. Mater.*, vol. 9, no. 9, pp. 756–61, Sep. 2010.

[57] C. Thiele, K. Dörr, O. Bilani, J. Rödel, and L. Schultz, "Influence of strain on the magnetization and magnetoelectric effect in La0.7A0.3MnO3∕PMN-PT(001) (A=Sr,Ca)," *Phys. Rev. B*, vol. 75, no. 5, p. 054408, Feb. 2007.

[58] J. J. Yang, Y. G. Zhao, H. F. Tian, L. B. Luo, H. Y. Zhang, Y. J. He, and H. S. Luo, "Electric field manipulation of magnetization at room temperature in multiferroic CoFe[sub 2]O[sub 4]/Pb(Mg[sub 1/3]Nb[sub 2/3])[sub 0.7]Ti[sub 0.3]O[sub 3] heterostructures," *Appl. Phys. Lett.*, vol. 94, no. 21, p. 212504, May 2009.

[59] T. Brintlinger, S.-H. Lim, K. H. Baloch, P. Alexander, Y. Qi, J. Barry, J. Melngailis, L. Salamanca-Riba, I. Takeuchi, and J. Cumings, "In situ observation of reversible nanomagnetic switching induced by electric fields.," *Nano Lett.*, vol. 10, no. 4, pp. 1219–23, Apr. 2010.

[60] A. G. Olabi and A. Grunwald, "Design and application of magnetostrictive materials," *Mater. Des.*, vol. 29, no. 2, pp. 469–483, Jan. 2008.

[61] J. Atulasimha and A. B. Flatau, "A review of magnetostrictive iron–gallium alloys," *Smart Mater. Struct.*, vol. 20, no. 4, p. 043001, Apr. 2011.

[62] A. E. Clark, J. B. Restorff, M. Wun-Fogle, T. A. Lograsso, and D. L. Schlagel, "Magnetostrictive properties of body-centered cubic Fe-Ga and Fe-Ga-Al alloys," *IEEE Trans. Magn.*, vol. 36, no. 5, pp. 3238–3240, 2000.

[63]  M. Wuttig, L. Dai, and J. Cullen, "Elasticity and magnetoelasticity of Fe–Ga solid solutions," *Appl. Phys. Lett.*, vol. 80, no. 7, p. 1135, Feb. 2002.

[64]  R. Wu, "Origin of large magnetostriction in FeGa alloys," *J. Appl. Phys.*, vol. 91, no. 10, p. 7358, May 2002.

[65]  E. M. Summers, T. A. Lograsso, and M. Wun-Fogle, "Magnetostriction of binary and ternary Fe–Ga alloys," *J. Mater. Sci.*, vol. 42, no. 23, pp. 9582–9594, Aug. 2007.

[66]  J. R. Hattrick-Simpers, D. Hunter, C. M. Craciunescu, K. S. Jang, M. Murakami, J. Cullen, M. Wuttig, I. Takeuchi, S. E. Lofland, L. Benderksy, N. Woo, R. B. Van Dover, T. Takahashi, and Y. Furuya, "Combinatorial investigation of magnetostriction in Fe–Ga and Fe–Ga–Al," *Appl. Phys. Lett.*, vol. 93, no. 10, p. 102507, Sep. 2008.

[67]  J. Furthmüller, M. Fähnle, and G. Herzer, "Theory of magnetostriction in amorphous and polycrystalline ferromagnets," *J. Magn. Magn. Mater.*, vol. 69, no. 1, pp. 79–88, Oct. 1987.

[68]  N. C. Koon, C. M. Williams, and B. N. Das, "Giant magnetostriction materials," *J. Magn. Magn. Mater.*, vol. 100, no. 1–3, pp. 173–185, Nov. 1991.

[69]  S. Rafique, "Magnetic anisotropy of FeGa alloys," *J. Appl. Phys.*, vol. 95, no. 11, p. 6939, May 2004.

[70]  H. Uchida, Y. Matsumura, H. Uchida, and H. Kaneko, "Progress in thin films of giant magnetostrictive alloys," *J. Magn. Magn. Mater.*, vol. 239, no. 1–3, pp. 540–545, Feb. 2002.

[71]  J. Atulasimha, A. B. Flatau, and E. Summers, "Characterization and energy-based model of the magnetomechanical behavior of polycrystalline iron–gallium alloys," *Smart Mater. Struct.*, vol. 16, no. 4, pp. 1265–1276, Aug. 2007.

[72]  D. Hunter, W. Osborn, K. Wang, N. Kazantseva, J. Hattrick-Simpers, R. Suchoski, R. Takahashi, M. L. Young, A. Mehta, L. A. Bendersky, S. E. Lofland, M. Wuttig, and I. Takeuchi, "Giant magnetostriction in annealed Co(1-x)Fe(x) thin-films.," *Nat. Commun.*, vol. 2, p. 518, Jan. 2011.

[73]  N. C. Woo, B. G. Ng, and R. B. van Dover, "High-Throughput Measurement of Magnetostriction Using MEMS and Composition Spreads," *MRS Proc.*, vol. 894, pp. 0894–LL07–03, Feb. 2011.

[74]  D. B. Williams and C. B. Carter, *Transmission Electron Microscopy*. New York, NY: Springer, 1996.

[75]  H. W. Fuller and M. E. Hale, "Determination of Magnetization Distribution in Thin Films Using Electron Microscopy," *J. Appl. Phys.*, vol. 31, no. 2, p. 238, Jun. 1960.

[76]  H. Hoffmann, "Quantitative Calculation of the Magnetic Ripple of Uniaxial Thin Permalloy Films," *J. Appl. Phys.*, vol. 35, no. 6, p. 1790, Jul. 1964.

[77]  H. Hoffmann, "Theory of magnetization ripple," *IEEE Trans. Magn.*, vol. 4, no. 1, pp. 32–38, Mar. 1968.

[78]  M. E. Hale, H. W. Fuller, and H. Rubinstein, "Magnetic Domain Observations by Electron Microscopy," *J. Appl. Phys.*, vol. 30, no. 5, p. 789, Jun. 1959.

[79]  H. W. Fuller and M. E. Hale, "Static and Dynamic Studies of Magnetization Distribution in Thin Films by Electron Microscopy," *J. Appl. Phys.*, vol. 31, no. 5, p. S308, Aug. 1960.

[80]  J. N. Chapman, A. B. Johnston, and L. J. Heyderman, "Coherent Foucault imaging: A method for imaging magnetic domain structures in thin films," *J. Appl. Phys.*, vol. 76, no. 9, p. 5349, Nov. 1994.

[81]  "SPI Supplies." [Online]. Available: http://www.2spi.com/catalog/grids/silicon-nitride.php.

[82]  M. Ali, C. Marrows, B. Hickey, F. Offi, J. Wang, L. Chelaru, M. Kotsugi, and W. Kuch, "Suppression of magnetization ripple by exchange bias," *Phys. Rev. B*, vol. 79, no. 6, p. 064415, Feb. 2009.

[83]  D.-T. Ngo, A. Hashimoto, S. McVitie, S. Saito, J. N. Chapman, and M. Takahashi, "Nanoscale physical microstructure and micromagnetic behaviour of CoIr film with negative anisotropy," *J. Phys. D. Appl. Phys.*, vol. 44, no. 9, p. 095001, Mar. 2011.

[84]  A. Hubert and R. Schafer, *Magnetic Domains: The Analysis of Magnetic Microstructures*. New York, NY: Springer, 2000.

[85]  U. Komaragiri, M. R. Begley, and J. G. Simmonds, "The Mechanical Response of Freestanding Circular Elastic Films Under Point and Pressure Loads," *J. Appl. Mech.*, vol. 72, no. 2, p. 203, Mar. 2005.

[86]  S. Timoshenko and S. Woinowsky-Krieger, *Theory of Plates and Shells*. New York, NY: MrGraw-Hill, 1959, pp. 203–205.

[87]  A. Libai and J. G. Simmonds, *The Nonlinear Theory of Elastic Shells*. Cambridge, United Kingdom: Cambridge University Press, 1998.

[88]  M. Donahue and D. Porter, "OOMMF User's Guide Version 1.0," *Res. J. Natl. Inst. Stand. Technol.*, 1999.

[89]  T. Y. Tsui, J. J. Vlassak, and A. J. McKerrow, "Measuring the elastic modulus and ultimate strength of low-k dielectric materials by means of the bulge test," in *Proceedings of the IEEE 2004 International Interconnect Technology Conference (IEEE Cat. No.04TH8729)*, pp. 133–135.

[90]  T. Y. Tsui, J. J. Vlassak, and A. J. McKerrow, "Measuring the elastic modulus and ultimate strength of low-k dielectric materials by means of the bulge test," in *Proceedings of the IEEE 2004 International Interconnect Technology Conference (IEEE Cat. No.04TH8729)*, 2004, pp. 133–135.

[91]  P. Temple-Boyer, "Residual stress in low pressure chemical vapor deposition SiN[sub x] films deposited from silane and ammonia," *J. Vac. Sci. Technol. A Vacuum, Surfaces, Film.*, vol. 16, no. 4, p. 2003, Jul. 1998.

[92]  T. Ueno and T. Higuchi, "Investigation of Micro Bending Actuator using Iron-Gallium Alloy (Galfenol)," in *2007 International Symposium on Micro-NanoMechatronics and Human Science*, 2007, pp. 460–465.

[93]  E. Lage, C. Kirchhof, V. Hrkac, L. Kienle, R. Jahns, R. Knöchel, E. Quandt, and D. Meyners, "Exchange biasing of magnetoelectric composites.," *Nat. Mater.*, vol. 11, no. 6, pp. 523–9, Jun. 2012.

[94]  J. Nogués, J. Sort, V. Langlais, V. Skumryev, S. Suriñach, J. S. Muñoz, and M. D. Baró, "Exchange bias in nanostructures," *Phys. Rep.*, vol. 422, no. 3, pp. 65–117, Dec. 2005.

[95]  X. Zhang, Q. Zhan, G. Dai, Y. Liu, Z. Zuo, H. Yang, B. Chen, and R.-W. Li, "Effect of mechanical strain on magnetic properties of flexible exchange biased FeGa/IrMn heterostructures," *Appl. Phys. Lett.*, vol. 102, no. 2, p. 022412, Jan. 2013.

[96]  A. Gentils, J. N. Chapman, G. Xiong, and R. P. Cowburn, "Variation of domain-wall structures and magnetization ripple spectra in permalloy films with controlled uniaxial anisotropy," *J. Appl. Phys.*, vol. 98, no. 5, p. 053905, Sep. 2005.

[97]  V. Novosad, Y. Otani, A. Ohsawa, S. G. Kim, K. Fukamichi, J. Koike, K. Maruyama, O. Kitakami, and Y. Shimada, "Novel magnetostrictive memory device," *J. Appl. Phys.*, vol. 87, no. 9, p. 6400, May 2000.

[98]  H. Lu, C.-W. Bark, D. Esque de los Ojos, J. Alcala, C. B. Eom, G. Catalan, and A. Gruverman, "Mechanical writing of ferroelectric polarization.," *Science*, vol. 336, no. 6077, pp. 59–61, Apr. 2012.